Doctoral Dissertation (Shinshu University)

Study on moisture-induced electricity generation of graphene oxide-based film

(酸化グラフェン系フィルムの水分誘起発電に関する研究)

Graduate School of Medicine, Science and Technology

CHEN SI

19HS152A

September 2022

Contents

Abstract

Green energy conversion is the first choice in solving contemporary energy pollution and shortages. Harvesting energy from clean and inexhaustible widespread small-scale water in nature environment, is promising choice to alleviate the energy crisis. Graphene oxide (GO) is rich in oxygen-related functional groups such as hydroxyl and carboxyl groups and has good application prospects. Interested in potential applications in electronics, energy-related devices, and smart systems that are highly dependent on flexible regulation of oxygen content. Ultraviolet (UV) irradiation treatment, as a clean and effective method can remove oxygen-containing groups (OCGs) of GO. OCGs in GO is beneficial to hydrophilic, so GO-based films with regionally hydrophilic difference can be obtained by UV treatment.

Firstly, GO film (GOF) was reduced by UV irradiation for different times, and based on the reduction degree and surface hydrophilicity, 3 h was considered as a good option. The RGO/GO film (RGF) has considerable hydrophilicity and conductivity differences in its two surfaces, which endow it the application potential in moisture-induced power generation. RGF could generated electricity in humid environment. The RGF-based generator showed good output performance in high humidity

which can generated electricity of 424 mV, 9.2 uA, and the generator with expandation could power a timer. Therefore, the UV reduced GO-based film with the hydrophilic difference is very promising in moisture induced electricity, and further use can be done to employ UV treated GO-based films for more applications.

However, the RGF-based generator has a short power supply time. Hence, developing a sustainably powered electricity generator based on UV-treated GO-based film should be conducted. Afterwards, a sustainably moisture-induced electricity generator which can supply considerable electrical power even when transferred to a dry condition was developed. GO film was simply region-treated by bilateral ultraviolet irradiation to obtain two special structural films—RGO/GO/RGO sandwich-like structural film (RGRSF) and RGRSF–GO composite films. The special sandwich-like structure endows films with the capability to easily transport water molecules and difficultly release moisture that improve the adaptability of generator to environmental change. A single moisture induce electricity generation (MIEG) could supply an open circuit voltage of 215.7 mV for more than 3 h. 9MIEGs successfully powered a LED in 1 h under moisture, and its total discharging process took about 5.5 h in a normal room condition, in which the LED kept lit for 1 h. Additionally, with outstanding flexibility, high stability, and reproducibility, the generator shows the potential in application of wearable electronics, and it

can generate sustainable electricity in the face of suddenly changes in humidity.

Moisture from the breath is one of ubiquitous water energy sources. The inability to continuously provide water molecules limits its application in moisture-induced electricity generation. Developing a sustainable breath moisture-induced power generator is a challenge. MIEG presented above can only generate about 50 mV under 45%, and the charging time is too long which nearly took 50 mins. So, the sensitivity to low moisture of the generator should be improved to conduct high performance and fast response. Therefore, based on the sandwich structure that can help to slow down the discharging behavior, we first develop an electricity-sustainable breath-moisture-induced electricity generator (BMIEG) during intermittent exhalations. The generator is fabricated by the end-to-end connection of two equal asymmetric regional sandwich structural graphene oxide/carbon nanotube based composite films, making it continuously expandable without limit. The appropriate addition of CNT facilitates the establishment of a continuous CNT network channel and induces voltage when water flows through the surface of the CNTs to enhance the output performance. The BMIEG presents a slow discharging behavior when exhalation is stopped, and it continually lights up a light-emitting diode in the intermittent exhalation process with a simple size expansion of a series of array arrangements. Additionally, the BMIEG is freely assembled using

a capacitor to achieve variable voltage and/or stabilized voltage electricity supply. The flexibility and reusability of the generator show its considerable application prospects in wearable electronic products.

In conclusion, UV treatment can be used to obtain various the GO-based films with reginal difference in hydrophilicity which is promising in the field of moisture-induce electricity generation. Based on the regionally hydrophilic difference of GO-based films, environmental and breath moisture-induced power generators which could continuable power were developed. Besides, UV treated GO-based films show many advantages such as well controllable, flexible, and wearable. In the further research, sunlight can be considered to replace UV irradiation as a source to obtain similar good effect and other different regional treatments can be discussion for more applications.

Chapter 1：Introduction

In 2004, a new type of nano-carbonaceous material, graphene, was reported by researchers. Like fullerenes and carbon nanotubes, due to its excellent electrical properties and high specific surface area, graphene shows application potential in the field of gas and humidity sensors. At the same time, due to its two-dimensional structural properties, graphene is suitable for the existing processing technology of planar electronic devices. Therefore, a lot of research work on graphene chemical gas sensors has appeared in recent years. Meanwhile, a series of derivatives of graphene, such as graphene oxide (GO) and reduced graphene oxide (rGO), have also been widely reported for chemical gas sensors. Below we briefly introduce the preparation methods of graphene materials and GO.

1.1 The structure and properties of graphene

Graphene is a two-dimensional crystal composed of carbon six-membered rings in a periodic honeycomb lattice structure[1]. It can be seen as the basic unit that constitutes the allotropes of other carbons, as shown in Figure 1-1. Graphene can be deformed into zero-dimensional fullerenes, rolled to form one-dimensional carbon nanotubes, and stacked to form three-dimensional graphite. The ideal graphene structure is a planar

hexagonal lattice with a C—C bond length of about 0.142 nm [1], which can be regarded as a layer of exfoliated graphite atoms, with a theoretical thickness of 0.335 nm[1]. Each carbon atom in the atomic layer of graphite is in sp2 hybrid state and contributes an electron on the remaining p orbital to form a π bond. The π electron can move freely and unhindered in the plane structure, so graphene has excellent electrical conductivity. Its electron mobility reaches 15000 cm^2/vs, which is significantly better than that of the traditional transistor material (1400 cm^2/vs) and is less affected by temperature and doping effect[2]s. In addition to the excellent electrical properties of graphene, its non-electrical properties have also attracted the attention of scientists. The mechanical modulus and ultimate strength of graphene reach 1100 GPa and 130 GPa, respectively[3], which are comparable to the mechanical properties of one-dimensional carbon nanotubes. Graphene also has a low density (~2 g/cm^3)[4], an excellent thermal conductivity of 3000 W/(M·K)[4] and a large specific surface area (2630 m^2/g)[5].
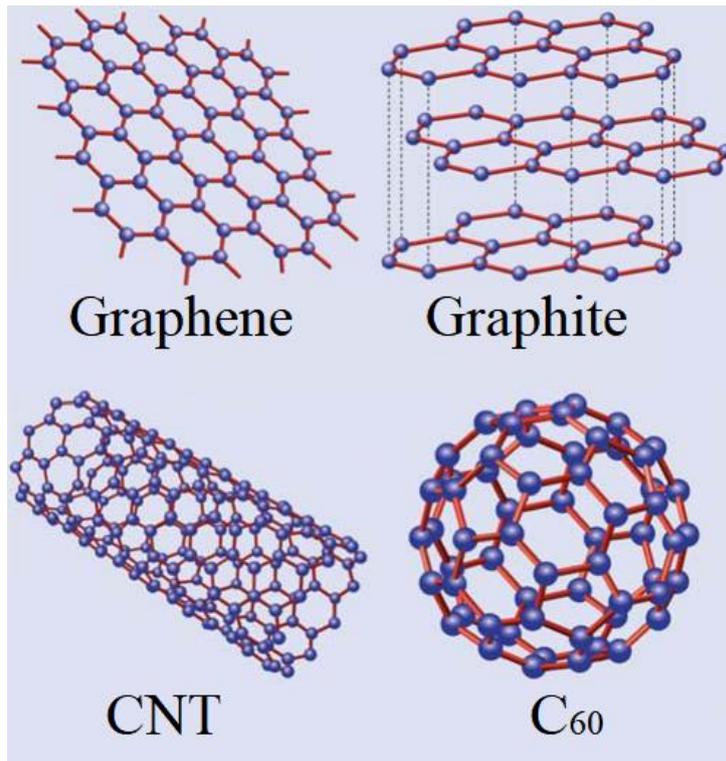
Figure 1-1 The structure of graphene, graphite, carbon nanotube (CNT) and Fullerenes

(C_{60})[6]

Due to the excellent mechanical and optical properties of graphene at the same time, combined with its special single-layer planar two-dimensional structure and its high specific surface area, graphene-based flexible electrical and sensor devices can be fabricated. Based on the above advantages, it is generally predicted that graphene materials have great application prospects in the fields of nanoelectronics, gas sensors, solar cells, capacitors, etc., and are expected to set off a new technological revolution in the century.

1.2 The preparation methods of graphene film

Whether graphene can be prepared on a large scale directly determines its application prospects, so the preparation method of graphene is currently a research hotspot in the industry. At present, the graphene preparation methods reported in the literature mainly include the following.

1.2.1 Micromechanical peeling method

In 2004, Heim's research group pretreated pyrolytic graphite with a high degree of orientation, and then used tape to repeatedly paste the graphite on the silica substrate, and finally obtained a stable single-layer graphene. Since the yield of this method is very low and difficult to control, it is not suitable for the application of large-scale and high-yield preparation of graphene and is currently mostly used in laboratory research fields. Figure 1-2 is the characterization diagram of the mechanically exfoliated graphene carried out by Heim's research group.
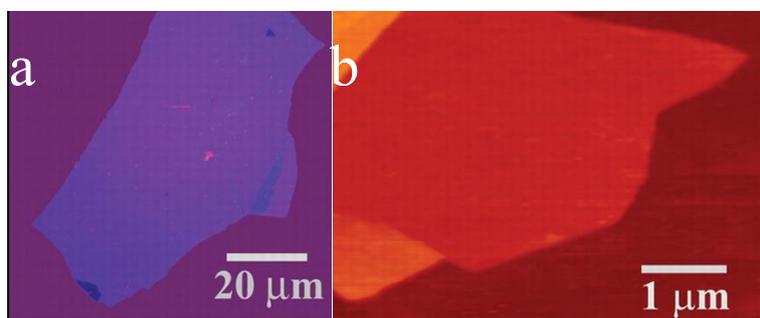
Figure 1-2 The optical micrograph of graphene prepared by mechanical exfoliation method (a) The substrate is silicon dioxide; (b) AFM image [7]

1.2.2 Chemical vapor deposition

In 2009, Ruoff's group reported a method for preparing graphite sintered sheets by chemical vapor deposition[8]. Using methane and oxygen as the basic raw materials, graphene sheets were obtained by chemical deposition on copper foil at high temperature (1000 °C), as shown in Figure 1-3. The test results show that the electron mobility of graphene prepared by CVD method reaches 4050 cm2/vs[8]. The graphene prepared by this method has good quality and can be prepared on a large scale, but the preparation of graphene by CVD has higher requirements on the required equipment and processes.
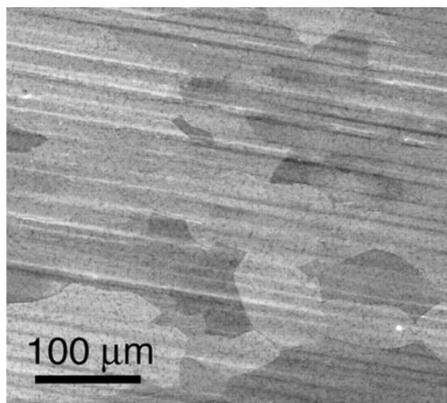
Figure 1-3 SEM image of graphene prepared on copper foil by CVD method[8]

1.2.3 Redox method

In 2007, Stankovich reported a method for chemically preparing graphene[9]. Graphite oxide is obtained by oxidizing intrinsic graphite, then exfoliating graphite oxide in solution to obtain a single layer GO structure, and finally reducing GO by adding a reducing agent to obtain the final graphene. In this method, since the reduction process usually cannot

make complete deoxidation, the obtained graphene usually still contains a small amount of oxygen functional groups, so the graphene obtained by this method is also called rGO. Figure 1-4 shows the SEM characterization of rGO prepared by Stankovich using the solution redox method. Different from the graphene prepared by the micromechanical exfoliation method and the chemical vapor deposition method, the morphology of the graphene prepared by the solution redox method is different. Flat, there will be a skirt wrinkle at the layer boundary. It is worth noting that the steps used in this method are all carried out in solution. Compared with methods such as micromechanical exfoliation and chemical vapor deposition, this method is simple and controllable, and has large scale and high yield (monolayer rate and high yield). The characteristics of low-cost preparation of graphene; at the same time, the entire system of this method is in the liquid phase, which can be very convenient to achieve thin film deposition. In summary, the solution redox method is currently the most mainstream method for preparing graphene. It is worth noting that, In the process of preparing graphene by solution redox method, GO, as an intermediate material for preparing graphene, can be regarded as functionalized graphene. In recent years, the electrical, mechanical, and thermal properties of GO have also attracted great interest of scientists, the research and application of various characteristics of GO have been emerging.
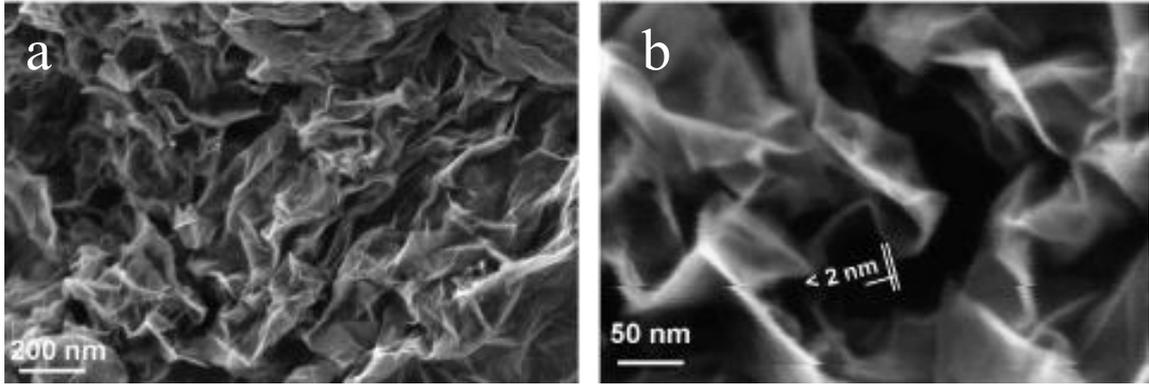
Figure 1-4 (a) SEM image of rGO; (b) local enlarged part [9]

1.3 The electrical and mechanical properties of GO

1.3.1 Electrochemical properties of GO

Due to the introduction of oxygen-containing functional groups, it has some new properties different from graphene. First, the introduction of oxygen-containing functional groups greatly changes the electrical properties of graphene compared with graphene, and part of the sp2 hybrid carbon atoms in the carbon six-membered ring is converted into sp3 hybrid carbon atoms, which directly abstracts the carbon six-membered ring. π electrons, which break the π bond originally formed in the C_8 ring, thus greatly weakening its ability to conduct electrons. In a dry atmosphere, the electrical conductivity of GO is extremely weak, showing a high resistance state (the sheet resistance value reaches $1012\Omega\cdot sq\text{-}1$) [10]. Venugopal experimentally studied the electrical transport properties of the films prepared by Hummer's method and found that the resistance of GO films is related to the ambient temperature, as shown in Figure 1-5, it can be

found that when the temperature is decreased from order of magnitude. Through the test and study of the field effect transistor (GO-FET) constructed by the film, the relationship between the channel current and the voltage between the gate and the source of the GO-FET is shown in the figure. It can be found that the film exhibits the characteristics of P-type semiconductor, its majority carriers are holes. Venugopal further pointed out that the exhibited p-type semiconductor characteristics originate from the introduction of many oxygen-containing functional groups.
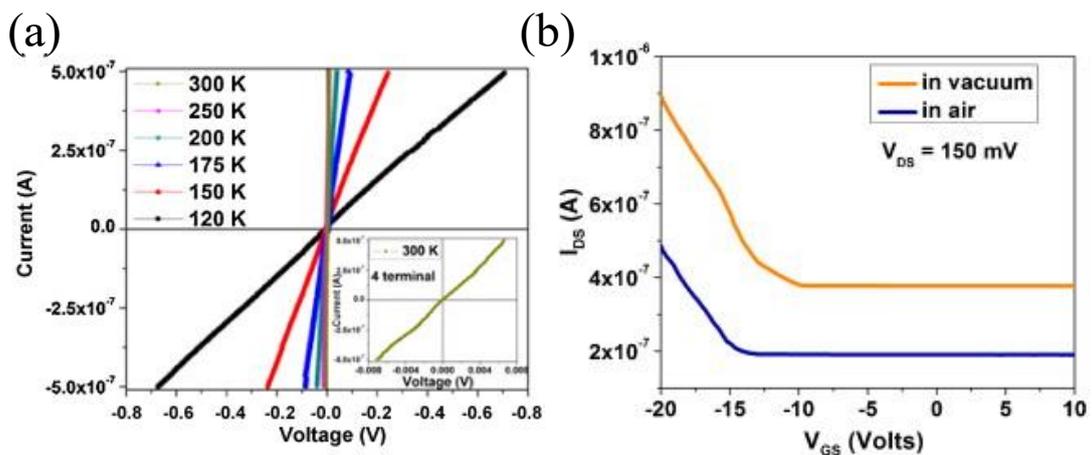
Figure 1-5 (a) I-V characteristics of GO films at different temperatures; (b) relationship between channel current and gate voltage of GO-FET [11]

The electrical conductivity of GO at room temperature is extremely weak, which greatly limits the application of GO materials in the field of electronic devices. In recent years, many research reports have shown that the electrical conductivity of GO can be restored by reductive deoxygenation, that is, GO to rGO. In addition, GO films have good

mechanical properties [12, 13]]. The mechanical modulus of GO films prepared by solution method is 6–42 GPa [13], and the extreme strength is 100–132 GPa[13], which is lower than that of mechanical exfoliation. The mechanical modulus of the obtained graphene is still higher than that of many traditional polymer materials (eg, rubber has a mechanical modulus of 7.8 GPa, polyethylene has a mechanical modulus of 0.2–0.8 GPa, and plexiglass PMMA has a mechanical modulus of 7.8 GPa. about 3 GPa), so it is very suitable for the preparation of flexible devices.

1.3.2 Dispersibility of GO

Unlike graphene, which is difficult to disperse in solvents, GO has good dispersibility. The most used medium for dispersing GO is water. Through mechanical stirring or ultrasound, GO can be easily dispersed in water to form a stable GO aqueous dispersion. The concentration of the obtained GO aqueous dispersion is usually 1-4 mg/ml[14-16]. At the same time, it can be seen from the GO structure model shown in the figure that GO is amphiphilic, specifically: the skeleton structure composed of a six-membered carbon ring is hydrophobic, while the oxygen-containing functional group connected to the six-membered carbon ring is hydrophobic. It is hydrophilic, so it has the characteristics of surfactants, and can be dispersed in water and most organic solvents, such as DMF, NMP, THF, EG, etc. [13] to form a stable GO dispersion, as shown in Figure 1-6. Pictures of GO solutions after ultrasonic dispersion in various

solvents and after standing for 3 weeks. At the same time, the stable GO dispersion can prepare uniform and continuous GO thin films by drop coating, spin coating, self-assembly and other film-forming methods, which provides convenient conditions for the application in the field of micro-nano electronic devices[12].
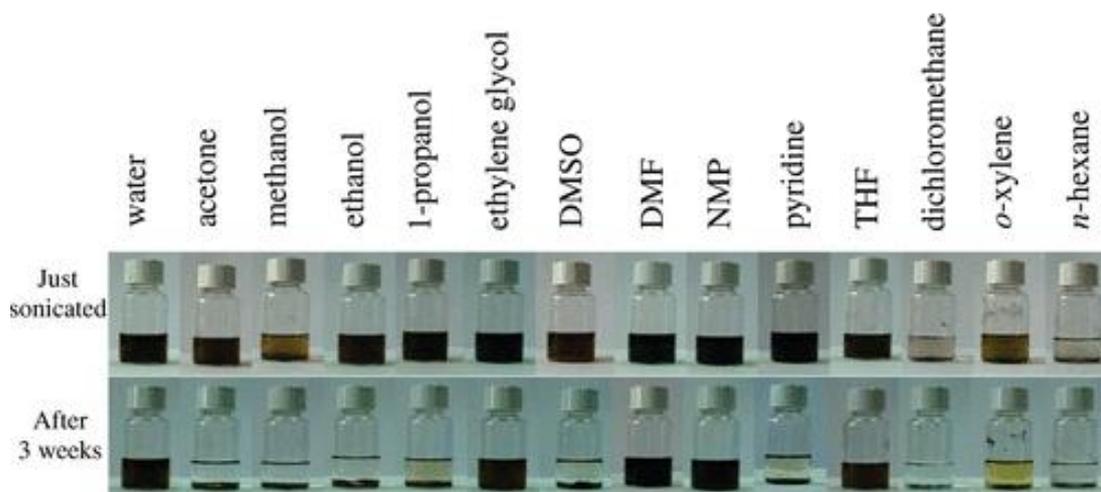
Figure 1-6 Dispersion photos of GO in water solvent and 13 medium organic solvents (a) after ultrasonication; (b) after 3 weeks of rest[17]

1.3.3 Hydrophilicity of GO

The introduction of oxygen-containing functional groups also makes GO have strong hydrophilic properties[13, 18]. GO can easily adsorb water molecules from the environment, and the water content inside GO completely depends on the external humidity level. Medhekar [13] discussed the interaction mechanism between water molecules and GO films in detail. For films formed by random stacking of GO, water molecules adsorbed into the interlayer voids of GO and formed an oxygen

bond network with the oxygen-containing functional groups of the GO layer. Figures 1-7a and 1-7b show the atomic structure models of G with water contents of 0.9% and 25.8%, respectively. Under the condition of relatively low external humidity, the GO film adsorbs less water molecules and its water content are low, and hydrogen bonds are mainly formed between the hydroxyl groups and hydroxyl groups, and between hydroxyl groups and epoxy groups between the GO layers. (Figure 1-8a); under the condition of relatively high external humidity, due to the large amount of water molecules adsorbed by GO, the water content of the GO film is correspondingly high, and many adsorbed water molecules enter the interlayer of the GO layer, and the surface of the GO layer interacts with the surface of the GO layer. Hydroxyl groups and epoxy groups form a hydrogen bond network through hydrogen bonding, as shown in Figure 1-8b. At this moment, due to the entry of water molecules into the interlayers of GO, the interlayer spacing of GO increases, causing the volume of the film to expand. At the same time, it is predicted by simulation that when the water content increases from the initial 0wt% to 26wt%, the spacing between the individual GO layers increases from 5.1 Å to 9.0 Å, and the volume expansion reaches 76%[13].
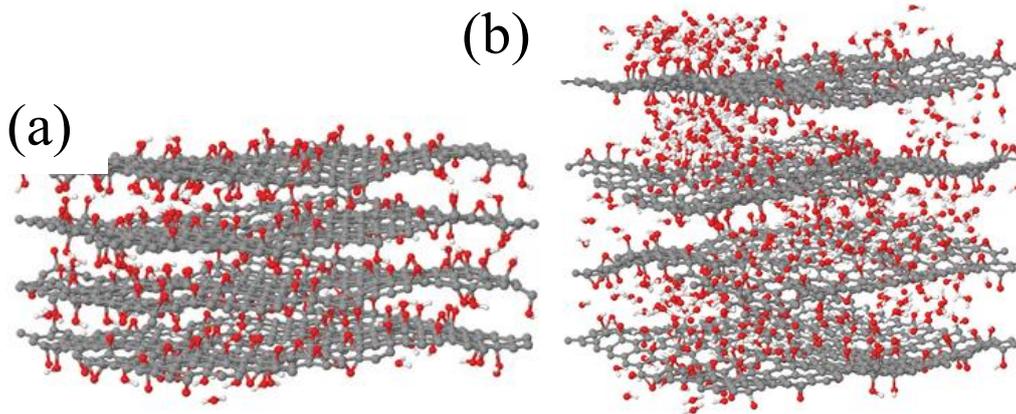
Figure 1-7 (a) Atomic structure of GO with water content of 0.9%; (b) Atomic structure of GO with water content of 25.8% [13]
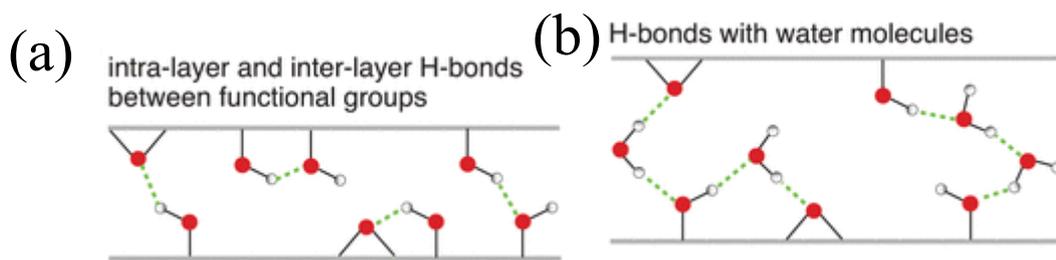
Figure 1-8 Schematic diagram of hydrogen bond formation of GO under different humidity conditions: (a) low humidity condition; (b) high humidity condition [13]

In 2013, Lee et al.[19] studied the water molecule adsorption mechanism of GO. Through first-principles calculations, they discussed the effect of a single GO hydrophilic functional group (such as hydroxyl) on one, two and three water molecules. adsorption, as shown in Figure 1-9. It can be found that the first adsorbed water molecule is combined with the hydrophilic functional group of GO through hydrogen bond adsorption, the second adsorbed water molecule is combined with the first adsorbed water

molecule through hydrogen bond adsorption, and the third adsorbed water molecule Then it combines with the second adsorbed water molecule through oxygen bond adsorption, thereby forming a stacked layer of multi-layer water molecules, and the entire adsorption process is physical adsorption. Lee further studied the change trend of the work function of GO under different ambient humidity conditions, and the results are shown in Figure 1-10. With the increase of humidity, the work function of GO decreases slightly, and its range is 4.3~4.4 eV[19]
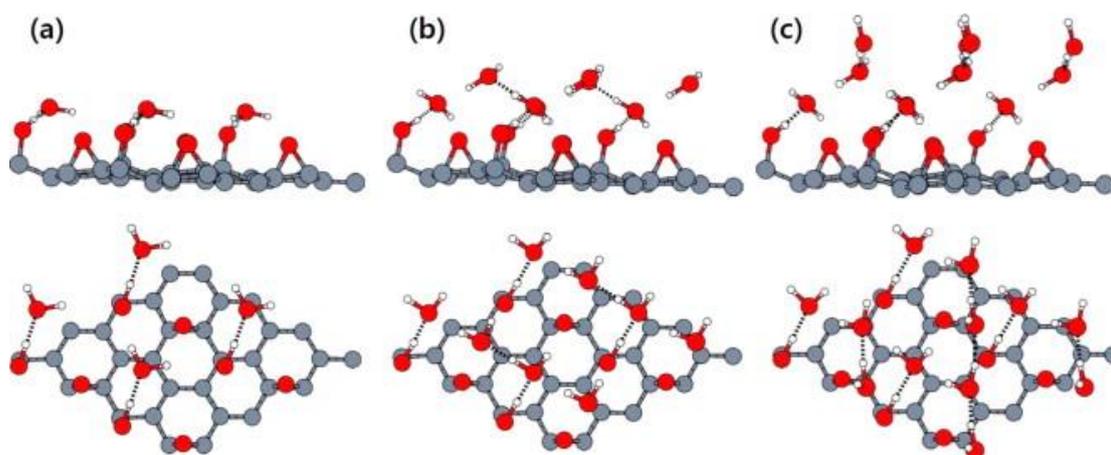
Figure 1-9 Water molecule adsorption model of a single hydrophilic functional group (such as hydroxyl) of GO: (a) one adsorbed water molecule; (b) two adsorbed water molecules; (c) three adsorbed water molecules [19]
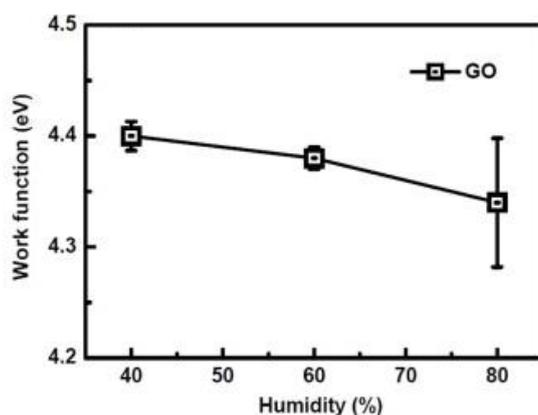
Figure 1-10 Variation curve of work function of GO under different humidity conditions [19]

In 2009, Park et al. [20] reported the bulk deformation behavior of the GO-CNT bilayer structure under humidity changes. The GO-CNT bilayer structure was obtained by suction filtration of the GO dispersion and the CNT dispersion in sequence, and the preparation process is shown in Figure 1-11. In this bilayer structure, the material is strongly hydrophilic, and the material is hydrophobic. The layer will undergo swelling and shrinking deformation during the rise and fall of humidity, while the GO layer hardly deforms during the humidity change. The volume deformation behavior of the bilayer structure under different ambient humidity conditions was investigated experimentally by Park, and the results are shown in Figure 1-12. Under low humidity conditions (RH = 12%), GO undergoes a curling behavior due to the desorption of water molecules, and this deformation causes the entire bilayer structure to curl. However, under high humidity conditions (RH>60%), swelling occurs due to the adsorption of water molecules, so that the entire bilayer structure bends in the opposite

18

direction to that under low humidity conditions. This experimental phenomenon shows that the adsorption and desorption of water molecules by GO can produce reversible mechanical deformation, which is expected to realize the MEMS humidity sensor based on GO material.
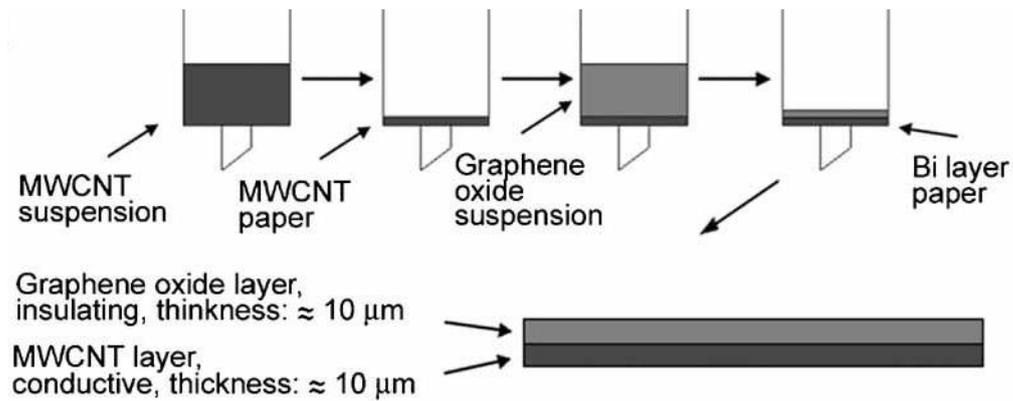
Figure 1-11 Graphene oxide carbon nanotube double-layer film prepared by suction filtration
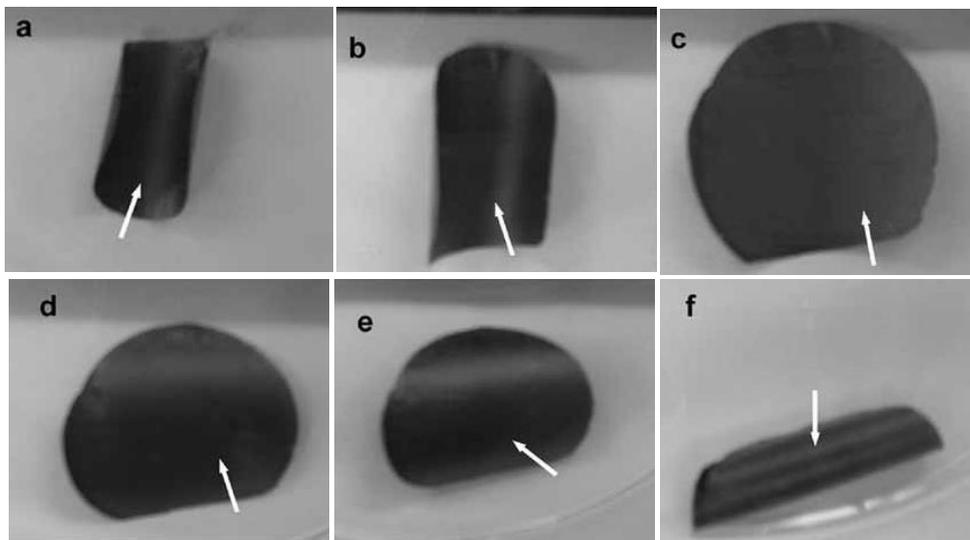
Figure 1-12 Deformation behavior of GO-CNT bilayer films under different humidity conditions[20]

1.4 The preparation methods of GO film

This chapter outlines the main preparation methods of GO membranes, and categorizes, analyzes, and summarizes the preparation methods of GO. The main preparation methods of GO membranes prepared from GO solutions include vacuum filtration, spin coating, Dip coating method, electrostatic self-assembly method, etc[21].

The preparation methods of graphite oxide mainly include physical methods and chemical methods. The physical method usually takes cheap flake graphite or expanded graphite as raw material, and directly prepares single-layer or multi-layer graphene by substrate-free gas phase synthesis method, thermal expansion exfoliation method, mechanical exfoliation method, liquid phase, or gas phase direct exfoliation method, etc.[22] After a series of oxidation, GO is obtained. The advantage of the physical method is that the raw materials are easy to obtain, the operation is relatively simple, and the synthetic graphene has high purity and fewer defects, but the shortcomings such as time-consuming and low yield make it unsuitable for large-scale production[23].

Chemical methods are generally prepared from natural flake graphite or natural graphite powder by oxidation and exfoliation. More oxidation methods are used, such as Brodie method, Staudenmaier method, Hummer's method, Brodie method and Staudenmaier method. The degree of oxidation is easy to control, but the reaction process Harmful gas will be

generated in the reaction time, and the reaction time is very long. The Staudenmaier method uses a mixed acid of concentrated sulfuric acid and fuming nitric acid to treat graphite, which seriously damages the layered structure of graphite. The Hummers method has a short reaction time, no toxic gas generation, and high safety, so it has become a commonly used method for preparing GO. At present, the most used method for preparing graphite oxide is the modified Hummers method. The specific process is as follows: assemble a beaker in an ice-water bath, add 23 parts of concentrated sulfuric acid, and add a solid mixture of 1 part of natural flake graphite and 0.5 part of sodium nitrate under stirring , and then slowly add 3 parts of potassium permanganate, add potassium permanganate, pay attention to control the reaction temperature not to exceed 20 °C, stir the reaction for a period of time, then heat up to about 35 °C, continue stirring for 1 h, many small bubbles will appear during this process[24]. Then slowly add a certain amount of deionized water, continue stirring for 40 min, and add an appropriate amount of hydrogen peroxide to reduce the residual oxidant, and the solution turns bright yellow. Filter while hot and wash with 3% HCl solution and deionized water until no sulfate is detected in the filtrate. Finally, the filter cake was fully dried in a vacuum drying oven at 60 °C.

According to many literature reports, to sum up, the preparation methods of GO films mainly include vacuum filtration method, spin coating method,

dip coating method, drop coating method, solvent casting method, electrostatic self-assembly method, and layer-by-layer self-assembly method[24]. Wait. Among them, the vacuum filtration method and the solvent casting method are the most used methods. They both use the pressure difference to obtain a uniform and relatively thick film, so they are discussed together; dip coating, spin coating, drop coating The methods are classified into one category for discussion, because they are all coated with several layers of GO nanosheets on the surface of the substrate to obtain relatively thin films; the electrostatic self-assembly method uses the hydrophilic edge and hydrophobic middle of the GO sheet. The interaction between the surfaces and the strong hydrogen bonds gathers the individual membranes in the GO film [25]; the layer-by-layer self-assembly method is to use the negative charge of GO to make it connect with the positively charged polymer or The GO film with controllable number of layers is prepared by the mutual attraction between the substrates, because the method is similar, and the electrostatic self-assembly method is discussed together.

1.4.1 Vacuum filtration method

The vacuum filtration method is to remove the solvent in the GO colloid through a pressure difference and obtain a GO film on the substrate. It is also possible to separate the film and the substrate by some methods to obtain an unsupported GO film. Commonly used substrates include Anodic

22

membranes, various organic polymer membranes and other membranes with larger pore sizes. These materials have little effect on the flux of the membrane while enhancing the strength of the GO membrane [26]. The pressure differential can be obtained by maintaining a vacuum environment on the permeate side, or by providing pressure on the dope side. The substrate can be either flat sheet membranes or hollow fiber membranes. To increase the flux of the membrane, suitable nanoparticles or organic substances can be added to the GO solution to obtain a mixed solution, and then the desired membrane can be obtained by filtration. The thickness of the membrane is controlled by adjusting the concentration of the colloidal suspension or the filtration volume. Compared with the spin coating method and the dip coating method, the membrane obtained by the vacuum filtration method is thicker, usually in the order of microns. In theory, only a certain pressure is needed to obtain uniform membranes of different thicknesses according to the set gel volume. The operation is very simple, but in the actual operation process, under a certain pressure, the GO layer spacing is small, and suction filtration becomes the time required for the membrane is longer. The principle of the solvent casting method [24] is the same as that of the vacuum filtration method, and the water in the GO solution is removed by pressure difference filtration, and the desired membrane is obtained after drying.

1.4.2 Dip coating method

The dip coating method is to immerse the substrate in the GO solution for a certain period of time, keep the substrate level as much as possible, take it out and attach it to a flat plate and dry it naturally or put it on a spin coater to spin dry to maintain the uniformity of the film, thereby making the graphite oxide The graphene sheets are integrated to obtain a thin GO film composed of several layers of GO nanosheets. Repeat the above steps to obtain a multi-layered GO film. The spin coating method is to attach the substrate to the flat plate on the spin coater. While the spin coater rotates at a certain number of revolutions, a certain concentration of GO solution is dropped at a certain rate above the center of the spin coater. The more graphene, the thicker the obtained GO film[27]. The major differences between the two methods are centrifugal force and immersion capillary force. The dip coating method is more complicated, and the centrifugal force and the immersion capillary force during the film formation will affect the GO sheet, resulting in less neatly arranged coating compared to the spin coating method. For spin coating, the movement of GO sheets caused by the immersion capillary force and the repulsion of the same charge between the edges is limited due to the rapid evaporation of the solution and the large centrifugal force, resulting in a uniform and highly interlocking stack structure. The membranes prepared by these two methods are relatively thin and uniform, and the number of coating layers

can be controlled by controlling the number of dip-coating times or the amount of dripped GO solution. The process control is more troublesome than the filtration method. The drop-coating method can prepare unsupported GO films. The main preparation process is as follows: drop a certain amount of GO colloidal suspension on a smooth substrate, dry at room temperature, and then remove from the substrate. An unsupported GO film was peeled off. The film prepared by this method has the advantages of large area, uniformity, and excellent mechanical strength, but it cannot obtain a thinner film and is not suitable for large-scale production [21].

1.4.3 Electrostatic self-assembly method

The electrostatic self-assembly method is to use the effect of the charge between GO to obtain a GO film with a controllable number of layers. The most used method is the layer-by-layer self-assembly method. The layer-by-layer self-assembly method makes the molecules and GO sheets alternately deposited on the substrate to form nanometer-thick films through electrostatic attraction or hydrogen bonding [28]. The specific operation method is to immerse the positively charged substrate in GO solution. For a certain period, drying, repeating several times; or alternately coating positively charged polymer and negatively charged GO solution on the substrate, and repeating several times after drying. The layer-by-layer self-assembly method is divided into two different bonding methods. The

first method is to use a suitable cross-linking agent to establish a covalent bond between the cross-linking agent and the GO layer through chemical reaction[29]. Another method is to use electrostatic adsorption to bond stacked GO sheets. The feasibility stems from the hydrolysis of carboxyl groups on GO sheets to make them negatively charged [30, 31], so that they can be adsorbed on positively charged substrates or by Positively charged polyelectrolytes such as polyacrylamide hydrochloride are attracted to obtain stable GO films. Compared with covalent bonding, the advantages of electrostatic adsorption bonding are the simple reaction of GO films, flexible control of chemical reactions, less use of organic solvents, and reduction of by-products during the manufacturing process. For GO film to be practically applied to water and solute separation, the integrity of the membrane must be ensured. GO membrane is easy to disperse in aqueous solution because of its good hydrophilicity and is especially not suitable for membrane operation. Commonly used crossflow filtration [32]. Both covalent cross-linking and electrostatic adsorption can lead to tight bonding between adjacent GO layers and between the outermost layer and the supporting matrix, thereby solving the integrity problem.

1.5 The application of GO-based films in moisture-induction

Harvesting mild and controllable energy from nature and converting it

into electrical energy for easy storage and utilization is an important research topic in the field of energy materials. When the ambient humidity changes, the energy contained in the diffusion process of gaseous water molecules from a high-concentration environment to a low-concentration environment is one of them. A GO assembly structure with functional group distribution gradient can be built, which can convert the energy in the process of environmental humidity changes into electrical energy. Novel graphene wet gas power generation materials and devices with practical application value. Using the excellent hydrophilic properties of GO materials, the ambient atmosphere can be the water molecules in the GO are effectively adsorbed on the surface of the GO assembly, forming a good ion transport channel. The ionizable functional groups in GO the ionization effect of the cluster can promote the release of ionic carriers in the GO material under the action of moisture. Gradient distribution of functional groups can drive specific directional migration of electrical carriers realizes the process of generating electricity by the interaction of GO and water molecules. by assembling GO in vivo, The optimization of chemical composition, fine structure and surface state can prepare high-performance flexible power generators based on GO wet gas power generation assemblies.
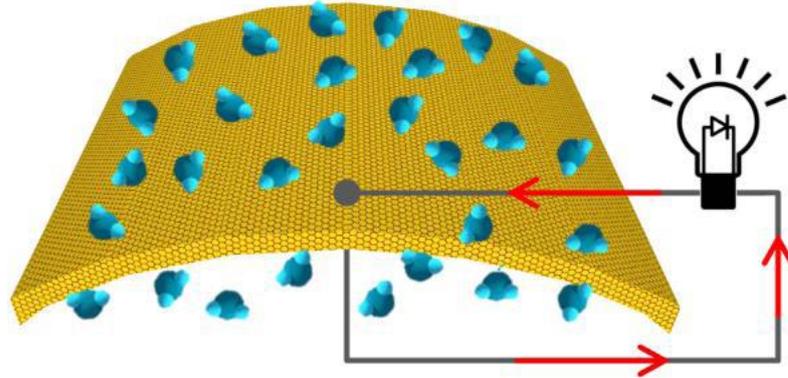
Figure 1-13 Schematic illustration of moisture enabled power generation[33]

1.5.1 GO-based films for power generators

Classical electrokinetic theory states that the flow of liquid over a thin-film electrode can generate an electrical potential [34, 35]. It was found that a voltage of 0.15 mV can be generated by the movement of water droplets of 0.6 m NaCl solution along the graphene ribbons at a constant velocity of 2.25 cm s (Figure 1-14a) [36]. The droplet stops when the induced voltage drops to zero, while it shows the same opposite sign as when the droplet moves backwards at the same speed. As shown in Figure 1-5b, Na^+ ions would adsorb on the graphene electrode and attract electrons from graphene at the droplet/graphene interface. As the droplet moves, the pseudo capacitance formed on the front side attracts electrons, while the Na^+ ions at the rear of the droplet desorb and release the pseudo capacitance. The dynamic charge-discharge process achieves that the frontal potential is higher than that of the rear. Based on this concept, a power device that

supports handwriting is reasonably designed (Figure 1-14c, 1-14d), which can be used for stroke recognition.
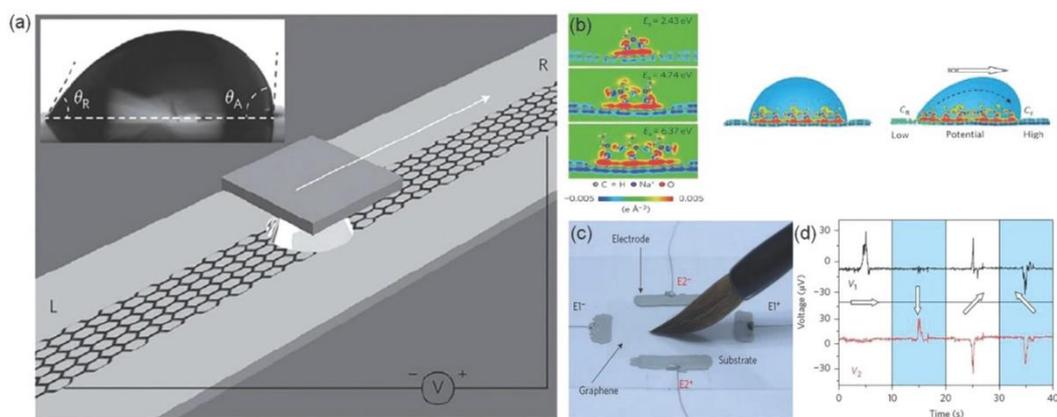
Figure 1-14 (a) The scheme of a droplet containing 0.6 M NaCl sandwiched between SiO$_2$/Si wafer and monolayer graphene. The droplet could be drawn by the moving of the wafer. The inset shows the contact angle of the droplet with advancing and receding contact angles of 91.98° and 60.28°. (b) The DFT calculation of the charge distribution of a static (left) and moving (right) droplet loaded on the graphene. (c, d) A photograph of the handwriting-recognition system and the testing results.[36]

Guo's group further reported that a wave potential could be induced in/out of NaCl aqueous solution by inserting/pulling out monolayer graphene sheets (Figure 1-15a)[37]. The voltages at the insertion and output can reach 3.3 and -3.3 mV respectively at a certain speed during the pulling process (Figure 1-15b). At a velocity of 65 cm·s^{-1}, the voltage can be increased to more than 20 mV. Electric double layer (EDL) theory sheds light on the underlying mechanism. Since the adsorption energy is positive for Na+, positive for Cl$^-$, and negative for graphene, the EDL formed at the

interface of graphene and solution (Figure 1-15c) is accompanied by hole doping of graphene. During the fast insertion and extraction cycles (Figure 1-15d), the non-equilibrium at the liquid-gas interface leads to electrons at the EDL boundary and the graphene part, respectively.
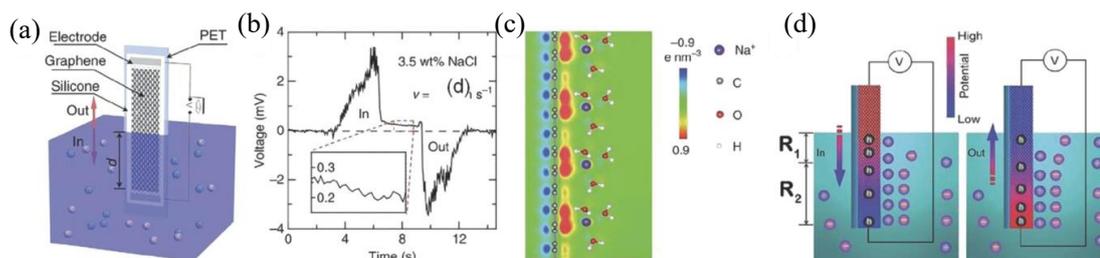
Figure 1-15 (a) (b) The typical voltage output signal of the waving potential. (c) The charge distribution of graphene when Na^+ ions were attached to the graphene.(d) Scheme of the charge distribution rearranged when the device was inserted and pulled out of the solution. [37]

Tang et al. exploited the phenomenon of electricity generation caused by π-electronation double-layer pseudo capacitance. Combining graphene electrodes with solar cells forms an all-weather sun and rain energy harvester (Figure 1-16a)[38]. All-weather solar cells can generate electricity on rainy days because the rain is full of positively and negatively charged ions. The cations (such as Na^+, NH_4^+, Ca^{2+}) in raindrops can be adsorbed on the graphene surface to drive electron migration, thereby forming π-electronation double-layer pseudo capacitors for potential and current output. As a result, the device produced a current of 0.49 μA and a voltage of 109.26 μV (Figure 1-16b,1-16c).
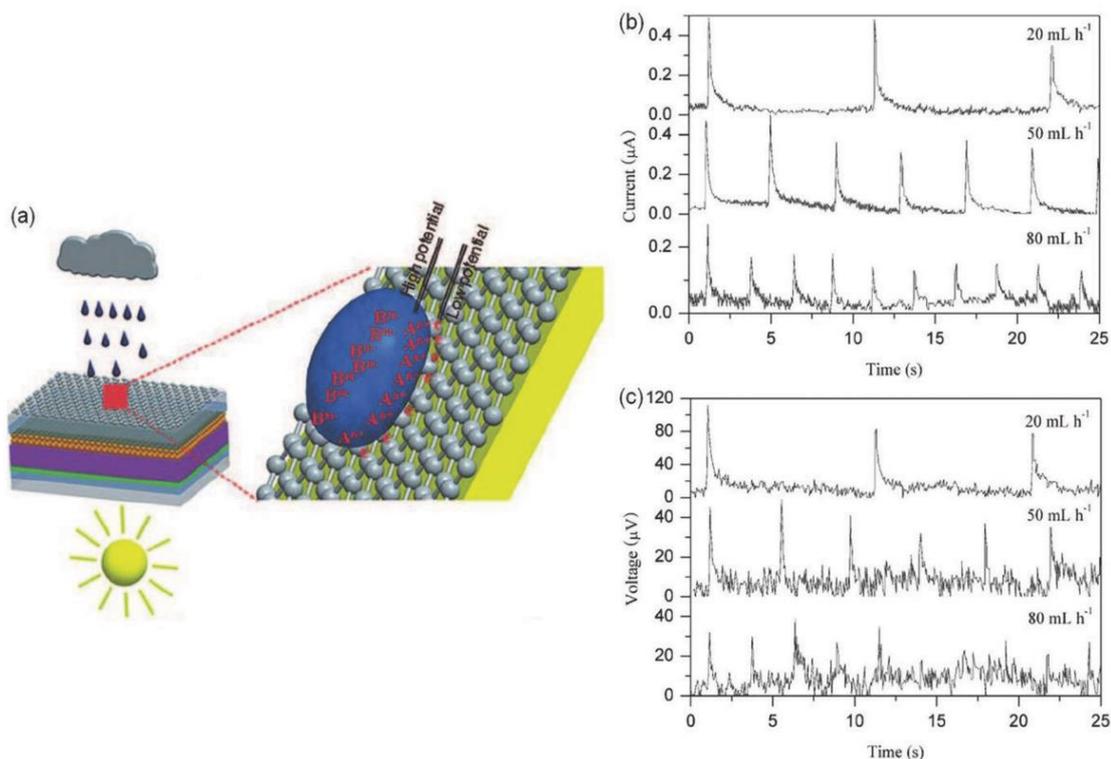
Figure 1-16 (a) Scheme showing the working principle of the all-weather solar cell. (b) Output current and (c) voltage signals produced by dropping 0.6 M NaCl solution droplets onto the device's film at different injection speeds. Reproduced with permission.[38]

In addition to this, the pristine GOF without any pretreatment or additives can directly generate voltage outputs as high as 0.4-0.7 V (Figure 1-17a). [39] Figure 1-8b shows the mechanism of the original GOF generator. When the pristine GOF is exposed to moisture, the local oxygen functional groups on the GO are ionized (Figure 1-17b–i), thereby releasing a large amount of free H^+ as a charge carrier. Then, as the water molecules gradually penetrated deep into the pristine GOF, due to the difference in proton concentration, the free H^+ ions move with the water molecules according to the Grotius's mechanism, resulting in charge

31

separation and ion-directed movement (Figure 1-17b-ii). Therefore, when the water molecules ionize enough H^+ ions in the original GOF, the induced potential and current are stable. In contrast, the expulsion of moisture reduces the number of mobile ions and accelerates the recombination of H^+ and negative functional groups in GO (Figure 1-17b-iii), resulting in reverse voltage. After the complete release of water, the original GOF will return to its original state.
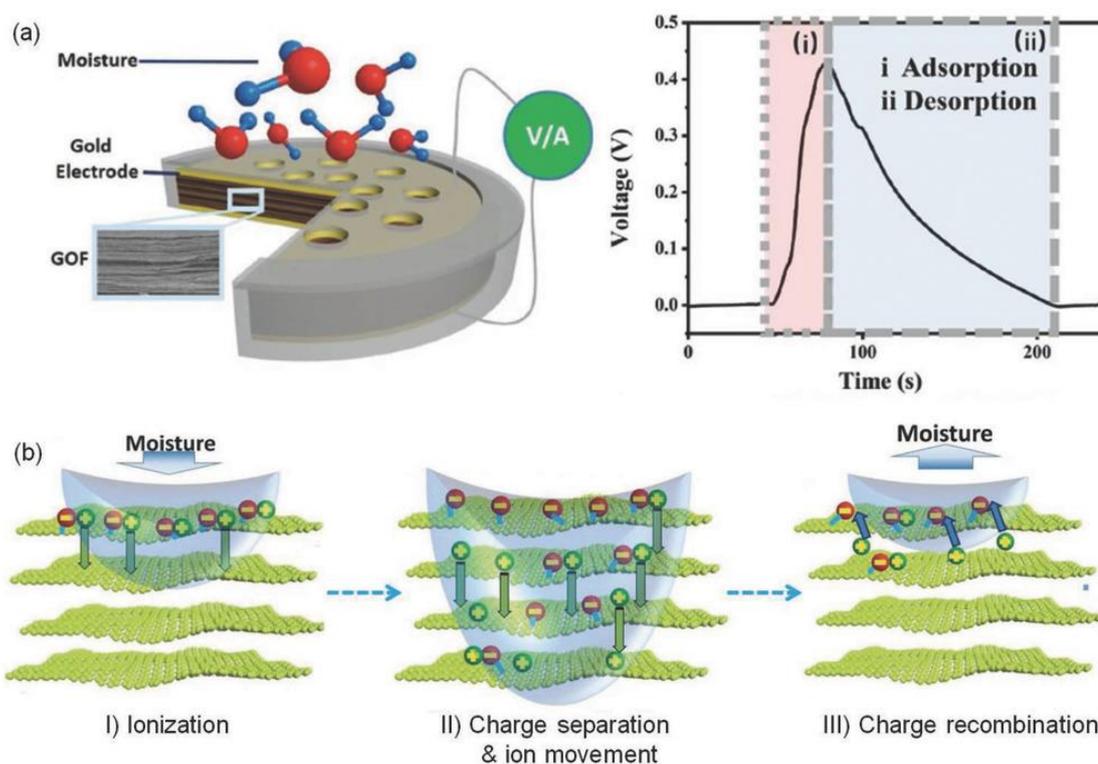
Figure 1-17 (a) Scheme showing the working principle of the all-weather solar cell. (b) Output current and (c) voltage signals produced by dropping 0.6 M NaCl solution droplets onto the device's film at different injection speeds. Reproduced with permission.[38]

Generators based on layered graphene hydrogel membranes (GHM) have also been fabricated[40]. As shown in Figure 1-18a, when an aqueous

NaCl solution (0.1 m) flows through a GHM at an air pressure of 5 kPa, the oxygen-containing groups on the surface of the GHM allow cations (Na$^+$) pass and block the anion (Cl$^-$). Therefore, ionic currents as high as 2.23 ± 0.26 nA can be monitored (Figure 1-18b). By converting hydraulic motion into flowing ionic current, GHM-based generators can directly output electricity (Figure 1-18c).
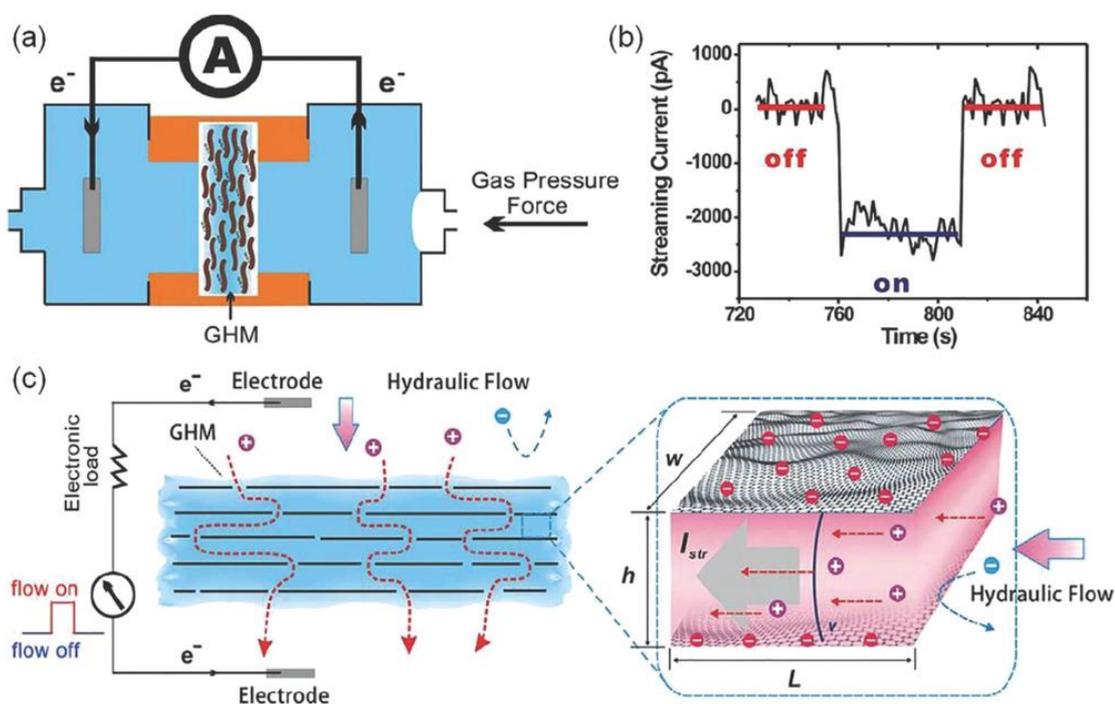
Figure 1-18 (a) The experimental setup for hydraulic-electric conversion with GHM. (b) Ionic current was caused when a 0.1 M NaCl solution flowed across the GHM. (c) Proposed mechanism for the streaming current generation. Reproduced with permission.[40]

1.5.2 GO-based films for respiratory sensors

In the past two decades, carbon nanomaterials have been widely used in the field of gas and humidity sensors, such as fullerenes and carbon

nanotubes. Sensors prepared from carbon nanomaterials as a gas-humidity active layer usually have the following advantages: (1) large specific surface area: Usually, carbonaceous nanomaterials have a larger specific surface area than homogeneous carbon materials, which increases gas molecules and activity. The contact area of the layer improves the ability to adsorb gas molecules, so the sensor constructed from it has higher sensitivity; (2) room temperature working ability: traditional semiconductor metal oxide gas humidity sensors usually require a certain working temperature, while nano carbon The gas sensor made of the material can work normally at room temperature, reducing the power consumption of the device; (3) miniaturization: the size of the nano-carbon material itself is small, and the sensor prepared from it can easily achieve miniaturization characteristics; (4) stability : Since the chemical properties of carbon nanomaterials are relatively stable at room temperature, the prepared sensor also has good stability. Wearable electronics with the ability to bend and twist with uniform stretchability [41] can be integrated with clothing[42], sensors[43], and high-tech products [44], It has important value in health monitoring [45]. Among these devices, respiration tracking devices have been widely used in the clinical diagnosis of cardiovascular and pulmonary diseases[46], since respiration is undoubtedly one of the most important vital signs.

Power generation can be enhanced by assembling graphene sheets into

macroscopic 2D films. Qu' group demonstrate for the first time that GO is an important material for power generation[47]. For example, based on a single GO thin film (GOF) with a gradient of oxygen groups (g-GOF), electricity was directly generated by harvesting energy from moisture diffusion (Figure 1-19a). The g-GOF was prepared by wet electric annealing method, and the oxygen content gradually increased from top to bottom (Figure 1-19b, 1-19c). Driven by the concentration gradient, protons spontaneously diffuse from the higher concentration region to the lower part, resulting in the potential energy of free electrons moving in the external circuit until the diffusion reaches dynamic equilibrium. Conversely, the desorption of water can promote the recombination of H^+ ions and negatively charged groups, leading to a negative potential for the reverse movement of electrons until the GO releases the remaining water molecules. As a result, the g-GOF produced a maximum moisture-triggered power density of 4.2 $mW·m^{-2}$ at an output voltage of 30 mV, surpassing some piezoelectric and fluidic generators. Based on the basic principle of gradient ion distribution, a g-GOF hydroelectric device (Figure 1-19d) was used to detect body conditions. In this case, the respiratory rate can be easily monitored by counting the number of output signals.
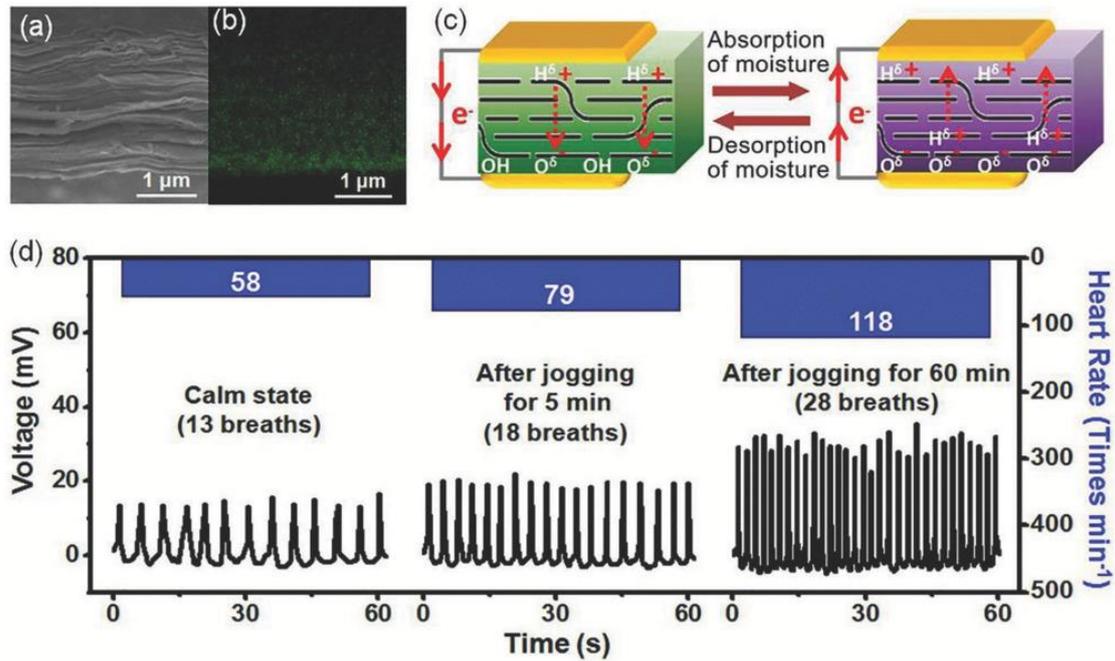
Figure 1-19 (a) Scheme showing the working principle of the all-weather solar cell. (b) Output current and (c) voltage signals produced by dropping 0.6 M NaCl solution droplets onto the device's film at different injection speeds. Reproduced with permission[38].

1.6 The purpose and significance of this work

The works above provide more application potentials in energy harvesting from moisture. However, some aspects remain unresolved. Drawbacks, such as complex manufacturing methods, expensive chemical addition demands, insufficient flexibility, and especially the rapid discharging speed, prevent the wide use of carbon materials in the green energy conversion field. And they both share a disadvantage that cannot be ignored: their generators conducted a good charging performance under high humidity but exhibited a rapid discharging behavior in low humidity. Hence, I aim to develop a new graphene oxide-based material which can

supply considerable electrical power even when transferred to a dry condition for moisture-induced electricity generator. This material also has the advantages of low cost, excellent flexibility, and ease of manufacturing. The generator based on this material can not only obtain energy from various types of moisture, such as moisture in the air, moisture in the breath, water droplets and sweat, etc., but also can be freely assembled to meet the instantaneous power supply, stable power supply, various requirements such as regulated power supply or transformer power supply.

1.7 The outline of this dissertation

The dissertation is organized to summery moisture-induced electricity generation of graphene oxide-based film by 5 chapters. And the main research is divided into three parts on the development of graphene oxide-based films and the developments of moisture-induced power generators for different kinds of moisture.

In Chapter 1, the basic properties of GO, graphene, and some common reduction methods of GO are summarized for material preparation. And the recently researched on the application of GO-based film in humidity power generation and sensors are summarized.

In Chapter 2, to develop a graphene oxide-based material with asymmetric hydrophilicity, RGF with different oxygen-containing were prepared by UV treating on the surface of GOF. And the good output

performance of RGF-based generator suggested that UV treatment is effective in making GO-based film for power generator. The generator with expandation powered a timer under wet environmental for seconds.

In Chapter 3, in order to gain a generator which can provide sustainable electricity even when moving from high humid environment to dry condition, the double-sided reduction treatment of GOF with UV is used to obtain the RGO/GO/RGO sandwich structure, which is beneficial to slow down the dehumidification of water molecules, thereby obtaining the performance of slow discharge.

In Chapter 4, based on the RGO/GO/RGO sandwich structure, CNTs are added to improve induced electricity under breath moisture. The domain design of asymmetric hydrophilicity is optimized for a breath-moisture induced power generator. This generator based on CNT added film can successfully provide sustainable electricity under intermittent exhalations.

In Chapter 5, the whole summary and conclusions of this dissertation are presented.

References

[1] A.K. Geim, K.S. Novoselov, The rise of graphene, Nature Materials 6(3) (2007) 183-191.

[2] J.H. Chen, C. Jang, S.D. Xiao, M. Ishigami, M.S. Fuhrer, Intrinsic and extrinsic performance limits of graphene devices on SiO2, Nature

Nanotechnology 3(4) (2008) 206-209.

[3] C. Lee, X.D. Wei, J.W. Kysar, J. Hone, Measurement of the elastic properties and intrinsic strength of monolayer graphene, Science 321(5887) (2008) 385-388.

[4] S. Stankovich, D.A. Dikin, G.H.B. Dommett, K.M. Kohlhaas, E.J. Zimney, E.A. Stach, R.D. Piner, S.T. Nguyen, R.S. Ruoff, Graphene-based composite materials, Nature 442(7100) (2006) 282-286.

[5] M.D. Stoller, S.J. Park, Y.W. Zhu, J.H. An, R.S. Ruoff, Graphene-Based Ultracapacitors, Nano Letters 8(10) (2008) 3498-3502.

[6] A.H. Castro Neto, F. Guinea, N.M.R. Peres, Drawing conclusions from graphene, Physics World 19(11) (2006) 33-37.

[7] K.S. Novoselov, A.K. Geim, S.V. Morozov, D. Jiang, Y. Zhang, S.V. Dubonos, I.V. Grigorieva, A.A. Firsov, Electric field effect in atomically thin carbon films, Science 306(5696) (2004) 666-669.

[8] X.S. Li, W.W. Cai, J.H. An, S. Kim, J. Nah, D.X. Yang, R. Piner, A. Velamakanni, I. Jung, E. Tutuc, S.K. Banerjee, L. Colombo, R.S. Ruoff, Large-Area Synthesis of High-Quality and Uniform Graphene Films on Copper Foils, Science 324(5932) (2009) 1312-1314.

[9] S. Stankovich, D.A. Dikin, R.D. Piner, K.A. Kohlhaas, A. Kleinhammes, Y. Jia, Y. Wu, S.T. Nguyen, R.S. Ruoff, Synthesis of graphene-based nanosheets via chemical reduction of exfoliated graphite oxide, Carbon 45(7) (2007) 1558-1565.

[10] H.A. Becerril, J. Mao, Z. Liu, R.M. Stoltenberg, Z. Bao, Y. Chen, Evaluation of solution-processed reduced graphene oxide films as transparent conductors, Acs Nano 2(3) (2008) 463-470.

[11] G. Venugopal, K. Krishnamoorthy, R. Mohan, S.J. Kim, An investigation of the electrical transport properties of graphene-oxide thin films, Materials Chemistry and Physics 132(1) (2012) 29-33.

[12] G. Eda, M. Chhowalla, Chemically Derived Graphene Oxide: Towards Large-Area Thin-Film Electronics and Optoelectronics, Advanced Materials 22(22) (2010) 2392-2415.

[13] N.V. Medhekar, A. Ramasubramaniam, R.S. Ruoff, V.B. Shenoy, Hydrogen Bond Networks in Graphene Oxide Composite Paper: Structure and Mechanical Properties, Acs Nano 4(4) (2010) 2300-2306.

[14] L. Yu, T. Grace, M. Batmunkh, M. Dadkhah, C. Shearer, J. Shapter, Insights into chemical doping to engineer the carbon nanotube/silicon photovoltaic heterojunction interface, Journal of Materials Chemistry A 5(46) (2017) 24247-24256.

[15] S.R. Kim, M.K. Parvez, M. Chhowalla, UV-reduction of graphene oxide and its application as an interfacial layer to reduce the back-transport reactions in dye-sensitized solar cells, Chemical Physics Letters 483(1-3) (2009) 124-127.

[16] D.D. Han, Y.L. Zhang, Y. Liu, Y.Q. Liu, H.B. Jiang, B. Han, X.Y. Fu, H. Ding, H.L. Xu, H.B. Sun, Bioinspired Graphene Actuators Prepared by

Unilateral UV Irradiation of Graphene Oxide Papers, Advanced Functional Materials 25(28) (2015) 4548-4557.

[17] J.I. Paredes, S. Villar-Rodil, A. Martinez-Alonso, J.M.D. Tascon, Graphene oxide dispersions in organic solvents, Langmuir 24(19) (2008) 10560-10564.

[18] A. Buchsteiner, A. Lerf, J. Pieper, Water dynamics in graphite oxide investigated with neutron scattering, Journal of Physical Chemistry B 110(45) (2006) 22328-22338.

[19] C.W. Lee, B.J. Min, S.I. Kim, H.K. Jeong, Stacking of water molecules in hydrophilic graphene oxides characterized by Kelvin probe force microscopy, Carbon 54 (2013) 353-358.

[20] S. Park, J. An, J.W. Suk, R.S. Ruoff, Graphene-Based Actuators, Small 6(2) (2010) 210-212.

[21] P.Z. Sun, M. Zhu, K.L. Wang, M.L. Zhong, J.Q. Wei, D.H. Wu, Z.P. Xu, H.W. Zhu, Selective Ion Penetration of Graphene Oxide Membranes, Acs Nano 7(1) (2013) 428-437.

[22] M. Hu, B.X. Mi, Layer-by-layer assembly of graphene oxide membranes via electrostatic interaction, Journal of Membrane Science 469 (2014) 80-87.

[23] R.R. Nair, H.A. Wu, P.N. Jayaram, I.V. Grigorieva, A.K. Geim, Unimpeded Permeation of Water Through Helium-Leak-Tight Graphene-Based Membranes, Science 335(6067) (2012) 442-444.

[24] D.A. Dikin, S. Stankovich, E.J. Zimney, R.D. Piner, G.H.B. Dommett, G. Evmenenko, S.T. Nguyen, R.S. Ruoff, Preparation and characterization of graphene oxide paper, Nature 448(7152) (2007) 457-460.

[25] J. Kim, L.J. Cote, J.X. Huang, Two Dimensional Soft Material: New Faces of Graphene Oxide, Accounts of Chemical Research 45(8) (2012) 1356-1364.

[26] H. Li, Z.N. Song, X.J. Zhang, Y. Huang, S.G. Li, Y.T. Mao, H.J. Ploehn, Y. Bao, M. Yu, Ultrathin, Molecular-Sieving Graphene Oxide Membranes for Selective Hydrogen Separation, Science 342(6154) (2013) 95-98.

[27] H.W. Kim, H.W. Yoon, S.M. Yoon, B.M. Yoo, B.K. Ahn, Y.H. Cho, H.J. Shin, H. Yang, U. Paik, S. Kwon, J.Y. Choi, H.B. Park, Selective Gas Transport Through Few-Layered Graphene and Graphene Oxide Membranes, Science 342(6154) (2013) 91-95.

[28] Y.H. Yang, L. Bolling, M.A. Priolo, J.C. Grunlan, Super Gas Barrier and Selectivity of Graphene Oxide-Polymer Multilayer Thin Films, Advanced Materials 25(4) (2013) 503-508.

[29] M. Hu, B.X. Mi, Enabling Graphene Oxide Nanosheets as Water Separation Membranes, Environmental Science & Technology 47(8) (2013) 3715-3723.

[30] D. Li, M.B. Muller, S. Gilje, R.B. Kaner, G.G. Wallace, Processable aqueous dispersions of graphene nanosheets, Nature Nanotechnology 3(2) (2008) 101-105.

[31] T. Szabo, O. Berkesi, P. Forgo, K. Josepovits, Y. Sanakis, D. Petridis, I. Dekany, Evolution of surface functional groups in a series of progressively oxidized graphite oxides, Chemistry of Materials 18(11) (2006) 2740-2749.

[32] R.K. Joshi, P. Carbone, F.C. Wang, V.G. Kravets, Y. Su, I.V. Grigorieva, H.A. Wu, A.K. Geim, R.R. Nair, Precise and Ultrafast Molecular Sieving Through Graphene Oxide Membranes, Science 343(6172) (2014) 752-754.

[33] H.H. Cheng, Y.X. Huang, F. Zhao, C. Yang, P.P. Zhang, L. Jiang, G.Q. Shi, L.T. Qu, Spontaneous power source in ambient air of a well-directionally reduced graphene oxide bulk, Energy & Environmental Science 11(10) (2018) 2839-2845.

[34] Y.X. Xu, K.X. Sheng, C. Li, G.Q. Shi, Highly conductive chemically converted graphene prepared from mildly oxidized graphene oxide, Journal of Materials Chemistry 21(20) (2011) 7376-7380.

[35] D.C. Marcano, D.V. Kosynkin, J.M. Berlin, A. Sinitskii, Z.Z. Sun, A. Slesarev, L.B. Alemany, W. Lu, J.M. Tour, Improved Synthesis of Graphene Oxide, Acs Nano 4(8) (2010) 4806-4814.

[36] J. Yin, X.M. Li, J. Yu, Z.H. Zhang, J.X. Zhou, W.L. Guo, Generating electricity by moving a droplet of ionic liquid along graphene, Nature Nanotechnology 9(5) (2014) 378-383.

[37] J. Yin, Z.H. Zhang, X.M. Li, J. Yu, J.X. Zhou, Y.Q. Chen, W.L. Guo, Waving potential in graphene, Nature Communications 5 (2014).

[38] Q.W. Tang, X.P. Wang, P.Z. Yang, B.L. He, A Solar Cell That Is Triggered by Sun and Rain, Angewandte Chemie-International Edition 55(17) (2016) 5243-5246.

[39] T. Xu, X.T. Ding, C.X. Shao, L. Song, T.Y. Lin, X. Gao, J.L. Xue, Z.P. Zhang, L.T. Qu, Electric Power Generation through the Direct Interaction of Pristine Graphene-Oxide with Water Molecules, Small 14(14) (2018).

[40] W. Guo, C. Cheng, Y.Z. Wu, Y.A. Jiang, J. Gao, D. Li, L. Jiang, Bio-Inspired Two-Dimensional Nanofluidic Generators Based on a Layered Graphene Hydrogel Membrane, Advanced Materials 25(42) (2013) 6064-6068.

[41] W. Liu, M.S. Song, B. Kong, Y. Cui, Flexible and Stretchable Energy Storage: Recent Advances and Future Perspectives, Advanced Materials 29(1) (2017).

[42] Y.N. Meng, Y. Zhao, C.G. Hu, H.H. Cheng, Y. Hu, Z.P. Zhang, G.Q. Shi, L.T. Qu, All-Graphene Core-Sheath Microfibers for All-Solid-State, Stretchable Fibriform Supercapacitors and Wearable Electronic Textiles, Advanced Materials 25(16) (2013) 2326-2331.

[43] M. Dervisevic, M. Alba, B. Prieto-Simon, N.H. Voelcker, Skin in the diagnostics game: Wearable biosensor nano- and microsystems for medical diagnostics, Nano Today 30 (2020).

[44] D.H. Kim, N.S. Lu, R. Ma, Y.S. Kim, R.H. Kim, S.D. Wang, J. Wu, S.M. Won, H. Tao, A. Islam, K.J. Yu, T.I. Kim, R. Chowdhury, M. Ying,

L.Z. Xu, M. Li, H.J. Chung, H. Keum, M. McCormick, P. Liu, Y.W. Zhang, F.G. Omenetto, Y.G. Huang, T. Coleman, J.A. Rogers, Epidermal Electronics, Science 333(6044) (2011) 838-843.

[45] Z. Lou, L.L. Wang, K. Jiang, G.Z. Shen, Programmable three-dimensional advanced materials based on nanostructures as building blocks for flexible sensors, Nano Today 26 (2019) 176-198.

[46] G. Matzeu, L. Florea, D. Diamond, Advances in wearable chemical sensor design for monitoring biological fluids, Sens. Actuator B-Chem. 211 (2015) 403-418.

[47] F. Zhao, H.H. Cheng, Z.P. Zhang, L. Jiang, L.T. Qu, Direct Power Generation from a Graphene Oxide Film under Moisture, Advanced Materials 27(29) (2015) 4351-4357.

Chapter 2: An asymmetric hydrophilic GO film for electricity generator based on UV treatment

2.1 Introduction

Harvesting energy from the environment is promising, and important choice to alleviate the energy crisis[1]. The widespread small-scale water in nature environment, which is a clean and inexhaustible new energy, has long attracted the attention of researchers[2, 3]. Based on the different forms of water, various mechanisms have been proposed to explain the origin of the power generation process[4] including flowing current[5], interfacial charge-discharge process[6], electronic resistance[7], charged ion drift [8, 9] and ion gradient induced power generation[10]. Graphene-based materials with tunable properties offer considerable opportunities for developing next-generation energy conversion devices[3, 4]. Among them, graphene oxide (GO) is rich in oxygen-related functional groups such as hydroxyl and carboxyl groups and has good application prospects[10]. Thus, GO was adopted in this study as its sufficient hydrophilicity and the ability to easily form a uniform film on the substrate[11]. Ultraviolet (UV) photoreduction of rGO, as green chemical-free and highly efficient reduction strategy, is considered feasible for the removal of OCGs on GO sheets[12-16] as Figure 2-1 shown, can easily control the reduction degree of GO, the reduction region is controllable, and it can be flexibly changed

to form a variety of oxygen gradients. Besides, GO reduction can only be triggered by photon energies larger than 3.2 eV (λ < 390 nm) in a photochemical process [17]. The reduction treatment of UV on GOF could obtain character of oxygen-containing difference, which can be used to develop a moisture-induced power generator. Interested in potential applications in electronics, energy-related devices, and smart systems, the GO based-humidity power generator is highly dependent on flexible regulation of oxygen content[18, 19].
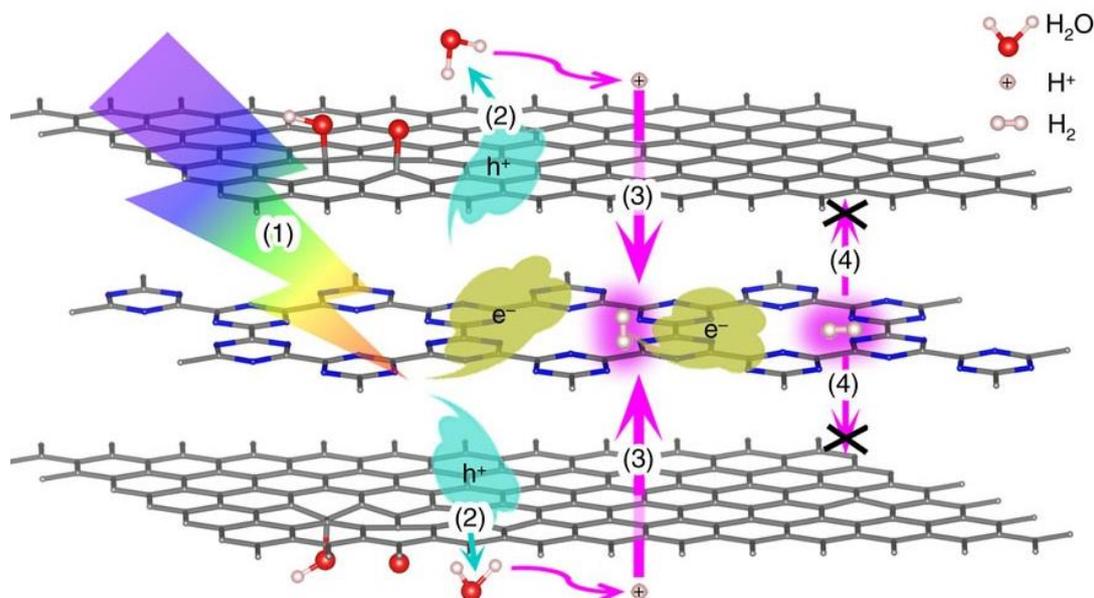
Figure 2-1 The principle of UV photoreduction on graphene oxide [13]

In this chapter, RGO/GO film (RGF) with different oxygen-containing were prepared by UV treating on the surface of GOF. The elemental composition, hydrophilicity and conductivity of the membrane surface were studied to verify the proper treatment time. To use the two-sided hydrophilic difference of RGF, the induced electricity of RGF in different

humid conditions was discussed. Besides, this character was used to develop a sandwich structural generator based on GOF and RGF, the output performance of GOF-based generator under different humid conditions suggested that UV treatment was effective to produce a GO-based film with different oxygen-containing for power generator.

2.2 Materials and methods

2.2.1 Material preparation

GO was prepared using the modified Hummers method [20]. Graphite flakes (3 g, Alfa Aesar, 7–10 μm) and $KMnO_4$ powder (18 g) were slowly added to the mixed solution of H_2SO_4 (360 mL, 98%) and H_3PO_4 (40 mL, 84%) in a 40°C-water bath. After stirring for 24h at 300rpm, H_2O_2 solution (400 mL, 0.3%) was poured into the acid liquid mixture. The hydrochloric acid solution (HCl, 200 mL, 5%) was added to the golden yellow precipitate 24 hours later. As figure 2-1 showed, the neutral GO solution was produced by centrifugation (3500 rpm, 10 min) for several times. The GO powder was obtained by a freeze-drying machine. And GO aqueous dispersion (4 mg/ml, 30 ml, ultrasound for 30 min) was placed in a glass dish (d=7cm) for vacuum drying (60°C, 3 h) to produce a piece of GO film. GO film was treaded by unilateral UV irradiation (Portable Cure 100, 100 W, 365 nm, 170 mWcm^{-2}) by 1~10 h to obtain an RGO/GO film (RGF).
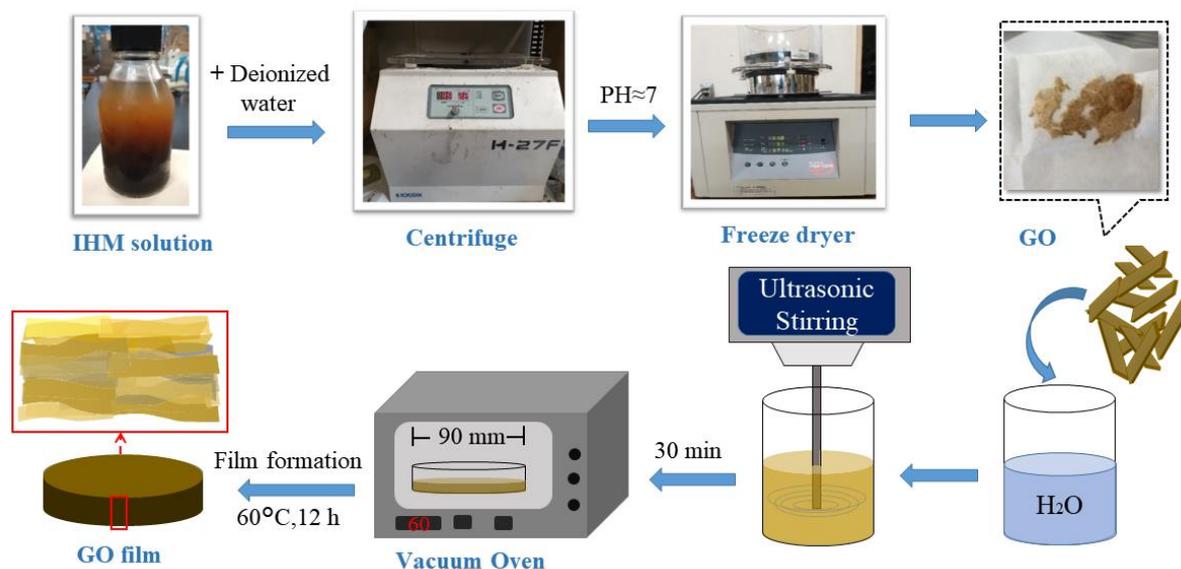
Figure 2-2 The preparation process of GO film

1 g H_3PO_4 (87%) was slowly added into the PVA solution (0.1 g/mL, 10 mL, 90°C for 2 h, 300 rmp). The H_3PO_4/PVA gel used for bridging two electrode films was dried at room temperature for 3 h. The bridge distance was 2 mm, and the bridge size was 1cm^2. To facilitate the test, two ends of the films were fixed on a transparent plastic film by conductive tape (TERAOKA808, JAPAN).

2.2.2 Characterizations and evaluations

The micromorphology of RGFs were characterized by scanning electron microscope (SEM, SU1510, Hitachi High Technologies, Japan). And the change of element composition was identified by X-Ray Diffraction Spectroscopy (XRD, scan rate 5°min^{-1}, MiniFlex300, Rigaku Co. Ltd, JPN), and Raman spectroscopy (Raman, 532 nm, JASCO NRS-3100, JPN).

The surface hydrophilic property of the film was measured by contact angle measurements (CA, Digidrop, GBX, Whitestone Way, France). A digital multimeter (GDM-8342) was used to record the voltage and current in different moisture environments to evaluate the output performance of power generation. To control the humidity, a homemade humidity cabinet was employed as Figure 2-3 shown. The room temperature was $15°C \pm 2°C$ and the ambient humidity was $25\% \pm 3\%$. In the humidity cabinet, a humidifier was used to produce wet air and control different humidity ($45\% \pm 2\%$, $65\% \pm 2\%$, and $85\% \pm 2\%$). In addition, a humidity of $5\% \pm 2\%$ was obtained by passing dry Argon into another dehumidification box with desiccant inside. The temperature of moisture could be controlled by water in a humidifier. As shown in Figure 2-3, the samples were placed horizontally and vertically in the humidification chamber, respectively. The substrate is hollow with same area of the test sample. Therefore, when tested vertically, both sides of the sample were under same humidity; while tested horizontally, only the upper side was exposed to humid air. All tests were conducted on at least three specimens to represent each sample in this study.
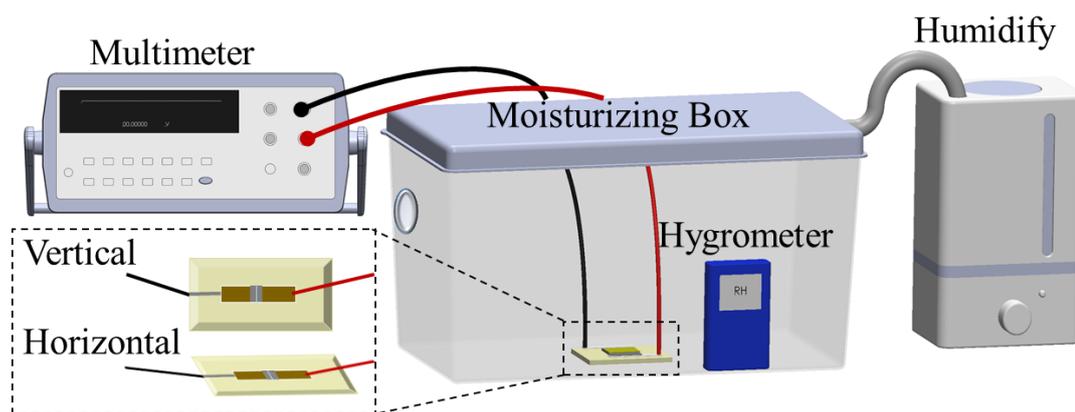
Figure 2-3 The humidity cabinet for moisture test and test methods for different samples.

2.3 Results and discussion

2.3.1 The morphology of RGF

As Figure 2-4a showed, RGF was obtained by UV treatment on one side of GOF. After the treatment, it presented metallic luster comparing to GOF in GCF in macroscopic morphology (Figure 2-4b). In microscopic morphology, all layers in GOF were tightly arranged in the cross-section (Figure 2-4c), in RGF only the untreated side showed like GOF, while the layers nearby UV-treated side had larger interlayer gaps due to the release of gas through the interlayer during the reduction process. In addition, compared with the surface micromorphology of GOF, the wrinkle on the treated side of RGF was significantly increased. This was caused by the expansion and subsequent retraction of the interlayer after carbon emission in reduction process by UV irradiation.
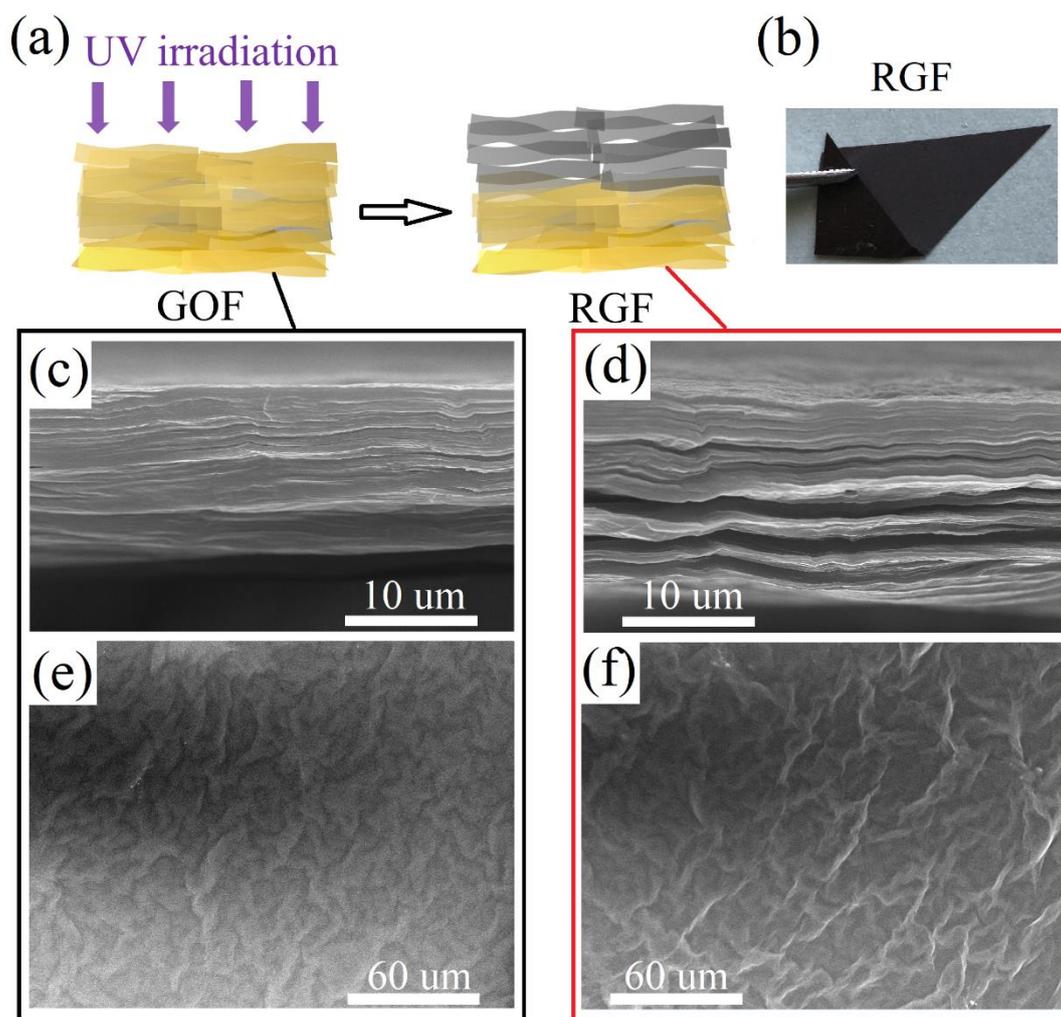
Figure 2-4 (a) The design principle schematic illustration and digital photograph of RGF. (b) The digital photo of RCF. The surface and section micromorphology of GOF (c, d) and RGF (e, f).

2.3.2 The effect of UV treatment on the structure and properties of RGF

Figure 2-5a~d shows the difference in chemical composition, surface hydrophilicity and surface conductivity between the RGF treated surface (RGF-RGOS) and the untreated surface (RGF-GOS) caused by UV

treatment. Both D-band and G-band of RGF-RGOS obviously decreased (Figure 2-5a), and the characteristic peak in $2\theta = 11.7°$ of RGF-RGOS (Figure 2-5b) also large decreased comparing with peaks of RGF-GOS because of the reduction. This made significant differences presented in the surface hydrophilicity and resistance of the two sides of RGF. In Figure 2-5c, RGF-GOS has a relatively better hydrophilicity with a CA of 54° than RGF-RGOS with a CA of 82°. In Figure 2-5d, the surface conductivity of RGF-RGOS (3.61 MΩ) was much higher than RGF-GOS (22.24 MΩ). Above all, UV treatment endowed different properties to two sides of RGF and the hydrophilic differences would bring an application potential in moisture-induced power generation.
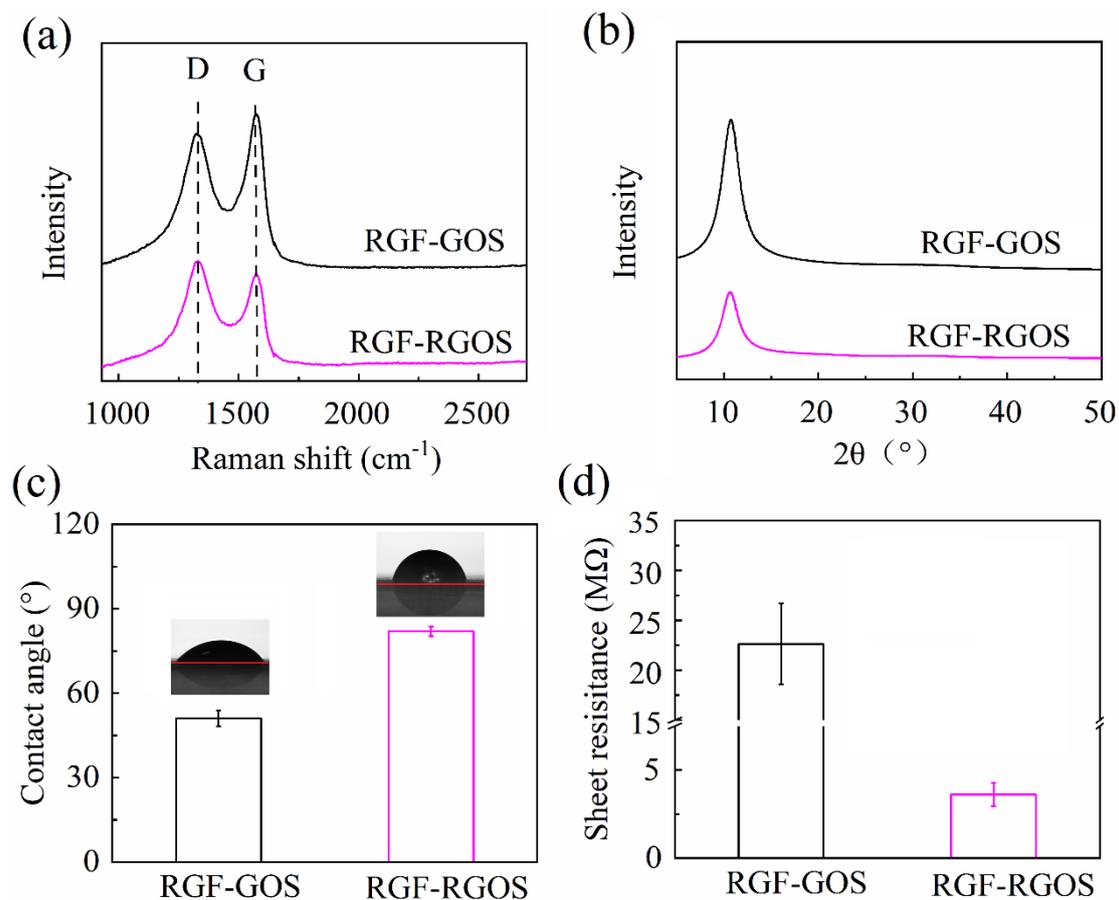
Figure 2-5 (a) XRD, (b) Raman spectra, (c) the surface hydrophilicity, and (d) sheet resistance of two sides of RGF.

2.3.4 The power performance of RGF under different humidity

To verify the hydrophilicity difference between the two sides of the RGF, induction power can be generated. As shown in Figure 2-6a, the RGF was placed in different humidity environments, and the V_{OC} and I_{SC} on both sides were measured. When RGF is placed in a humid environment, due to the difference in hydrophilicity between the two sides, the ability to absorb moisture is different. RGF-GOS absorbs more water molecules than RGF-RGOS. Freer H^+ ions are ionized from the combination of GO and water

molecules. Therefore, the formation of a difference in the concentration of H^+ ions on both sides of the RGF generates a potential difference, and the difference in the concentration of H^+ ions will cause the diffusion of H^+ ions to produce current.

In Figure 2-6b~d, RGF could generate electricity in a humid environment, and the maximum values of V_{OC} and I_{SC} obtained under high humidity are larger. Under wet air, both the voltage and current show a trend of first increasing and then decreasing. This is because in the initial stage, the humidity difference between the two sides of the RGF increases with time, and then due to the free diffusion of water molecules inside the RGF, or the RGF-GOS surface is saturated with moisture, or gradually reaches equilibrium with the ambient humidity, the humidity difference decreases, so the voltage will decrease. When current is the largest in the concentration difference of H^+ ions, the moving speed and number of H^+ ions are the largest. When the humidity difference decreases, the ion concentration difference will also decrease, resulting in a decrease in the current. As Figure 2-6a showed, V_{OC} under 85% rapidly increased to about 86 mV, and then V_{OC} decreased, and the decreasing speed became smaller as time increased; I_{SC} rapidly increased to about 2.3 uA in a few seconds, and then quickly decrease, the I_{SC} kept a lower decrease rate after 400 s and decreased slowly. RGF at 65% and 45% humidity, the V_{OC} and I_{SC} change curves are similar, and the maximum values are 43 mV and 1.4 uA (65%),

22 mV and 0.14 uA (45%), respectively. Additionally, RGF generates electricity longer under high humidity. It might be due to that the power generation mainly depends on the hydrophilic difference between GOS and RGOS of RGF. Thus, the longer the RGF generates electricity under high humidity.
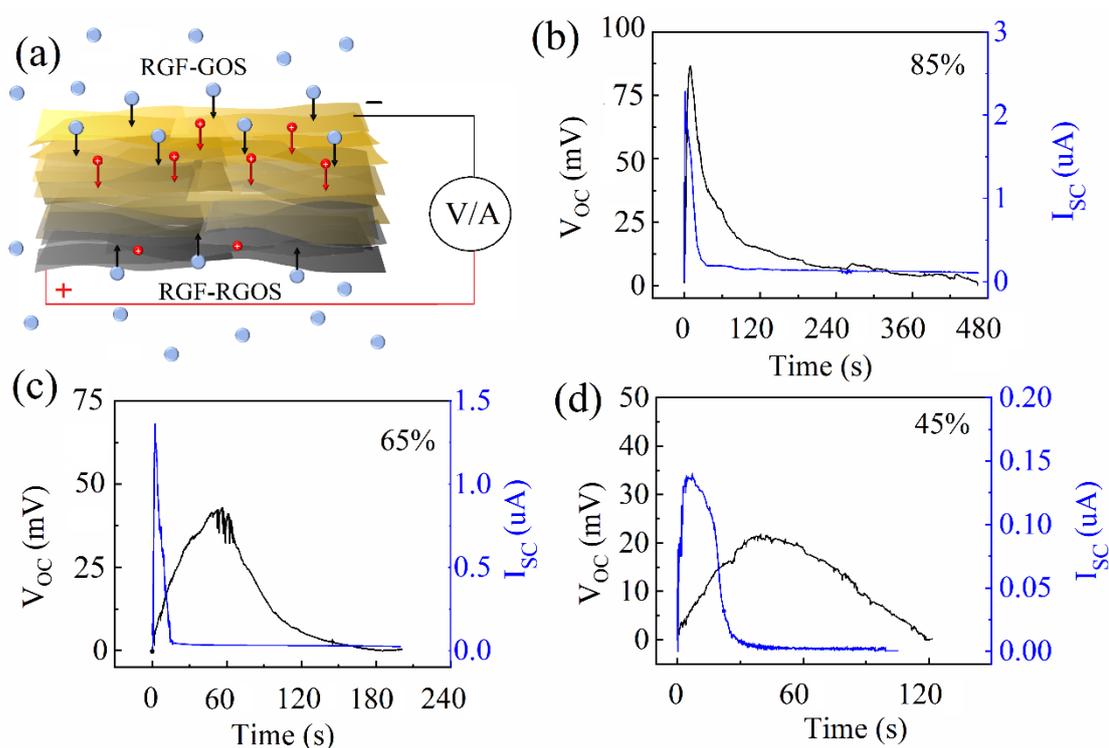
Figure 2-6 (a) The power generation mechanism and test model of RGF (vertical test). (b) The V_{OC}–t and I_{SC}–t of RGF under different humidity of 45% (b), 65% (c) and 85%(d).

2.3.5 The application of RGF in electricity generator

As shown in Figure 2-7a, a humidity electricity generator (HEG) is prepared by bridging two pieces of RGF in front and back with an electrolyte gel, where RGF is the positive electrode and GOS is the

negative electrode. In the generator, GOS can absorb more moisture than RGOS, and the diffusion path of water molecules in the HEG is from left to right（Figure 2-7）The difference in the concentration of H+ ions due to the difference in the content of water molecules in the GOF and GCF will drive the H+ ions in the electrolyte to form a directional movement.
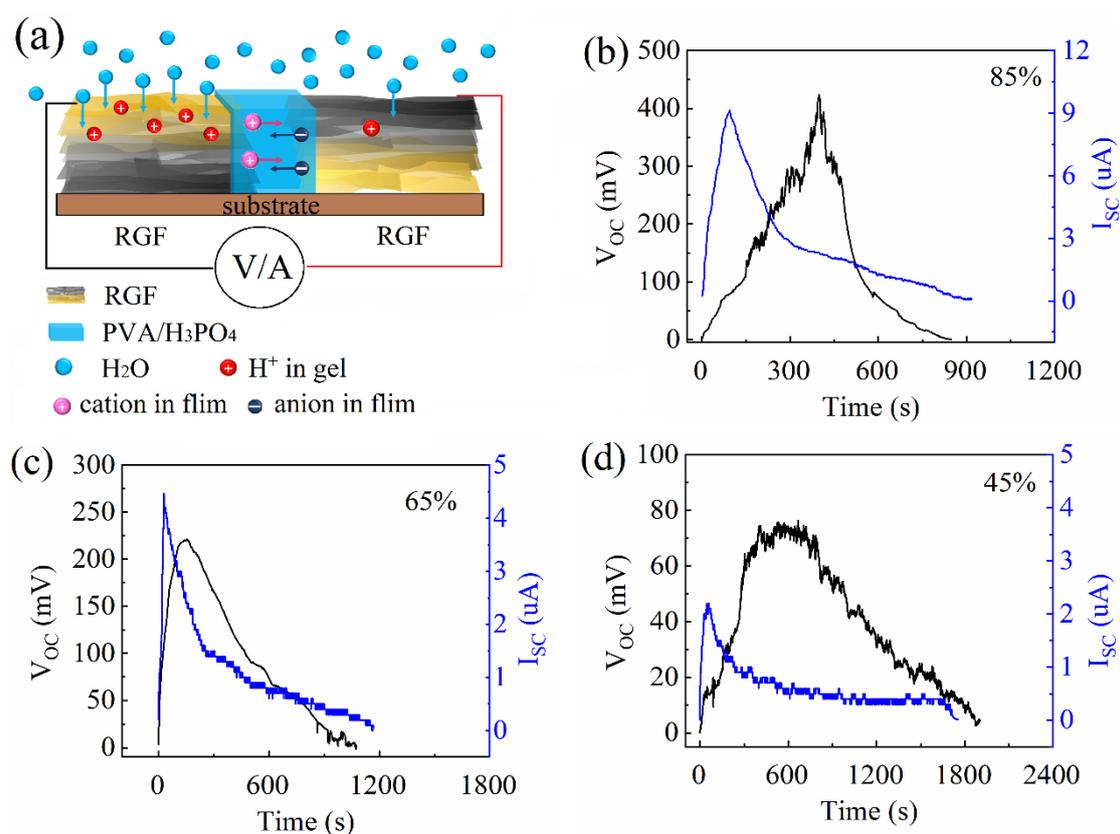
Figure 2-7 (a) The power generation mechanism and test model of HEG (horizontal test). (b) The V_{OC}–t and I_{SC}–t of HEG under different humidity of 45% (b), 65% (c) and 85%(d).

As Figure 2-7b~d showed, the maximum V_{OC} and I_{SC} values obtained at different humidity increased with increasing humidity, respectively 424 mv, 9.1 uA (85%), 215 mv, 4.5 uA (65%), and 76 mv, 2.2 uA (45%). However, the power generation time decreased with the increase of humidity, which

was different to RGF (Figure 2-7). This might be cause by that HEG mainly relied on the surface GOF to absorb water, and the ability of GOF to absorb water was limited. Under high humidity, GOF was easier to reach moisture saturation, so the power generation time was shorter.

The six pieces of HEGs (6-HEGs) was connected as Figure 2-8 showed. According to the principle of series-parallel power supply, the series voltage of is 6-HEGs about four times that of a single HEG, about 1.6 V; and the parallel current is improved to three times which is about 27 uA. Since the power required to light a timer is about 1.5V and 25 uA, as Figure 2-8d presented, 6-HEGs did power the timer for seconds. In addition, HEG is soft and has good flexibility in both X and Y directions (Fig. 2-8b). This shows the application potential of HEG to power small wearable electronic devices. However, the power supply time in a humid environment is short, so HEG needs to be further improved to achieve sustainable power supply.

Figure 2-8 (a)The schematic of 6-HEGs in expansion, (b) the digital photo of 6-HEGs under bending, (c-d) the digital photos of 6-HEGs to power a timer (V > 1.5 V, I > 25 um) under 85%

2.4 Conclusions

In this chapter, GOF was reduced by UV irradiation for 3 h. The RGF has considerable hydrophilicity and conductivity differences in its two surfaces, which endow it the application potential in moisture-induced power generation that RGF could generated electricity in humid environment. A single RGF-based HEG can generated electricity of 424 mV, 9.2 uA. And the expansion can help to HEG to power a timer for a short time, showing the potential in the field of small electronics. The UV reduced GO-based film with the hydrophilic difference is very promising in moisture induced electricity, and further use can be done to employ UV treated GO-based films for more applications.

Reference

[1] C.H. Jung, J.H. Hong, J.M. Jung, I.T. Hwang, C.H. Jung, J.H. Choi, Preparation of sulfonated reduced graphene oxide by radiation-induced chemical reduction of sulfonated graphene oxide, Carbon Letters 16(1) (2015) 41-44.

[2] G.H. Liu, T. Chen, J.L. Xu, K.Y. Wang, Blue energy harvesting on nanostructured carbon materials, Journal of Materials Chemistry A 6(38) (2018) 18357-18377.

[3] T. Xu, Q. Han, Z.H. Cheng, J. Zhang, L.T. Qu, Interactions between Graphene-Based Materials and Water Molecules toward Actuator and Electricity-Generator Applications, Small Methods 2(10) (2018).

[4] Y.F. Xu, P.N. Chen, H.S. Peng, Generating Electricity from Water through Carbon Nanomaterials, Chemistry-a European Journal 24(24) (2018) 6287-+.

[5] G.B. Xue, Y. Xu, T.P. Ding, J. Li, J. Yin, W.W. Fei, Y.Z. Cao, J. Yu, L.Y. Yuan, L. Gong, J. Chen, S.Z. Deng, J. Zhou, W.L. Guo, Water-evaporation-induced electricity with nanostructured carbon materials, Nature Nanotechnology 12(4) (2017) 317-321.

[6] Q.W. Tang, X.P. Wang, P.Z. Yang, B.L. He, A Solar Cell That Is Triggered by Sun and Rain, Angewandte Chemie-International Edition 55(17) (2016) 5243-5246.

[7] P. Kral, M. Shapiro, Nanotube electron drag in flowing liquids, Physical

Review Letters 86(1) (2001) 131-134.

[8] P. Dhiman, F. Yavari, X. Mi, H. Gullapalli, Y.F. Shi, P.M. Ajayan, N. Koratkar, Harvesting Energy from Water Flow over Graphene, Nano Letters 11(8) (2011) 3123-3127.

[9] J. Yin, Z.H. Zhang, X.M. Li, J.X. Zhou, W.L. Guo, Harvesting Energy from Water Flow over Graphene?, Nano Letters 12(3) (2012) 1736-1741.

[10] F. Zhao, H.H. Cheng, Z.P. Zhang, L. Jiang, L.T. Qu, Direct Power Generation from a Graphene Oxide Film under Moisture, Advanced Materials 27(29) (2015) 4351-4357.

[11] X.Y. Fu, L.L. Wang, L.J. Zhao, Z.Y. Yuan, Y.P. Zhang, D.Y. Wang, D.P. Wang, J.Z. Li, G.Z. Shen, W. Han, Controlled Assembly of MXene Nanosheets as an Electrode and Active Layer for High-Performance Electronic Skin, Advanced Functional Materials 31(17) (2021).

[12] P. Kumar, K.S. Subrahmanyam, C.N.R. Rao, Graphene Produced by Redation-Induced Reduction of Graphene Oxide, International Journal of Nanoscience 10(4-5) (2011) 559-566.

[13] P. Kumar, B. Das, B. Chitara, K.S. Subrahmanyam, K. Gopalakrishnan, S.B. Krupanidhi, C.N.R. Rao, Novel Radiation-Induced Properties of Graphene and Related Materials, Macromolecular Chemistry and Physics 213(10-11) (2012) 1146-1163.

[14] D.D. Han, Y.L. Zhang, Y. Liu, Y.Q. Liu, H.B. Jiang, B. Han, X.Y. Fu, H. Ding, H.L. Xu, H.B. Sun, Bioinspired Graphene Actuators Prepared by

Unilateral UV Irradiation of Graphene Oxide Papers, Advanced Functional Materials 25(28) (2015) 4548-4557.

[15] X.H. Tai, S.W. Chook, C.W. Lai, K.M. Lee, T.C.K. Yang, S. Chong, J.C. Juan, Effective photoreduction of graphene oxide for photodegradation of volatile organic compounds, Rsc Advances 9(31) (2019) 18076-18086.

[16] G. Williams, B. Seger, P.V. Kamat, TiO2-graphene nanocomposites. UV-assisted photocatalytic reduction of graphene oxide, Acs Nano 2(7) (2008) 1487-1491.

[17] V.A. Smirnov, A.A. Arbuzov, Y.M. Shul'ga, S.A. Baskakov, V.M. Martynenko, V.E. Muradyan, E.I. Kresova, Photoreduction of graphite oxide, High Energy Chemistry 45(1) (2011) 57-61.

[18] W. Gao, N. Singh, L. Song, Z. Liu, A.L.M. Reddy, L.J. Ci, R. Vajtai, Q. Zhang, B.Q. Wei, P.M. Ajayan, Direct laser writing of micro-supercapacitors on hydrated graphite oxide films, Nature Nanotechnology 6(8) (2011) 496-500.

[19] H.H. Cheng, Y. Hu, F. Zhao, Z.L. Dong, Y.H. Wang, N. Chen, Z.P. Zhang, L.T. Qu, Moisture-Activated Torsional Graphene-Fiber Motor, Advanced Materials 26(18) (2014) 2909-2913.

[20] D.C. Marcano, D.V. Kosynkin, J.M. Berlin, A. Sinitskii, Z.Z. Sun, A. Slesarev, L.B. Alemany, W. Lu, J.M. Tour, Improved Synthesis of Graphene Oxide, Acs Nano 4(8) (2010) 4806-4814.

Chapter 3：A sustainable environmental moisture-induced electricity generator based on sandwich structural GO film

3.1 Introduction

Access to energy from the environment is conducive to solving global energy shortage [1-3]. Water vapor or moisture widespread in nature is a renewable environmentally friendly green energy [4]. In 2001, Petr Kral propounded that voltage could be induced when liquid flows through carbon nanotubes in theory [5]. This theory was confirmed by Shankar Ghosh in 2003 [6], and he also clarified the exponential relationship between the voltage and flow rate of the solution. Afterward, further studies, such as B. N. J. Persson [7], S. H. Lee [8], L.F. Sun [9], and Jeff W. Baur [10], have been conducted. In 2011, Dhiman et al. [11] found that the immersion of graphene in a flowing dilute hydrochloric acid solution could produce a higher voltage signal. Han [12] suggested that the polarity of the solvent was highly correlated with voltage. In 2014, Yin et al. found that dropping ions onto bands of single-layer graphene could generate tens of millivolts of voltage, which was called "attraction potential" [13]. Subsequently, research on the interaction of different graphene materials with flowing liquids for power generation, such as reduced graphene oxide (GO) films [14], porous graphene [10, 15, 16], and banded graphene [17], was popularly conducted. Afterward, asymmetric moisturizing [18–20],

moisture-driven electrolyte diffusion, or microfluidic of carbon materials was used in harvesting energy from moisture. For example, Luo et al. [21] added $CaCl_2$ into the carbon nanotube electrodes on one side as moisture-absorbing chemicals. The device cannot be reused as ions in additives only move unidirectionally. Zhao [22] reported a GO-based three-dimensional power generator with GO with asymmetrical oxygen-containing groups (OCGs) enabled. The generator could produce an instantaneous voltage of about 200 mV, which disappears in 10 s if no moisture is supplied. Liu [23] treated porous carbon film by regional plasma treatment to endow the device with different functional group contents on two sides. It produced a voltage of hundreds of millivolts that decreased to zero within few minutes under a dry condition. Xu et al. [24] used a pristine GO film to generate electricity from moisture for the first time. The device generated a high open-circuit voltage but also exhibited a rapid discharging behavior. Their works provide more application potentials in energy harvesting from moisture. However, some aspects remain unresolved. Drawbacks, such as complex manufacturing methods, expensive chemical addition demands, insufficient flexibility, and especially the rapid discharging speed, prevent the wide use of carbon materials in the green energy conversion field.

In the previous chapter, UV treatment was effective to produce RGF for the use of the power generator. But the RGF-based generator presented similar weak point that it cannot provide sustainable electricity. Here, I try

to use UV treatment to gain a sandwich structural GO-based film which can store moisture inside in the dehumidification by treating two sides of a GO film. It was region functionalized by UV irradiation treatment to gain two special films—reduced graphene oxide/ graphene oxide /reduced graphene oxide (RGO/GO/RGO) sandwich-like structural film (RGRSF) and RGRSF–GO composite films. The generator was simply fabricated by bridging two films with H_3PO_4/polyvinyl alcohol (PVA) gels. The generator could quickly self-charge under humidity and discharge slowly under dry conditions. A simple expansion could make MIEGs successfully power a LED under moisture, and kept it lit for 1 h even when transferred to a dry condition. In addition, MIEG had remarkable endurance, considerable flexibility, and good reusability.

3.2 Materials and methods

3.2.1 Preparations of films and MIEG

GO was prepared using the modified Hummers method [25] from natural graphite flake (Alfa Aesar, 7–10 μm). Figure 3-1 shows the preparation process of GO film. 0.24 g GO was dissolved in 30 ml distilled water by ultrasound treatment for 30 min. The solution was placed in a glass dish with a diameter of 7cm under vacuum drying at 60°C for 3 h to obtain GO film (20 um). Portable Cure 100 (HLR100T-2, Sen Lights Corp., Japan) with a high-pressure UV lamp (100 W, 365 nm, 170 mWcm^{-2}) was

used as a UV light source. Two sides of the GO film (30 mm × 10 mm) were treated by UV irradiation at room temperature to obtain RGRSF. The samples treated for 1, 3, 5, and 10 h were labeled as UV-1, UV-3, UV-5, and UV-10, respectively. The GO film was region shielded by an opaque plate in the bilateral UV irradiation treatment. The shielded and treated parts are GO and RGRSF, respectively. The treated film is called RGRSF–GO composite film. Different shield sizes mean the proportions of GO in a total RGRSF–GO composite film (30 mm × 10 mm), recorded as 1/1, 1/2, 1/3, and 1/5.

1 g PVA was dissolved in 10-mL distilled water under 90°C for 2 h, 300 rpm. In addition, 1 g H_3PO_4 was slowly added to the solution at room temperature to obtain H_3PO_4/PVA gel. For further use, the gel was dried at room temperature for 3 h. H_3PO_4/PVA gel (10 mm × 10 mm) was used to bridge RGRSF and RGRSF–GO composite films, and the bridge distance was 2 mm. To facilitate the test, two ends of the films were fixed on a transparent plastic film by conductive tape 808 (TERAOKA, JAPAN).

3.2.2 Characterizations and evaluations

The RGRSFs were characterized by scanning electron microscope (SEM, SU1510, Hitachi High Technologies, Japan), X-Ray Diffraction Spectroscopy (XRD, scan rate 5°min^{-1}, MiniFlex300, Rigaku Co. Ltd, JPN), and Raman spectroscopy (Raman, 532 nm, JASCO NRS-3100, JPN). X-ray photoelectron spectroscopy (XPS, AXIS-ULTRA DLD, KRATOS,

JPN) was performed to identify the change of element composition. The hydrophilic property of RGRSFs was measured by contact angle (CA) measurements (CA, Digidrop, GBX, Whitestone Way, France). The resistivity measurement (UPMCP−450, Mitsubishi Chemical Analytech Co., JPN) was adopted to test resistivities of RGRSFs treated for different times. A multimeter (GDM-8342) was used to record the voltage and current in different moisture environments to evaluate the output performance of MIEGs. To control the humidity, a homemade humidity cabinet was employed as Figure 3-2 shown. The room temperature was 15°C ± 2°C and the ambient humidity was 30% ± 3%. In the humidity cabinet, a humidifier was used to produce wet air and control different humidity (45% ± 2%, 65% ± 2%, and 85% ± 2%) in 15 °C. In addition, a humidity of 5% ± 2% was obtained by passing dry N_2 gas into another dehumidification box with desiccant inside. The temperature of moisture could be controlled by water in a humidifier. All tests were conducted on at least three specimens to represent each sample in this study.
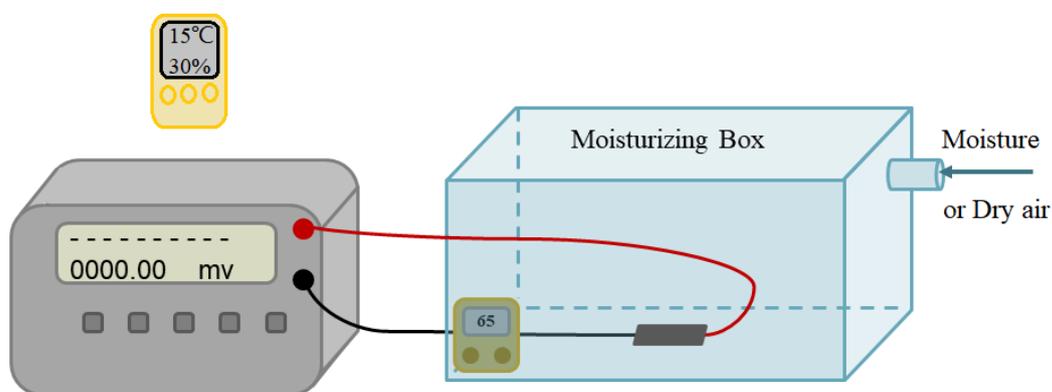

Figure 3-1 The humidity cabinet for moisture test

3.3 Results and discussion

3.3.1 The effect of bilateral UV treatment on the morphology of films

The OCGs in GO film can be reduced under the action of UV radiation (Figure 3-2a). Based on Sun's research [26], the reduction reaction of UV radiation is limited by light transmittance and thermal relaxation. Consequently, if GO film is treated by UV irradiation for a suitable time, the organic carbon (OCG) in the intermediate layer can survive to form an RGRSF [27-32]. Further, an RGRSF–GO composite film can be obtained by region bilateral shielding of GO film in the process of treatment, where the shielded and exposed parts are GO and RGRSF, respectively. From the digital photo of RGRSF–GO composite film in Figure 3-2a, two colors were observed—RGRSF part had metallic luster color and GO part was black. The surface and cross-sectional micromorphology images of GO film and RGRSF are shown in Figure 3-2b. In the top-view SEM images, GO film had only a few wrinkles but became rough after UV irradiation. In the cross-sectional SEM images, two films both showed clear layered stack structure. The layers in GO film were still tightly packed. However, RGRSF exhibited a sandwich-like layer structure, which an obvious layer spacing appeared in the outer layers on both sides. Besides, the thickness of RGRSF increased after UV irradiation. The expansion of the layers resulted from the photoreduction-induced carbon emission [26, 33].
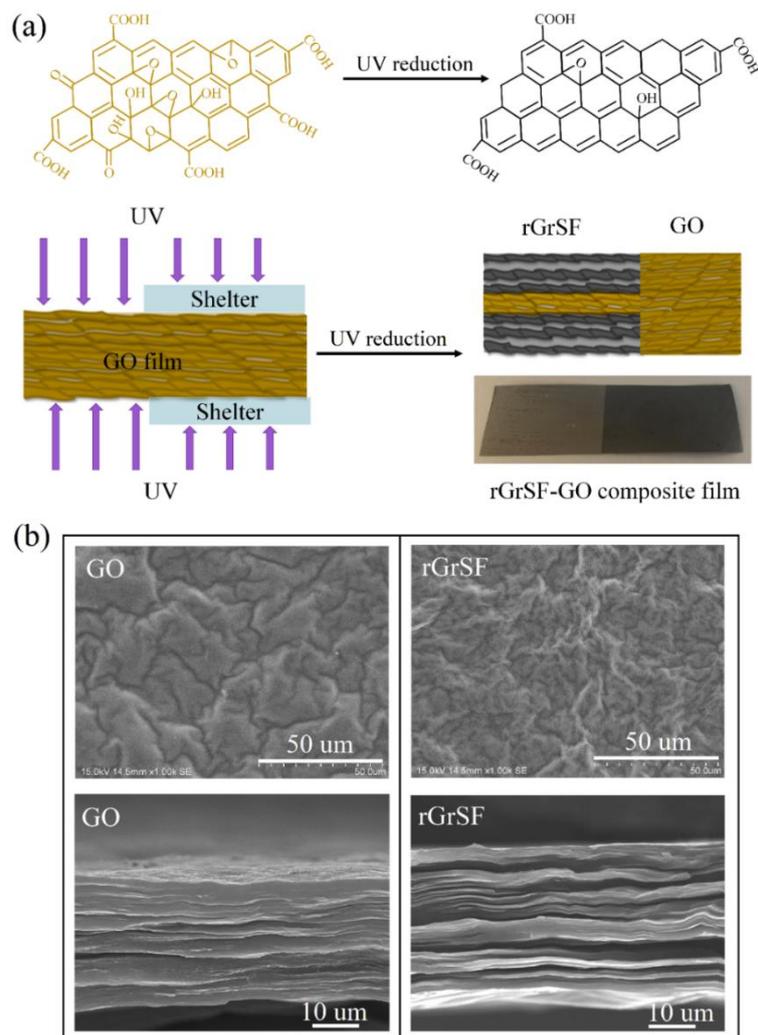
Figure 3-2 (a) The design principle schematic illustration and digital photograph of RGRSF–GO composite films. (b) The surface and section micromorphology of GO and RGRSF.

3.3.2 The effect of treatment time on the structure and properties of film

To evaluate the influence of treatment time on the reduction degree, elemental composition analysis of RGRSFs with different treatment times was measured (Figures 3-5a and 4b). In Figure 3-4a, the C1s spectrum

could be divided into three characteristic peaks: C–C (284.3 eV), C–O (266.2 eV), and C=O (288.2 eV). The weakening of C–O and C=O peaks and the strengthening of C–C peak represented the removal of OCG due to photoreduction. In Figure 3-3b, as the UV irradiation time increased, the intensity of O1s peak at 525–545 eV decreased, and the C1s peak at 280–300 eV strengthened. Notably, the atomic ratio of oxygen atoms to carbon atoms has gradually decreased from 0.48 (GO) to 0.16 (UV-10), indicating an increase in the reduction degree. Figures 3-4c and 4d present the XRD and Raman spectroscopy used to study the structural change. In Figure 3-3c, all films have a typical peak at $2\theta = 11.5°$, which is the crystal face (001) of the characteristic peak for exfoliated GO [30, 33]. The peak became weaker with the increase of treatment time owing to the interlayer peeling and increase of disorder [34, 35]. GO and RGRSFs (UV-1–UV-10) have two characteristic peaks D-band at 1321 cm^{-1} and G-band at 1572 cm^{-1} (Figure 3-3d). The D and G bands represent the breathing modes of rings with activation by defects and the in-plane bond stretching motion of sp2 C–C bond [36]. The D-band became stronger and the peak intensity ratio of the D-band to G-band (I_D/I_G) gradually increased from 0.90 (GO) to 1.25 (UV-10). These changes express the increase of smaller size graphene-like domains and the existence of more abundant structures [37, 38].
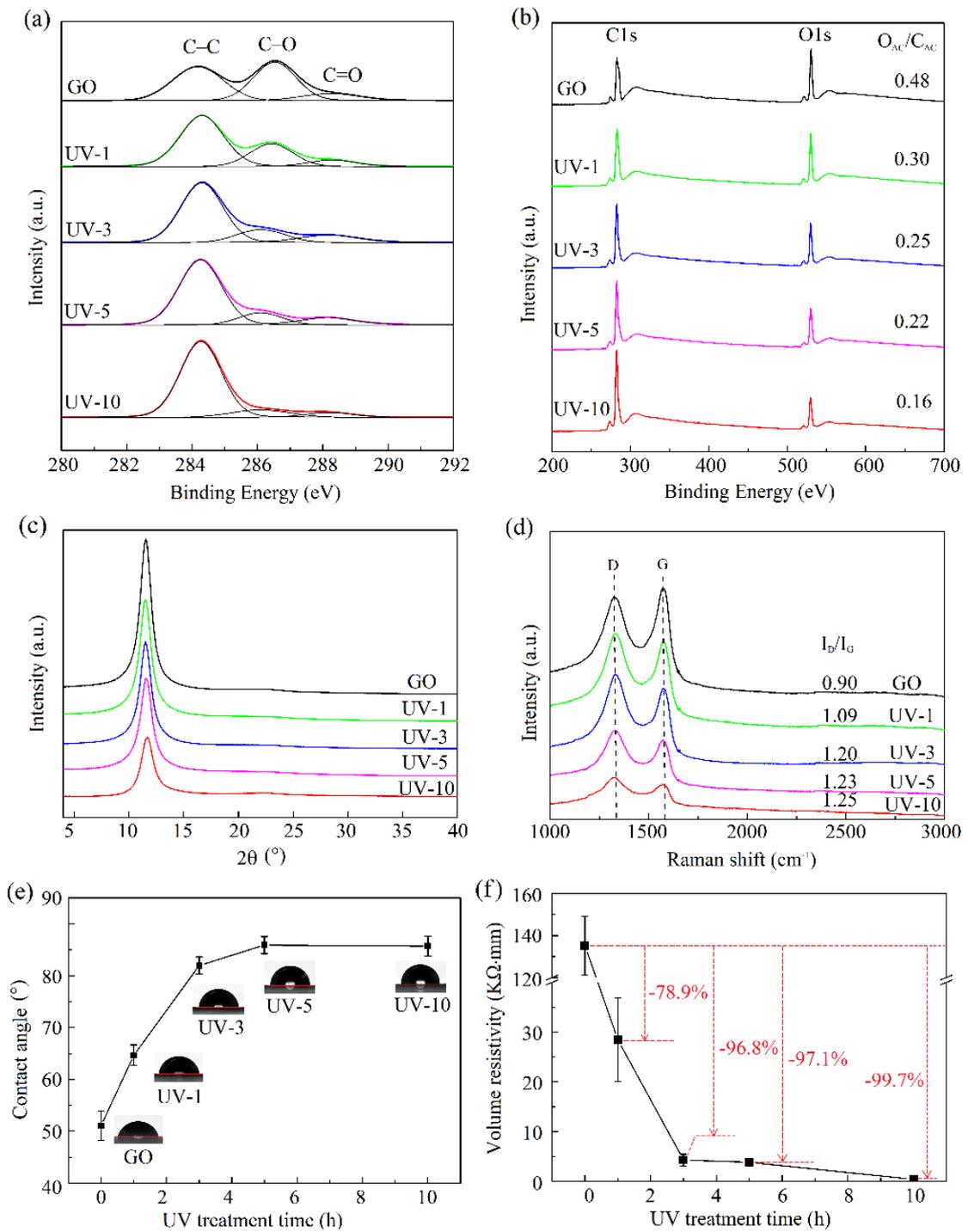
Figure 3-3 (a) C1s spectra, (b) survey XPS spectra, (c) XRD, (d) Raman spectra, (e) the surface hydrophilicity, and (f) volume resistivity of RGRSFs with different UV irradiation treatment times.

The surface hydrophilicity makes sense for MIEG. The hydrophilicity

of RGRSF can be modulated by UV treatment time. In Figure 3-3e, GO film has a relatively good hydrophilicity with a CA of 48°. After treatment, the CAs become larger, which was caused by the removal of the hydrophilic OCG and the membrane decrease of surface energy [39, 40]. For UV-3 with a CA of 82°, the hydrophobicity was significantly improved compared with GO film. The reduction of resistance would help reduce the internal energy consumption of MIEG during power generation. In Figure 3-3f, the conductivity increased after treatment that the resistivity of UV-3 film was about 4.3 $K\Omega \cdot mm$, reducing by 96.8% compared with GO film.

3.3.3 The Innovation of MIEG

As Figure 3-4 shown, only UV-1 and UV-3 presented sandwich-like structures in which GO layers were tightly packed in the middle and rGO layers exhibited obvious interlayer gaps in the outer layers on both sides. When the treatment time was longer than 3 h, the GO sheets located in the inner layer of the GO film were also reduced, resulting in the inability to form the RGO/GO/RGO sandwich structure.
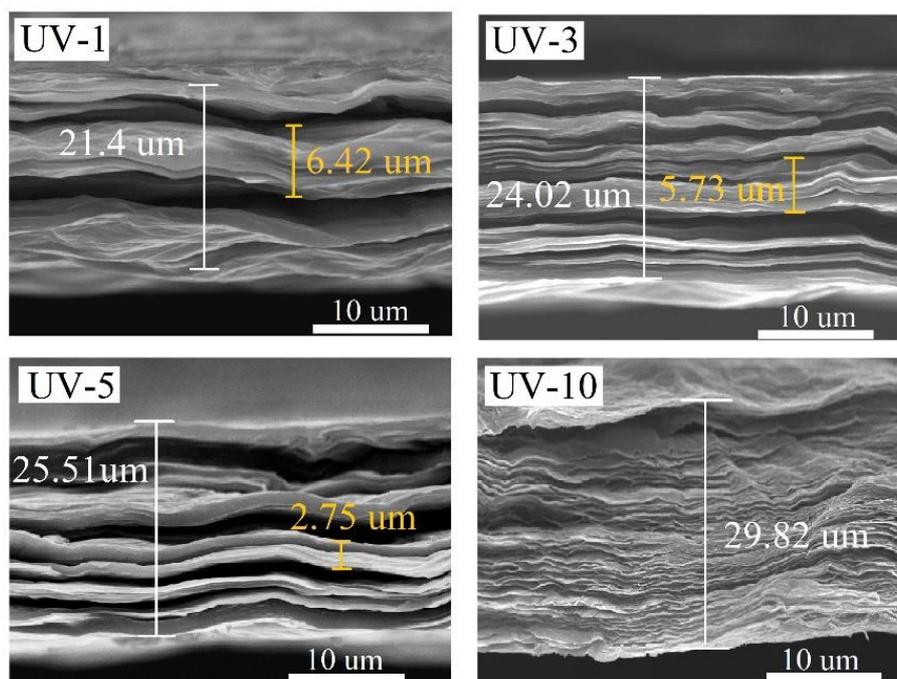
Figure 3-4 The section morphologies of RGRSFs with different UV irradiation treatment times.

As Figure 3-5a shown, MIEG in which was fabricated, in which the positive and negative electrode materials are the RGRSF–GO and RGRSF composite films, respectively. Since the hydrophilicity of GO and RGO/GO/RGO sandwich structure make sense on the output of MIEG, the size ratio of untreated part in RGRSF–GO composite films (S_{GO}/S_{total}), the region size of GO and the total size of MIEG were evaluated to optimize preparation parameters. Their open-circuit voltage (V_{OC}) under a humidity of 85% for 1 h were recorded in Figure 3-5b, 6c and 6d. The d_{GO}/d_{total} of UV-1 (0.326), UV-3 (0.273), UV-5 (0.122) and UV-10 (0.0452), gradually decreased with the treatment time (Figure 3-5b). The V_{OC} of UV-3 is largest resulted from the large content of GO that could release much more free

H^+ ions when combined with water molecules, and its sandwich structure facilitates the directional water diffusion to promote the movement of free ions. When S_{GO}/S_{total} is 1/4, the V_{OC} with a value of 215.7 mV, was the largest (Figure 3-5c). The decrease in the V_{OC} of 1/6 resulted from its poor water potential energy which could not drive the movements of many ions. However, for V_{OC} of 1/3 and 1/4, water molecules might prefer to diffusing along the thickness direction in GO region as their large content of GO. Further, the size expansion of MIEG was conducive to providing larger voltage (Figure 3-5d). For comprehensive considerations of the section structure, performances, and energy, the UV treatment time, S_{GO}/S_{total} and the size of is recommended as 3 h, 1/4 and 6 cm^2 to prepare MIEGs in the following tests.
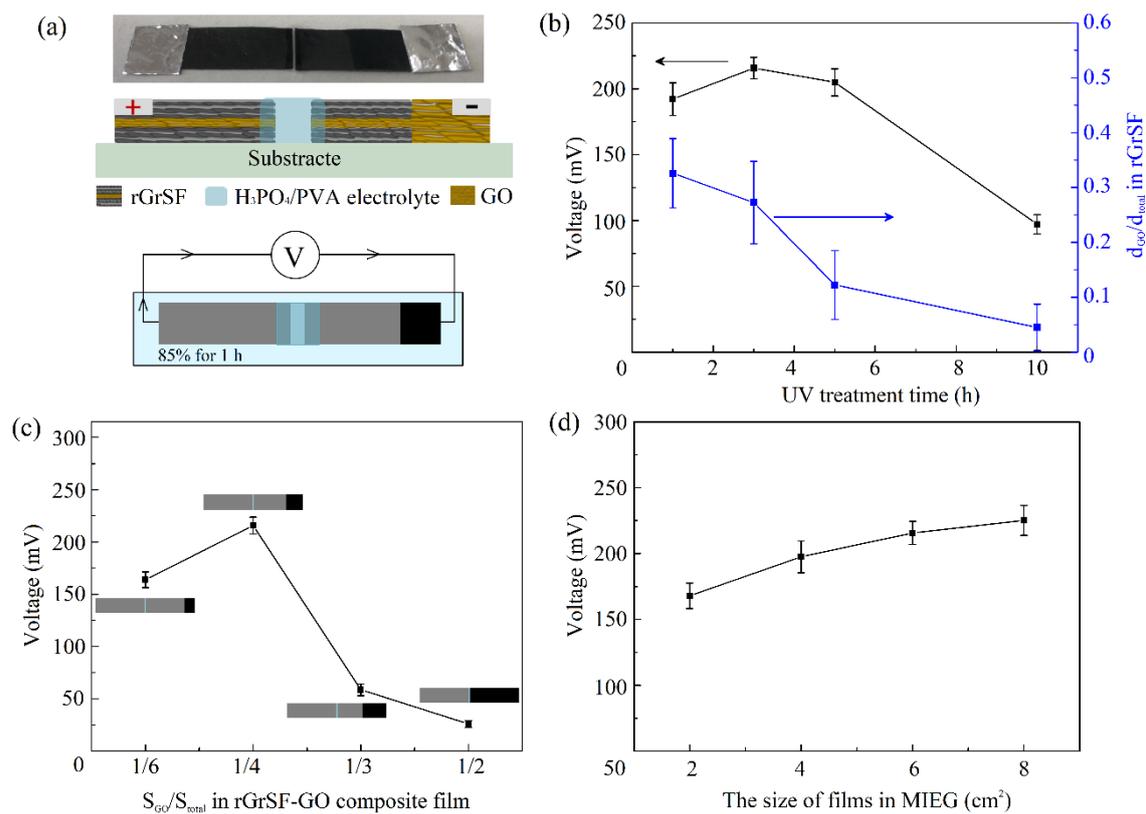
Figure 3-5 (a) Digital photograph, design schematic diagram and test method of V_{OC}. (b) The V_{OC} of MIEGs (85%, 1 h) and d_{GO}/d_{total} in different UV treatment times (c) The V_{OC} of MIEGs with different S_{GO}/S_{total}. (d) The V_{OC} of MIEGs (85%, 1 h) with different size.

3.3.4 The electricity generation mechanism of MIEG

To simulate the changes in potential of the RGRSF and the RGRSF–GO composite films in MIEG under moisture, wet air was approached on MIEG in a flow velocity of 10 mL/s (Figure 3-6a), and the V_{OC} versus time curves of RGRSF (V_1), RGRSF–GO composite films (V_2) and MIEG (V_3) were recorded in Figure 3-6b. V_1, V_2, and V_3 under wet air for 5 s, rapidly increased to 24 mV, 60 mV and 159 mV, respectively. The RGRSF–GO composite film generated larger voltage than RGRSF because much more

water molecules enter RGRSF–GO composite film and combined with GO to release more H^+ ions. Without the supply of wet air, V_1 slowly dropped in the following 23 s, While V_2 and V_3 rapidly decreased at the beginning then their decrease speeds became slow. The comparison of V_{oc} of RGRSF, RGRSF–GO composite films and MIEG suggests that a rapid discharging behavior might happen at the untreated GO part in the RGRSF–GO composite film and electrolyte gel.

Figure 3-6c–i show the charging and discharging mechanism of MIEG. Because of the significant difference in surface hydrophilicity between RGRSF and GO, moisture is more easily absorbed by untreated GO part in the RGRSF–GO composite film. GO will ionize and release lots of free H^+ ions after combining with water molecules (Figure 3-7c). The free H^+ ions will be driven by the concentration differences, [35] and they move with water molecules in the RGRSF–GO composite film (Figure 3-6c). The aggregation of free ions in the RGRSF–GO composite film and the water potential difference between the two films can increase the directional diffusion of H^+ ions in the electrolyte gel (Figure 3-6d). The potential difference in the gel can boost the movement of ions in RGRSF to realize the potential difference between the two electrodes (Figure 3-6e).
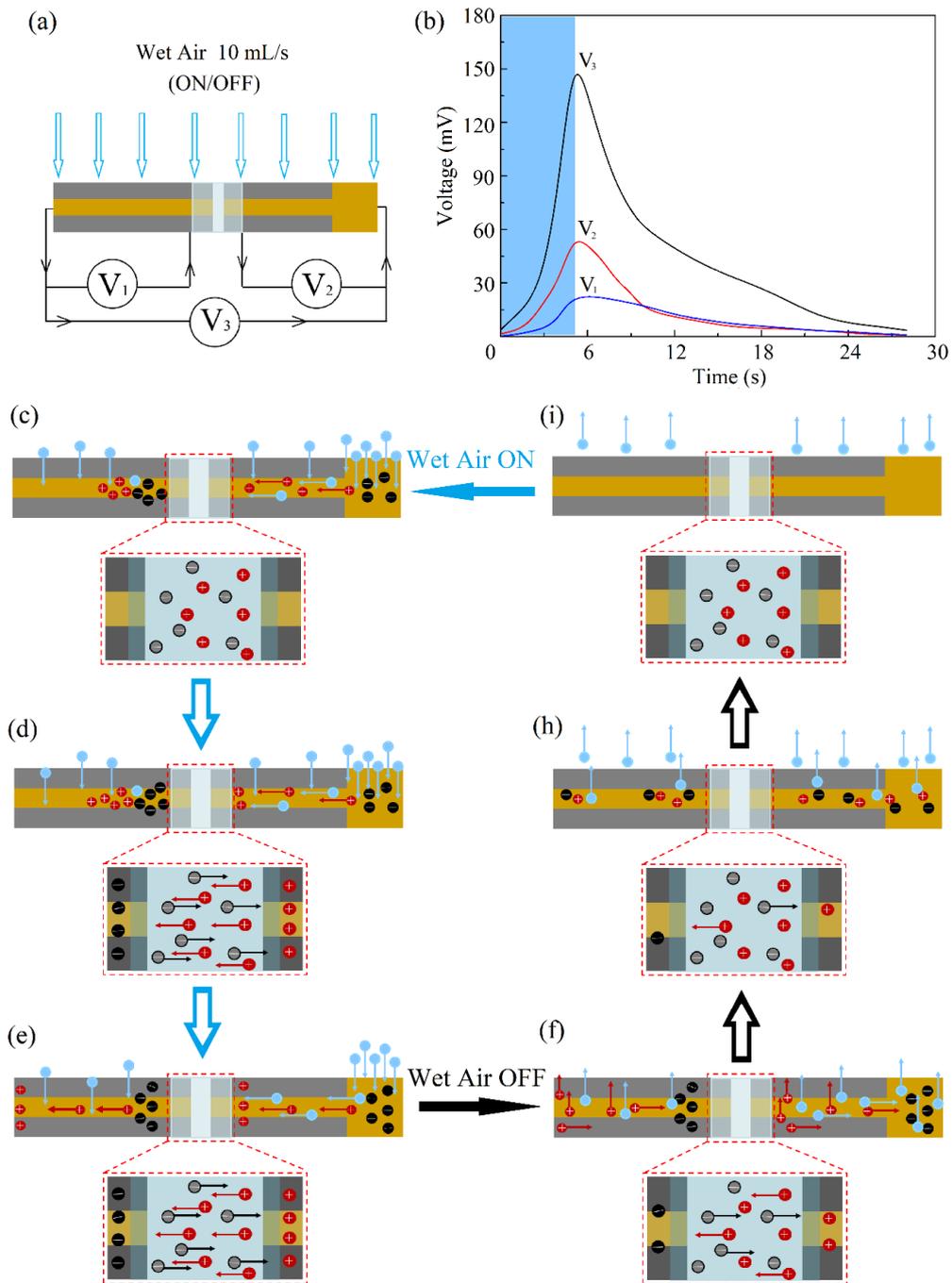
Figure 3-6 (a-f) The method to test the V_{OC} of RGRSF, RGRSF–GO composite films and MIEG under wet air ON and OFF. ON and OFF represent the start and stop of wet air supply, respectively. (b) The V_1 V_2 and V_3 variation curves under wet air ON and OFF. (c–i) The charging and discharging mechanism of MIEG.

Without moisture supply, dehumidification will happen in RGRSF and RGRSF–GO composite films. The H^+ ions in RGRSF move up the surface with the diffusion direction of water. While in RGRSF–GO composite film, part of ions moved up to the surface and others moved to untreated GO part with water molecules (Figure 3-6f). And in this process, the potential difference between electrolyte still exists. Afterwards, with the decrease of moisture in films, free H^+ ions decreased and recombined with the negative functional groups immobilized on GO (such as COO–) [24]. Since the tortuous path produced by the layered stacked structure of GO makes the penetration of water molecules in the layer spacing direction [42,43] more difficult than the transport between layers, dehumidification becomes difficult and free ions cannot quickly combine with the negative functional groups. In this process, the potential difference between two sides of electrolyte gel still exists to promote the directional movement of ions in electrolyte (Figure 3-6h). This is consistent with the result that the decrease of V_3 was delayed in Figure 3-6b. The discharge behavior stops with the completion of dehumidification (Figure 3-6i).

Combined with the movement of water and ions inside MIEG in the charging and discharging processes, from a comparation of the charge and discharge curves of V_1 and V_2 (Figure 3-6b), it can be indicated that untreated GO part in the RGRSF–GO composite film made it able to easily absorb moisture from outside，and thanks to the special sandwich structure

of RGO/GO/RGO, water molecules were difficultly exhausted from inside, which might endow MIEG a capacity to continuously supply power in a dry environment. Additionally, the short circuit current (I_{sc}) density of MIEG showed similar change trend as its Voc. I_{sc} density increased to 23.95 uA/cm^2 at the first 5 seconds (Figure 3-7).
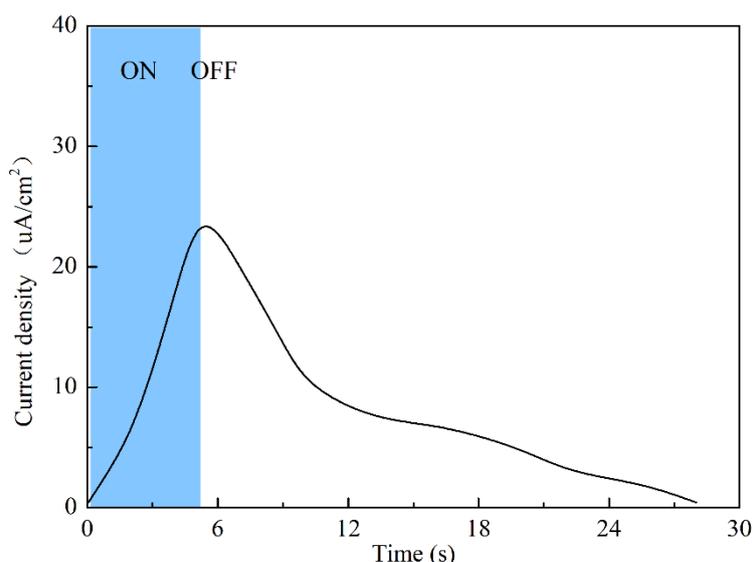
Figure 3-7. The current versus time curve when wet air is ON and OFF.

3.3.5 The output performance of MIEG under moisture

In Figure 3-8a, the change of V_{oc} under a humidity of 85% had three stages. In the first stage, the V_{oc} increased fast to 215.7 mV in 1 h, where the large water potential difference between GO and RGRSF in RGRSF-GO composite film promoted ions to move fast. In stage II, the difference became weak and their hygroscopicity began to reduce that the V_{oc} slowly increased from 1 h to 4 h. Afterwards, the V_{oc} decreased near to 1 mV in 10500 s in stage III. In this stage, the moisture absorption gradually came

to saturate, and H^+ ions diffused by concentration difference, which made the V_{OC} drop and even changed the direction of current at the last.
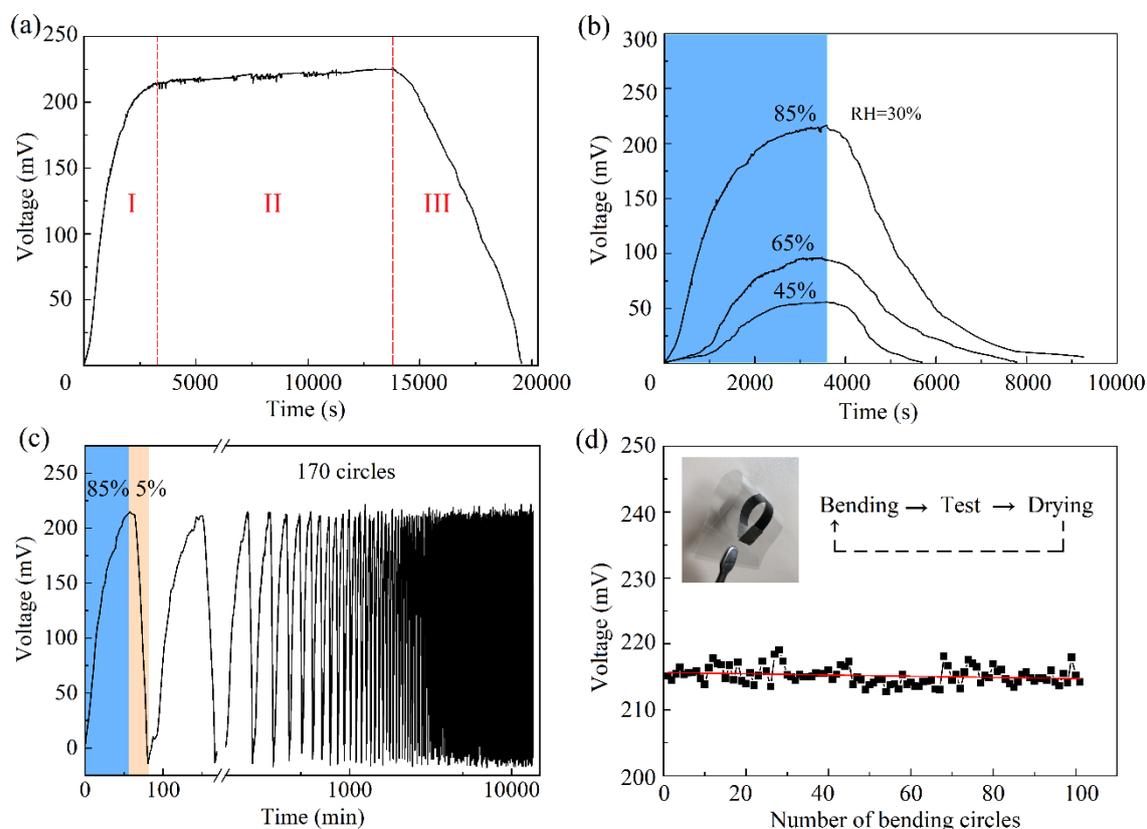
Figure 3-8 (a) V_{OC}–t of MIEG in a humidity of 85%. (b) V_{OC}–t curves of MIEG in different humidity. (c) 100 cycles of V_{OC} change of MIEG in a humidity of $\Delta H = 80\%$. (d) V_{OC} variation of MIEG in humidity of 85% for 1 h under 170 times bending, and the bending behavior is conducted like digital photo that the bending angle was about 150°.

In Figure 3-8b, the V_{OC} of MIEG under difference humidity differences (ΔH = 15%, 35%, and 55%) were recorded. MIEGs in humidity of 45%, 65%, and 85% could achieve 51.2, 74.6, 215.3 mV in 1 h. Their discharge processes kept 2100, 4200, and 6700 s under ΔH of 15%, 35%, and 55%,

respectively. In the dehumidification process, after the initial slow speed, the discharge speed increases, and then decreases. In addition, a small humidity difference led to a slow initial discharge speed. Notably, V_{OC} under ΔH of 55% decreased from 215 to 100 mV for 1600 s. This means that the induced electricity can be well stored in MIEG even under a great humidity difference and continue to provide considerable power in a dry environment. This is completely different from the electricity induced by moisture in GO [22, 23, 24] in which the V_{OC} disappears within a few seconds without moisture supply. To shorten the experiment time, the charging and discharging cycle of MIEG was conducted under ΔH of 80%. From Figure 3-8c, the output signal presented insignificant performance attenuation after 170 repetitions, suggesting high stability and reproducibility. Further, MIEG also presented outstanding flexibility that it kept working efficiently and stably after the generator being bent 100 times with bending angle of about 150° (Figure 3-8d).
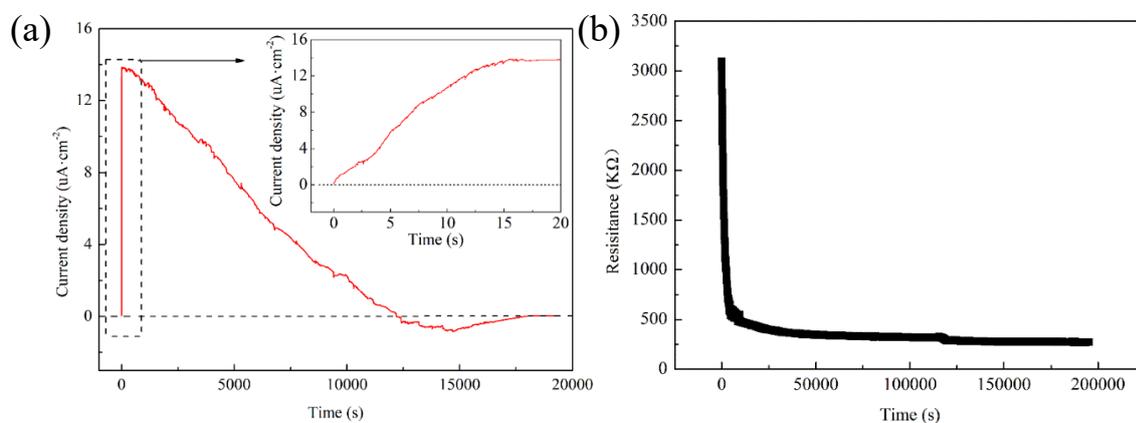

Figure 3-9 (a) The I_{sc} density–t curve of MIEG under a humidity of 85%, (b) the resistance–t curve of MIEG under a humidity of 85%.

Besides, the short-circuit current (I_{sc}) density quickly increased to 13.78 uA/cm^2 in seconds (Figure 3-9 a). The directional motion of free H^+ ions were driven by the concentration difference of H^+ ions between RGO/GO/RGO part and GO part in RGRSF. And the difference increased in seconds under moisture, which resulting in that the speed or number of directionally moved H^+ ions increased or both. So, the current increased fast in initially. Afterwards, the current slowly decreased, which was related to the diffusion of water molecular and the movement of H^+ ions, both mainly depended on their concentration differences. And the resistance of MIEG decreased to 77.4% fast in 1 h (Figure 3-9b) because of the increasing absorbed moisture. And after the first 1h, the moisture absorption ability decreased and gradually reached saturation, so the resistance changed little.

As it shown in Figure 3-10, changes in ambient temperature and humidity had a great impact on the power generation capacity of MIEG. A higher humidity helped to the increase speed of V_{OC} (Figure 3-10a). The great humidity led to the increase of moisture absorption rate, and meanwhile the movement of H^+ ions became faster, so that the faster the voltage increase. The temperature of moisture also improved the max value of V_{OC} because of the increase of the kinetic energy of water molecules.
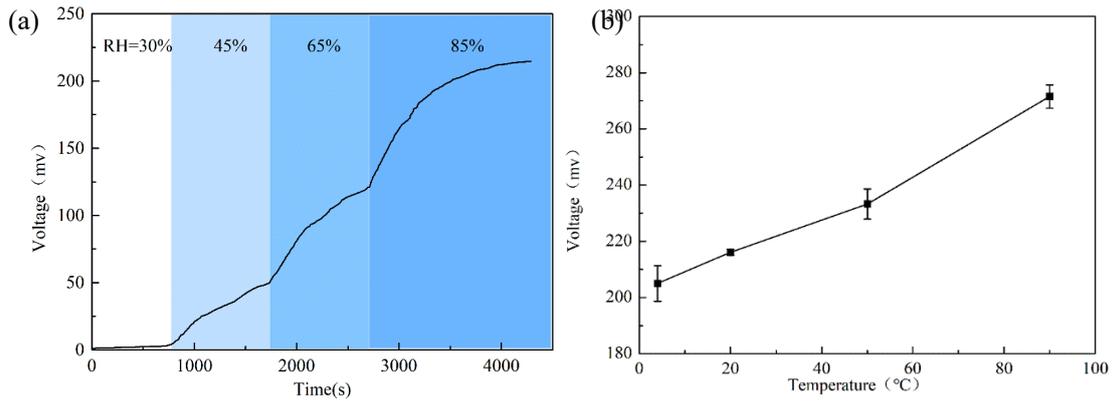
Figure 3-10 (a)The V_{OC}–t curve of MIEG when humidity is changed from 30% ~ 85% (b) the

V_{OC} of MIEG under 85% for 1h when moisture temperature is changed.

3.3.6 The extension and application of MIEGs

Since a single MIEG could not meet the power requirements for electronic devices, MIEGs should be connected in series and parallel to obtain higher voltage and current. From Figure 3-11a and 3-12b, five MIEGs connected in series and parallel could gain considerable V_{OC} of 1.13 V and I_{SC} density of 62.72 uA/cm², respectively, in 1 h. According to the formula, $P = \frac{V_{oc}I_{sc}}{4}$, the power density was calculated that a MIEG could gain power density of 0.73 uW/cm². And the extension of MIEG benefited to increasing of power density that 5MIEGs obtained 3.36 uW/cm². The Nine MIEGs (9MIEDs) were connected as the illustration shown in Figure 3-11c, and its V_{OC} and I_{SC} density versus time curves were recorded under ΔH of 55%. Nine MIEGs generated electricity of 1.1 V, 13.28 uA/cm² after being placed under humidity of 85% for 1 h to successfully power a commercial LED (Figure 3-11c). When transferred to the room environment with a humidity of 30%, the discharge behavior of 9MIEGs

took more than 5 h, in which the V_{OC} of 1.13–1.0 V kept about 4040 s and I_{SC} density decreasing from 13.28 to 10 uA/cm^2 approximately took 2580 s, suggesting excellent electricity supply endurance of MIEG in a dry condition.
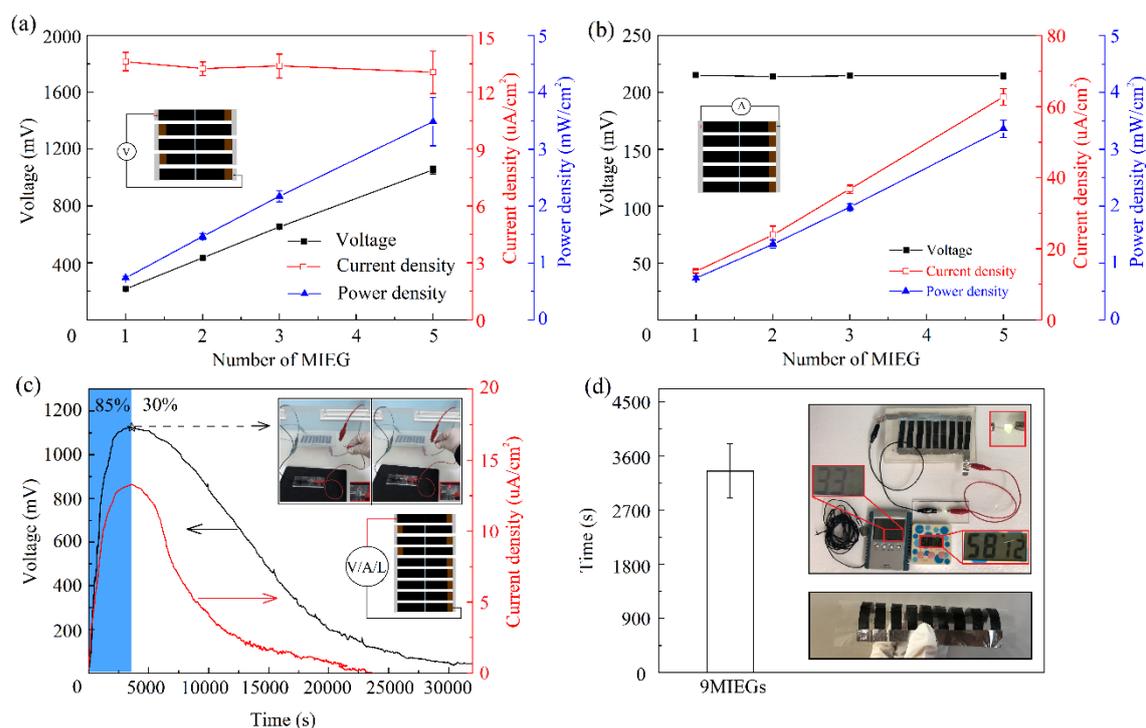
Figure 3-11 (a) V_{OC}, I_{SC} density and power density of MIEGs with series expansions. (b) V_{OC}, I_{SC} density and power density of MIEGs with parallel expansions. (c) V_{OC}–t and I_{SC} density–t of 9MIEGs under $\Delta H=55\%$. (d) The time that 9MIEGs (85%, 1 h) continues to light up the SMD LED under a room humidity of 30%.

As Figure 3-12 showed, the 9MIEDs kept powering a SMD LED for about 1 h under room humidity of 30%, which demonstrates that MIEG has good adaptability to humidity changes in application of sustainable

84

power supply for wearable electronics.
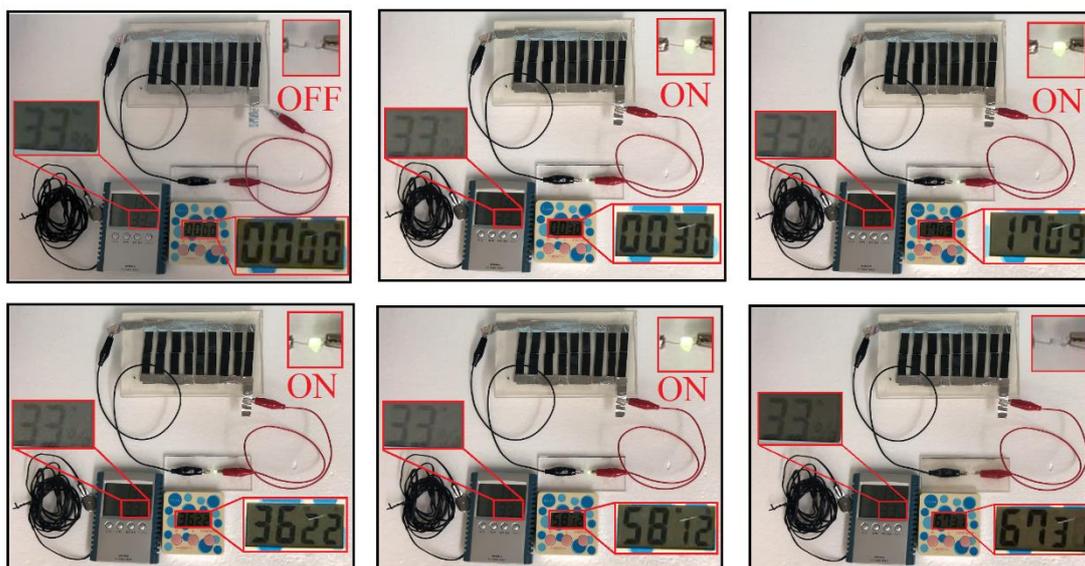
Figure 3-12. The images of that 9MIEGs (85%, 1 h) continues to light up the SMD LED under

a room humidity of 30%.

3.4 Conclusions

In this chapter, RGRSF and RGRSF–GO composite films were

developed by a simple bilateral UV treatment on GO films. Without any

additives, power generation from the moisture mechanism of MIEG mainly

depends on the hydrophilicity difference between the two films. The

special sandwich structure endows MIEG with the capability to generate

sustained electricity under moisture for more than 5.5 h and slow discharge

in a dry condition. The high stability and reproducibility of MIEG were

demonstrated by 100 cycles repetition of charge and discharge experiments.

Besides, the generator could be easily scaled up for higher output. 9MIEGs successfully powered a LED under moisture and kept it lit for 1 h in a normal room condition, thereby showing excellent adaptability to humidity changes in the application for wearable electronic products. Besides, the MIEG has many benefits of flexibility, high stability, reusability, lightweight, low price of medicines, and ease of production. The further research will focus on reducing energy consumption due to inner resistance and increasing its response sensitivity to low humidity.

References

[1] Zhang KW, Wang ZL, Yang Y. Conductive fabric-based stretchable hybridized nanogenerator for scavenging biomechanical energy. ACS Nano 2016;10(4): 4728-4734.

[2] Hou CT, Yang Y, Lin ZH, Ding Y, Park C, Ken CP, Chen LJ, Wang ZL. Nanogenerator based on zinc blende Cadet micro/nanowires. Nano Energy 2013;3(2):387-393.

[3] Xie LJ, Chen XP, Wen Z, Yang YQ, Shi JH, Chen C, Peng MF, Liu YN, Sun XH. Spiral steel wire-based fiber-shaped stretchable and tailorable triboelectric nanogenerator for wearable power source and active gesture sensor. Nano-Micro Lett.2019;11:39.

[4] Must I, Johanson U, Kaasik F, Po˜ldsalu I, Punning A, Aabloo A. Charging a supercapacitor-like laminate with ambient moisture: from a humidity sensor to an energy harvester. Phys Chem 2013;15: 9605-9614.

[5] Král P, Shapiro M. Nanotube electron drag in flowing liquids. Physical Review Letter 2001; 86(01):101-104.

[6] Ghosh S, Sood AK, Kumar N. Carbon nanotube flow sensors, Science2003; 299(02):1042-1044.

[7] Persson BNJ, Tartaglino U, Tosatti E, Ueba H. Electronic friction, and liquid-flow-induced voltage in nanotubes. Physical Review 2004; 69:235410-235415.

[8] Lee S, Kim D, Kim S, Han CS. Flow-induced voltage generation in

high purity metallic and semiconducting carbon nanotubes. Applied Physic Letters 2011; 99: 104103.

[9] Zhao Y, Song L, Deng K, Liu Z, Zhang Z, et al. Individual water-filled single-walled carbon nanotubes as hydroelectric power converters. Advanced Material 2008; 20:1772–1776.

[10] Liu J, Dai L, Baur JW. Multiwalled carbon nanotubes for flow-induced voltage generation. Journal of Applied Physics 2007; 101:064312.

[11] Dhiman P, Koratkar N, Yavari F, Mi X, Gullapalli H, et al. Harvesting energy from water flow over graphene. Nano Letter 2011; 11:3123–3127.

[12] Lee SH, Jung Y, Kim S, Han CS. Flow-induced voltage generation in nonionic liquids over monolayer graphene. Applied Physics Letters 2013; 102:063116.

[13] Yin J, Li X, Yu J, Zhang Z, Zhou J, Guo W. Generating electricity by moving a droplet of ionic liquid along graphene. Nature Nanotechnology 2014; 56 (04):1-6.

[14] Aruna RK, Singha P, Biswasb G, Chandaa N, Chakraborty S. Energy generation from water flow over reduced graphene oxide surface in a paper-pencil device. Lab on a Chip 2016; 16:3589-3596.

[15] Huang W, Wang G, Gao F, Qiao Z, Wang G, et al. Power generation from water flowing through three-dimensional graphene foam. Nanoscale 2013; 06 (07):3921-3924.

[16] Li C, Tian Z, Liang L, Yin S, Shen PK. Electricity generation from

capillary-driven ionic solution flow in a three-dimensional graphene membrane. ACS Applied Material & Interfaces 2019; 11:4922−4929.

[17] Lee SH, Kang YBA, Jung W, Jung Y, Kim S, Noh HM, Flow-induced voltage generation over monolayer graphene in the presence of herringbone grooves. Nanoscale Research Letters 2013; 8:487.

[18] Yin J, Zhang Z, Li X, Zhou J, Guo W. Harvesting energy from water flow over graphene. Nano Letter 2012; 12:1736-1741.

[19] Liu K, Ding TP, Li J, Chen Q, Xue GB, et al. Thermal-electric nanogenerator based on the electrokinetic effect in porous carbon film. Adv Energy Mater 2018; 8:6.

[20] Zhao F, Cheng HH, Zhang ZP, Jiang L, Qu LT. Direct power generation from a graphene oxide film under moisture. Adv Mater2015; 27:4351-4357.

[21] Luo ZL, Liu CH, Fan SS. A moisture induced self-charging device for energy harvesting and storage. Nano Energy 2019; 60:371-376.

[22] Zhao F, Liang Y, Cheng HH, Jiang L, Qu LT. Highly efficient moisture-enabled electricity generation from graphene oxide frameworks. Energy Environ Sci 2016; 9(3):912-916.

[23] Liu K, Yang PH, Li S, Li J, Ding TP, et al. Induced potential in porous carbon films through water vapor absorption. Angewandte Chemie-International Edition 2016; 55(28):8003-8007.

[24] Xu T, Ding XT, Shao CX, Song L, Lin TY, et al. Electric power

generation through the direct interaction of pristine graphene-oxide with water molecules. Small 2018;14.

[25] Marcano DC, Kosynkin DV, Berlin JM, Sinitskii A, Sun ZZ, et al. Improved synthesis of graphene oxide. ACS Nano 2010; 4(8): 4806-4814.

[26] Han DD, Zhang YL, Liu Y, Liu YQ, Jiang HB, et al. Bioinspired graphene actuators prepared by unilateral UV irradiation of graphene oxide papers. Adv. Funct. Mater 2015; 06:4548-4557.

[27] Fu XY, Wang LL, Zhao LJ, Yuan ZY, Zhang YP, Wang DY, Wang DP, Li JZ, Li DD, Shulga V, Shen GZ, Han W. Controlled assembly of MXene nanosheets as an electrode and active layer for high-performance electronic skin. Advanced Material Technology 2021; FEB.

[28] Kumar P, Subrahmanyam K, Rao C. Graphene produced by radiation-induced reduction of graphene oxide. International Journal of Nanoscience 2010; 09:559-566.

[29] Kumar P, Das B, Chitara B, Subrahmanyam K, Gopalakrishnan K, et al. Novel radiation-induced properties of graphene and related materials. Macromolecular Chemistry and Physics 2012; 6:1146-1163.

[30] Tai XH, Chook SW, Lai CW, Lee KM, T.C.K, et al. Effective photoreduction of graphene oxide for photodegradation of volatile organic compounds. RSC Adv 2019; 9:18076-18086.

[31] Williams G, Seger B, Kamat PV. TiO_2-graphene nanocomposites UV-assisted photocatalytic reduction of graphene oxide. ACS Nano 2008;

7:1487-1491.

[32] Smirnov VA, Arbuzov AA, Shul'ga YM, Baskakov SA, Martynenko VM, et al. Photoreduction of graphite oxide. High Energy Chem 2011; 45(1):57-61.

[33] Zhang YL, Guo L, Wei S, He YY, Xia H, et al. Direct imprinting of microcircuits on graphene oxides film by femtosecond laser reduction. Nano Today 2010; 5(1):15-20.

[34] Amer AA, Reda SM, Mousa MA, Mohamed MM. Mn_3O_4/graphene nanocomposites: outstanding performances as highly efficient photocatalysts and microwave absorbers. RSC Adv 2017;7(2):826-839.

[35] Diez N, Sliwak A, Gryglewicz S, Grzyb B, Gryglewicz G. Enhanced reduction of graphene oxide by high-pressure hydrothermal treatment. RSC Adv 2015; 5(100):81831-81837.

[36] Zhao LJ, Wang K, Wei W, Wang LL, Han W. High-performance flexible sensing devices based on polyaniline/MXene nanocomposites. InfoMat 2019; 11:407-416.

[37] Stankovich S, Dikin DA, Piner RD, Kohlhaas KA, Kleinhammes A, et al. Synthesis of graphene-based nanosheets via chemical reduction of exfoliated graphite oxide. Carbon 2007; 45(7): 1558-1565.

[38] Amieva EJC, Fuentes-Ramirez R, Martinez-Hernandez AL, Millan-Chiu B, et al. Graphene oxide and reduced graphene oxide modification with polypeptide chains from chicken feather keratin. J Alloy Compd 2015;

643: S137-S143.

[39] Liu CC, Ju J, Zheng YM, Jiang L. Asymmetric ratchet effect for directional transport of fog drops on static and dynamic butterfly wings. ACS Nano 2014; 8(2):1321-1329.

[40] Zhang YL, Guo L, Xia H, Chen QD, Feng J, Sun HB. Photoreduction of graphene oxides: methods, properties, and applications. Advanced Optical Materials 2014; 2(1):10-28.

[41] Zarrin, H, Higgins, D, Jun, Y, Chen, ZW, Fowler M. Functionalized graphene oxide nanocomposite membrane for low humidity and high temperature proton exchange membrane fuel cells. Journal of Physical Chemistry C 2011; 10:20774-20781.

[42] Sui X, Ding H, Yuan Z, Leong CF, Goh K. The roles of metal-organic frameworks in modulating water permeability of graphene oxide-based carbon membranes. Carbon 2019; 148(6):277-289.

[43] Zhang WH, Yin MJ, Zhao Q, Jin CG, Wang NX, Ji SL, Ritt CL, Elimelech M, An QF. Graphene oxide membranes with stable porous structure for ultrafast water transport. Nature nanotechnology 2021; JAN.

Chapter 4：A sustainable breath moisture-induced electricity generator based on sandwich structural CNT/GO composite film

4.1 Introduction

Water as a renewable and environmentally friendly energy source has been attracting considerable attention [1]. The traditional power generation mechanism is based on macroscopic water source activities (such as ocean tide, river, and rain) [2-5], heavily relying on the geographical environment and seasonal weather. The rapid development of nanotechnology has facilitated the application of the movements of water molecules in the environment and organisms to generate electricity. Various water forms, such as water droplets [4, 6-8], steam [9-11], and water molecules diffusion [12, 13], have been booming in clean energy harvest, showing a good promise in power supply for small electronics [14, 15]. However, the moisture from breath, an inexhaustible bioenergy source, has not been focused on as an energy source. Most researchers have mainly focused on the electricity generated from environmental moisture for power supply, and only a few of them have slightly mentioned that their generators could get energy from breathing moisture [14-23]. For example, Qu et al. have been working on the development of environmental moisture-induced generators [17, 24-30] and have made good contributions to this field. Only

one of their studies casually mentioned that a type of polymer moist-electric generator could achieve an open-circuit voltage (V_{OC}) of 70 mV under breath [16]. Zhou et al. have developed a titanium dioxide nanowire network humidity generator with a voltage pulse of 0.25 V under moisture from the mouth, and six cells in a series are used to power a light-emitting diode (LED) [31]. While the moisture supply from the breath is limited, the generator discharges fast after exhalation and cannot be applied for a sustainable-power supply. Hence, the development of a new sustainable breath-moisture-induced electricity generator (BMIEG) is urgently required.

In chapter 3, we have developed a sustainable environmental moisture-induced power generator. However, it can only generate about 50 mV under 45%. And the charging time took about 50 mins which is too slow. So, the sensitivity to low moisture of the generator should be improved if I want to use RGRSF into develop a breath-moisture induced power generator. In this chapter, I first develop a sustainable BMIEG during discontinuous exhalation to supply power to wearable electronics. This generator is fabricated using two graphene oxide (GO)/carbon nanotube (CNT)-based asymmetric composite films with a regional GO/reduced GO/GO (GO/RGO/GO) sandwich structure. The ability of the GO/RGO/GO sandwich structure film (RGRSF) to quickly absorb moisture and slowly dehumidify has been verified in our previous research [32]. The

appropriate addition of CNT facilitates the establishment of a continuous CNT network channel and induces voltage when water flows through the surface of the CNTs [33, 34] to enhance the output performance. The BMIEG innovated in this work is soft, reusable, stable, and continuous power generatable under discontinuous exhalation, presenting certain application prospects in the power supply of wearable electronics. By size expansion and parallel capacitor connection, the power supply affords an intermittent and continuously lit LED for different power supply requirements.

4.2 Materials and methods

4.2.1 Material preparations

GO was prepared using natural graphite flakes (Alfa Aesar, 7–10 μm) based on the Improved Hummer Method [35]. First, 0.24 g of GO and CNT (40–70 nm, Wako, Japan) were dispersed into 30 mL of distilled water by ultrasonic treatment for 1 h. The liquid mixture was dried under vacuum at 60°C for 3 h in a glass dish with a diameter of 9 cm to obtain a GO/CNT composite film (GCCF). The weight ratio of the CNT to GO was 1/10, 1/5, and 1/3. A high-pressure UV lamp with a power of 100 W and wavelength of 365 nm (Portable Cure 100, HLR100T-2, Sen Lights Corp., JAP., 170 mW·cm^{-2}) was used for GO surface reduction. As shown in Figure 4-1, an RGO/GO/RGO–CNT (RGRC) sandwich film (RGRCSF, 30 mm × 10

mm×60 um) was achieved by regional UV radiation treatment on the two sides of the GO film for 1 h, and the light barrier were used as the shield. The treatment part was the RGRC part, and the shielding part was the GC part, as shown in Figure 4-1. The proportion of the GO part in the total RGRC-GCCF was 1/2. Further, RGRCSFs with different CNT contents were labeled RGRC-GCCF-1/10, RGRC-GCCF-1/5, and RGRC-GCCF-1/3.

Polyvinyl alcohol (PVA, 1 g, polymerization degree: 900–1100, 96.0 mol%, Wako, Japan) was dissolved in 10 mL of distilled water at 90°C for 2 h at a stirring speed of 300 rpm. H_3PO_4 (1 g, 85%, Wako, Japan) was slowly added into the PVA solution at room temperature.

4.2.2 Fabrication of the BMIEG

The BMIEG was fabricated by bridging two pieces of RGRCSF end to end using the H_3PO_4/PVA gel (10 × 10 mm) in a bridging distance of 1 mm (Figure 4-1). Afterward, the BMIEG was dried at 30°C for 3 h, and the BMIEG was fixed on a transparent flexible plastic film with conductive tape 808 (TERAOKA, Japan).
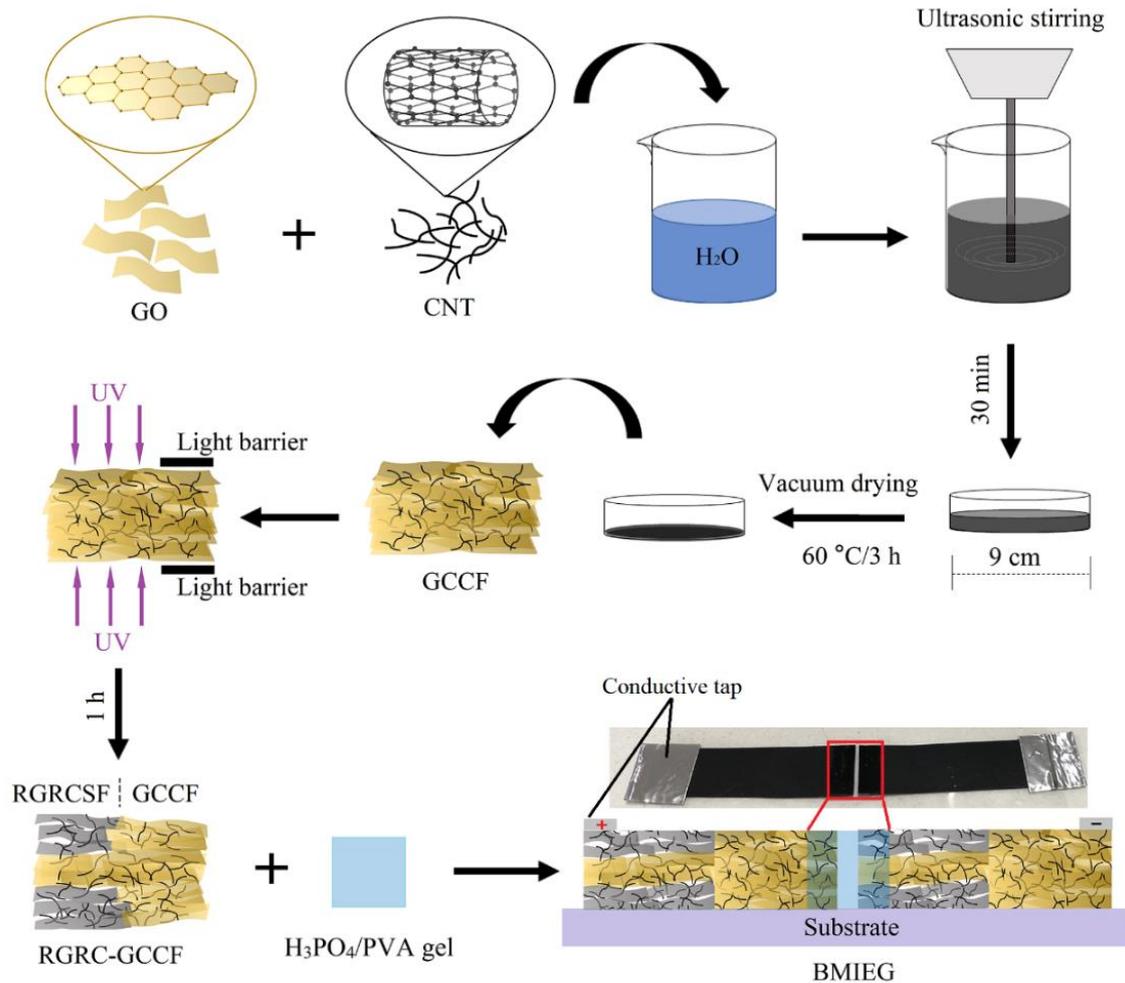
Figure 4-1 The schematic diagram of the BMIEG production process

4.2.3 Characters and evaluations

A scanning electron microscope (SU1510, Hitachi High Technologies, Japan) was used to characterize the surface and cross-section micromorphology of the films. Further, the element composition was evaluated by X-ray photoelectron spectroscopy (XPS, AXIS-ULTRA DLD, KRATOS, Japan). The surface hydrophilicity was measured by contact angle (CA) measurements (Digidrop, GBX, Whitestone Way, France, 65%,

25°C). The V_{OC}, I_{SC}, and resistance of the BMIEG were recorded using a digital multimeter (GDM-8342) at a temperature of 20°C ± 2°C and humidity of 50% ± 2%. All tests in this work were conducted in at least three places to represent each sample.

4.3 Results and Discussions

4.3.1 The Innovation of BMIEG

Since the moisture cannot be continuously supplied during breathing, it is difficult to continually harvest energy from breathing moisture. In our previous research, we developed a moisture-induced generator that could continuously discharge slowly for approximately 3 h even when transferred from a humid condition to a dry environment [32]. This kind of slow discharge mainly relies on the special RGO/GO/RGO sandwich structure composite GO film that can prevent moisture from escaping rapidly from the film in a dehumidification process. Applying this special structure in the breathing moisture-induced generator may be a good method to handle the problem of the intermittent supply of moisture in breathing. Therefore, the generator in our previous research was considered as a design choice (Figure 4-2a). Because of the limited moisture content in a single breath and the short breathing interval, the area of the GO part in the film should be enlarged; thus, a second-generation BMIEG was designed (Figure 4-2b), and 1/2 was the appropriate size of the GO part in the total film (Figure 4-

3). Due to that an electrical single can be induced by the moisture flowing over and inside CNTs[34, 36], coupled with the advantages of its hollow tubular structure benefiting to water molecule transport[37] and its chemical stability, CNTs could be added to enhance the electricity of the generator. Since the electricity induced by moisture moved on CNT was along the direction of the flow, the directions of the movement of water molecules and H^+ ions in the generator should also be consistent (Figure 4-3). So, the third generation of breathable moisture power generator was formed by bridging two identical RGRC-GCCF heads and tails (Figure 4-1). This bridging method not only simplified the preparation process but also allowed the generator to be continuously and infinitely expanded (Figure 4-2d).
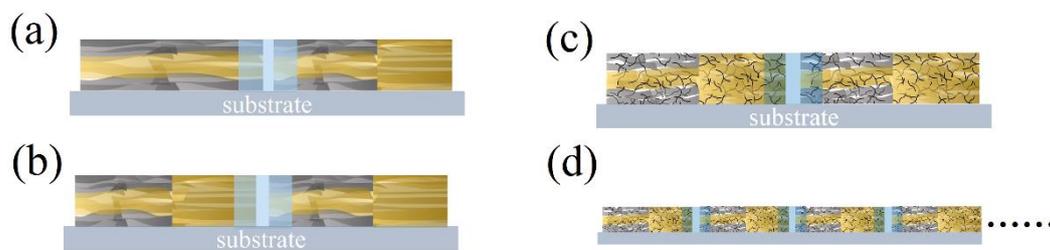

Figure 4-2 The BMIEG's design process (a) the first-generation generator: RGRSF/Electrolyte gel/RGR-GOCF (b) the second-generation generator: RGR-GOCF /Electrolyte gel/RGR-GOCF (c) the third-generation generator (BMIEG): RGRC-GCCF /Electrolyte gel/RGRC-GCCF (d) the continuous and infinite expansion of BMIEG
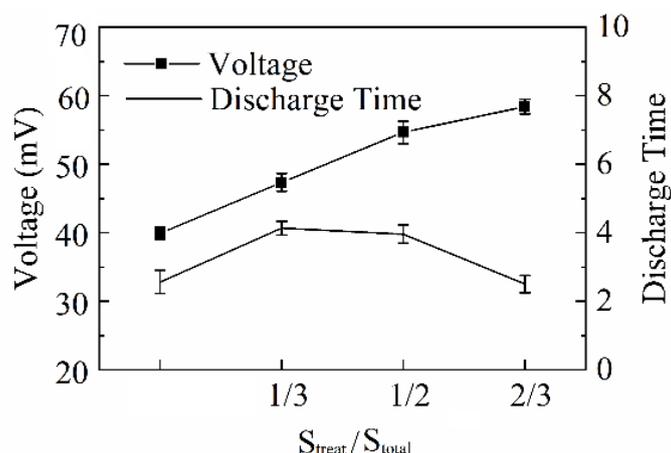
Figure 4-3 The effect of S_{treat}/S_{total} on the V_{OC} of BMIEG under an exhalation

4.3.1.1 The Characters of the regional UV-treated RGRC-GCCF

It has been verified in our previous study that the RGO/GO/RGO sandwich structural film can be obtained by regional UV treatment [32]. The treated part in the RGRC-GCCF was the RGRCSF. Figure 4-4a shows the surface and cross-sectional electron micrographs of the film before and after the UV irradiation treatment. After the treatment, some RGO sheets on the surface of the RGRCSF part were discontinuously stacked, and the CNTs wrapped in the GO layers were exposed on the surface. This was because of the carbon emission during the UV treatment; the CNTs on the surface were pushed outward, and the compact surface structure was destroyed. In the cross-sectional morphologies shown in Figure 4-4a, the GO sheets in the GCCF part were tightly stacked, and the CNTs were uniformly distributed in the thickness direction. Because of the limit of the UV penetration and carbon emission in the surface layers [38, 39], the interlayer spacing on the two sides of the RGRCSF increased and presented

100

a sandwich cross-section structure. Figure 4-4b shows the CA of the film before and after UV irradiation treatment. The GO film exhibited good hydrophilicity with a small CA of 38.24°. The CA of the GCCF increased to 52.3° because of the addition of little CNT, while its surface hydrophilicity was not bad. The significant decrease in the surface hydrophilicity of the RGRCSF was due to the reduction in the UV treatment and the exposure of the CNT on the surface. These can be verified by the chemical composition analysis of the film surface.
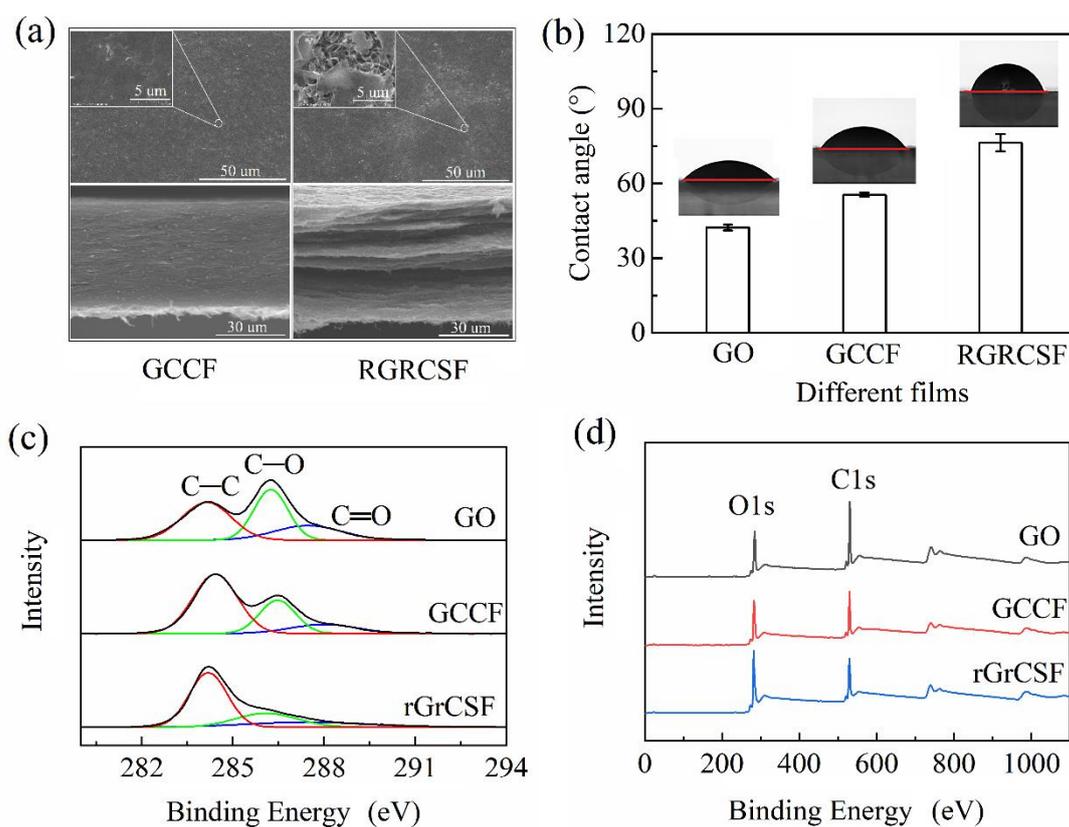

Figure 4-4(a) The surface and cross-section microscopic morphologies, (b) surface hydrophilicity and (c, d) surface chemical composition of the GCCF part and the GRGCSF part in the RGRC-GCCF.

The C1s spectra and survey XPS spectra of the GO film, GCCF, and RGRCSF were obtained and are shown in Figures 4-4c and 4-4d. As shown in Figure 4-4c, the C1s spectrum obtained three characteristic peaks: C–C at 284.2 eV, C–O at 266.3 eV, and C=O at 288 eV [40]. Compared with that of the GO film, the C–C bond of the GCCF significantly increased because of the addition of CNTs. Since the organic carbon was removed by photoreduction during the UV irradiation treatment, the C–O and C=O peaks of the RGRCSF became weak, while the intensity of the C–C peak increased [32, 38, 40, 41]. Further, the exposure of the CNT on the surface might enhance the intensity of the C–C peak. As shown in Figure 4-4d, the intensity of the O1s peak (525–545 eV) of the RGRCSF decreased, and the C1s peak (280–300 eV) became stronger. In summary, the GCF and RGRCSF had significant hydrophilicity differences that would be beneficial to achieve the asymmetric hydrophilicity of the RGRC-GCCF. Further, the sandwich structure would facilitate the transportation of water molecules in the RGRCSF.
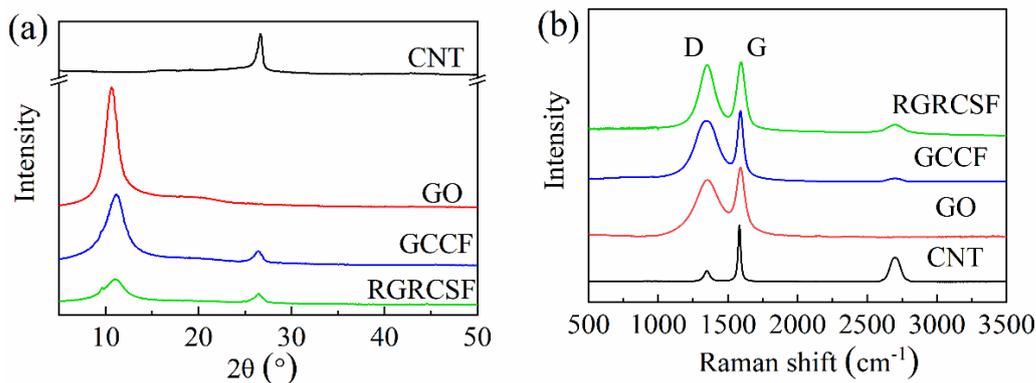
Figure 4-5 The XRD (a) and Raman (b) of the GCCF part and the GRGCSF part in the RGRC-GCCF

The XRD and Raman of the Regional UV-Treated RGRC-GCCF were studied in Figure 4-5. In Figure 4-5a, GO, GCCF and RGRCSF films, all have a typical peak at $2\theta = 11.5°$, which is the crystal face (001) of the characteristic peak for exfoliated GO[32, 42], Comparing with GCCF and RGRCSF films, the peak became weaker after treatment owing to the interlayer peeling and increase of disorder[38, 40]. Besides, GCCF and RGRCSF films also has a peak of CNT at $2\theta = 26°$ which is attributed to the crystal face (002) reflection of the hexagonal graphite structure [43, 44]. In Figure 4-5b, GO, GCCF and RGRCSF films have two characteristic peaks D-band at 1340 cm^{-1} and G-band at 1580 cm^{-1}. The D and G bands represent the breathing modes of rings with activation by defects and the in-plane bond stretching motion of sp2 C–C bond [45]. The D-band of GCCF is stronger than that of RGRCSF films because of reduction effect of UV irradiation. GCCF and RGRCSF films also have an obvious peak at

2700 cm^{-1} which was 2D-band, one typical peak of CNT.

4. 3.1.2 The electricity-enhanced RGRC-GCCF

The asymmetrically hydrophilic RGRC-GCCF was obtained by regional UV treatment, and one part was RGRCSF and the other was GCCF (Figure 4-6a). The V_{OC} of the RGRC-GCCF was tested under exhalations from the mouth of the tester. The surface micromorphology of the RGRCSF with different CNT contents is presented in Figure 4-6b. The increased surface wrinkles (Figure 4-6b) were due to the addition of CNT. Among the three films containing CNT (RGRCSF-1/10, RGRCSF-1/5, and RGRCSF-1/3), the RGRCSF-1/3 showed obvious agglomeration. Considering the disbenefit of the CNT on the surface hydrophilicity, the content of the CNT in the RGRCSF was controlled to be less than 1/3. Theoretically, the appropriate addition of CNT to form 3D CNT nano webwork in the film can increase electricity because a voltage/current can be induced when water flows through the CNTs (Figure 4-6h). However, the addition of CNT brings a negative influence on the surface hydrophilicity of the film. Thus, the appropriate content of CNT needs to be discussed further. As shown in Figures 6d–f, the RGRSF without CNT could generate 7.46 mV (Figure 4-6c), and the voltages of the RGRC-GCCF with CNT of 1/10, 1/5, and 1/3 were 11.23 mV (Figure 4-6d), 7.13 mV (Figure 4-6e), and 5.86 mV (Figure 4-6f), respectively.

Figures 4-6g and 4-6h show the power generation principle of the

RGRC-GCCF. The surface hydrophilicity difference afforded a regional difference in the ability of the RGRC and GC parts to absorb moisture. Since GO combined with water molecules can release free H^+ ions [17, 43], the difference in the water molecule concentration resulted in the difference in H^+ ions concentration, causing the H^+ ions to move directionally with the water molecules [15, 32, 46] (Figure 4-6g). Furthermore, it has been verified that the local electricity can be induced when water molecules move on the CNT (Figure 4-6h) [33, 34, 36, 37]. The network connection of CNTs (Figure 4-6b and 4-6g) could help to connect the local induced electricity to enhance the whole, as inferred from the comparison of Figures 4-6c and 4-6d.

To prove that the electrical signal comes from the device itself rather than the interference in the environment (such as vibration, breathing, etc.), three comparative experiments as Figure 4-7a~c shown. The voltage was tested without any sample by the digital multimeter in Figure 4-7a. And Figure 4-7b shows the voltage curve when the substrate (PET film) connected to the digital multimeter. In Figure 4-7c, the voltage change on the substrate was recorded under 10 exhalations. In Figure 4-7a and 7b, the voltage remained about 0 mV. And in Figure 4-7c, exhalation did bring irregular and small electrical signal changes. But comparing with the Figure 4-7d (same with Figure 4-6d), the influence is so small and can be ignored.
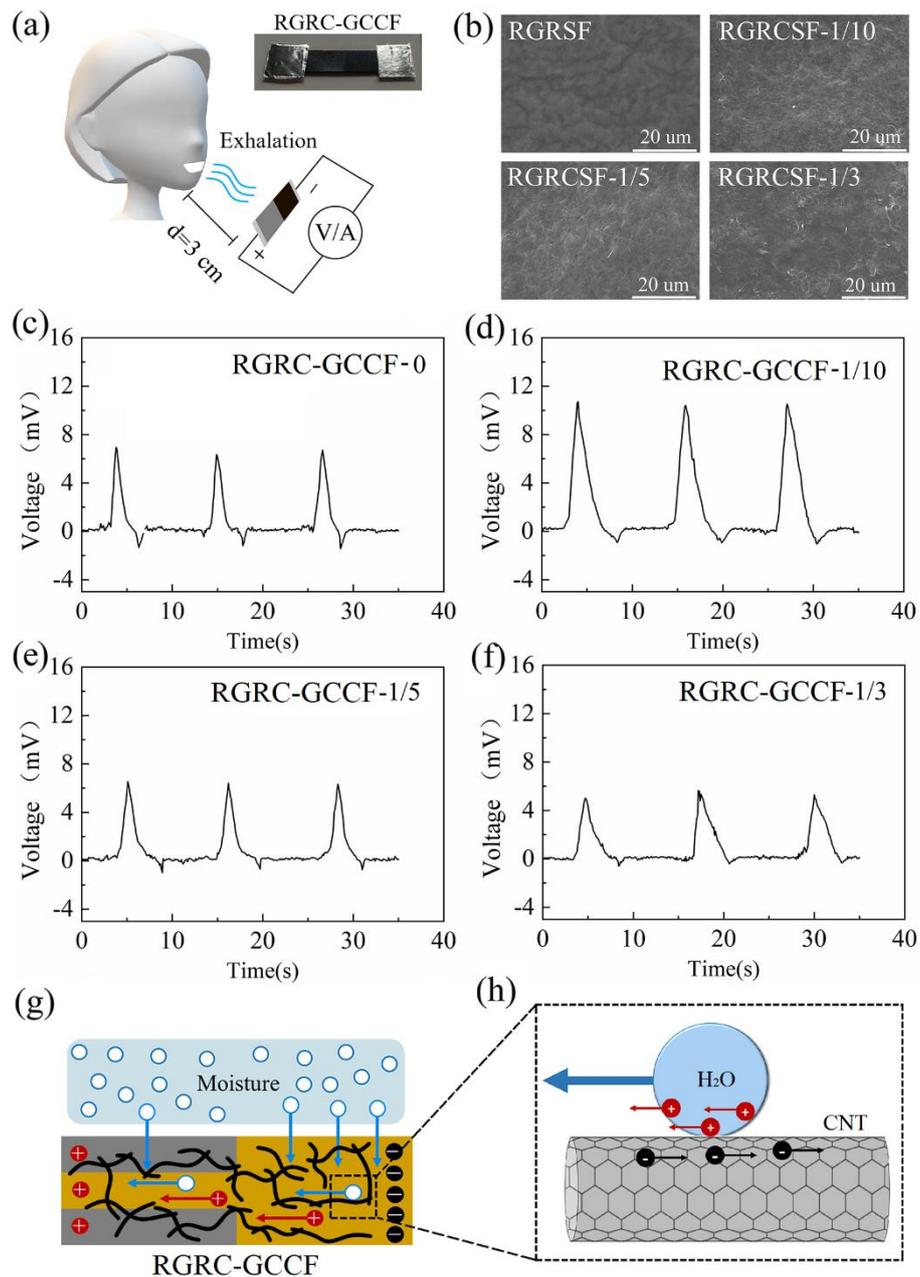
Figure 4-6(a) The V_{OC} measure method of the RGRC-GCCF under exhalations at 20°C and humidity of 50%; (b) the surface micromorphology of the RGRCSFs with different CNT contents of 0, 1/10, 1/5, and 1/3; (c–f) the V_{OC} change curves of the RGRC-GCCFs with different CNT contents under exhalations. The expiration frequency was 10 s, and each exhalation was maintained for 3 s. The S_{treat}/S_{total} of the RGRC-GCCFs was 1/2. (g, h) The electricity generation principle of the RGRC-GCCF under exhalation. The length of films above are 2 cm.

The V_{OC} of the RGRC-GCCF-1/10 was the largest because the surface hydrophilicity did not significantly increase as it shown in Figure 8a. This was because of the dominant station of the positive effect of the CNT on power generation. And the volume resistance of 1/5 reduced about 99% as Figure 8b showed. Consequently, the CNT content of 1/10 was considered as a proper choice.
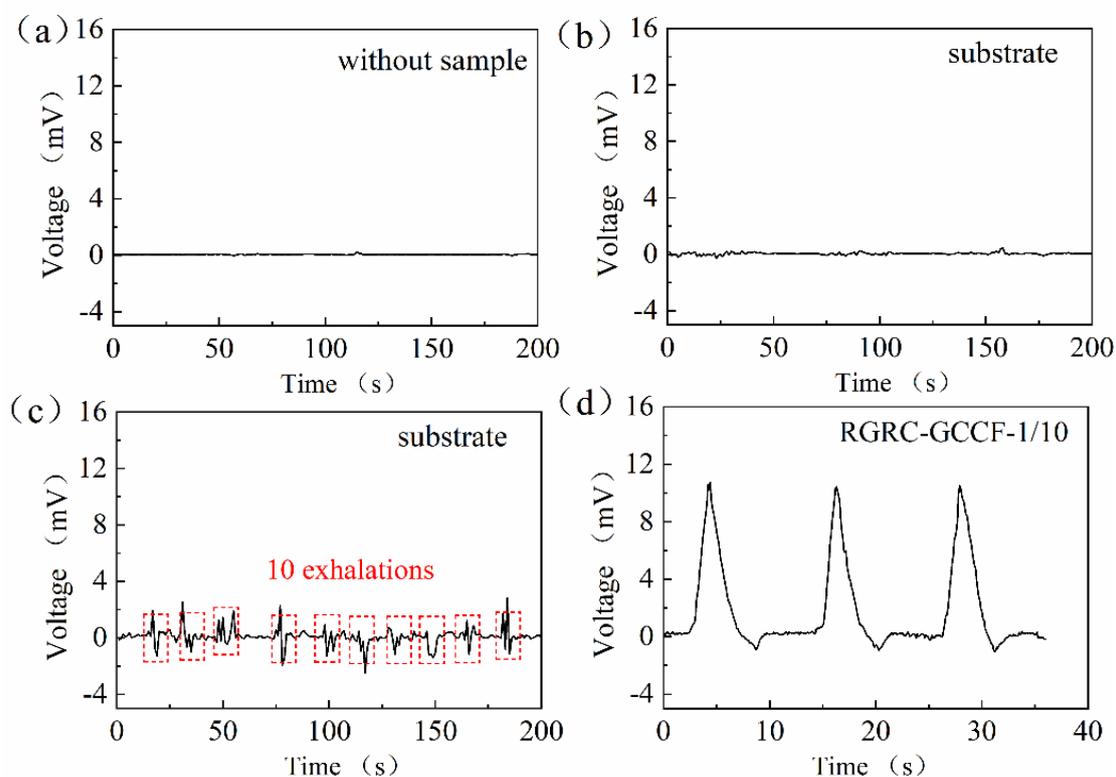

Figure 4-7 The V_{OC} change curves in RT of 20°C and RH of 50%, (a) without sample (b) substrate (c) substrate under interval exhalations and (d) RGRC-GCCF-1/10 under interval exhalations.
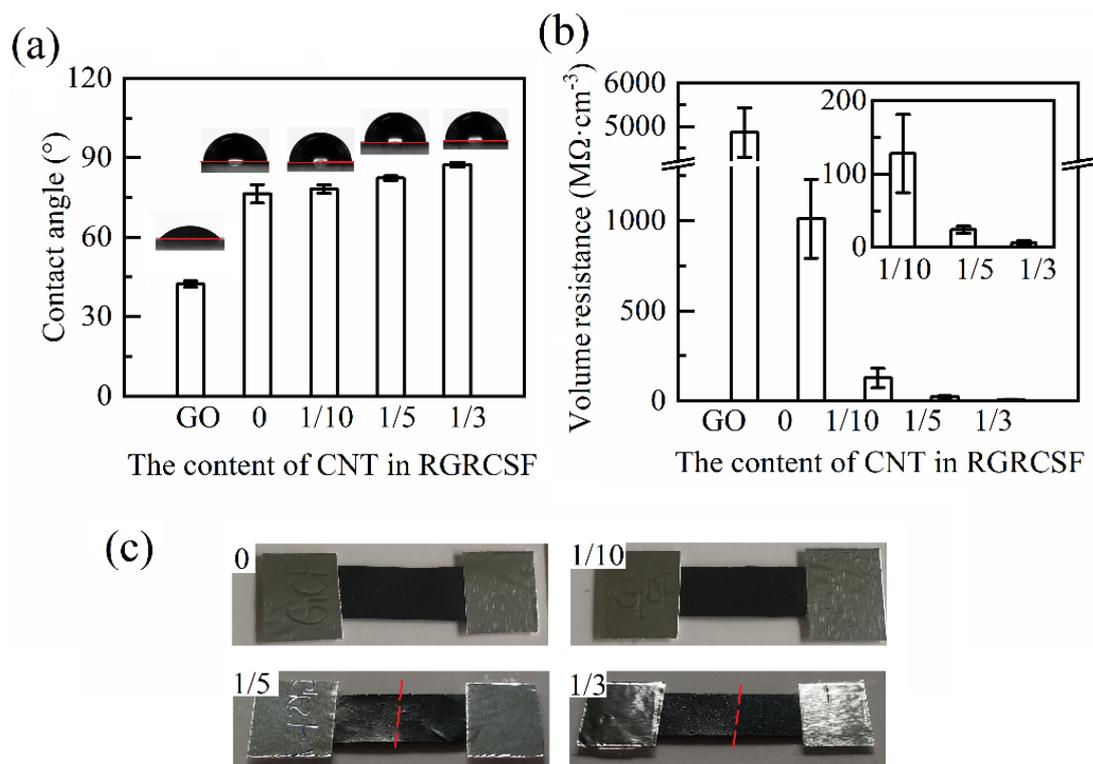
Figure 4-8 The surface hydrophilicity (a), the volume resistance (b) and the digital photos (c) of RGRCSFs with different CNT contents of 0, 1/10, 1/5, 1/3in RT of 20°C and RH of 50%.

4.3.2 The electricity generation mechanism of BMIEG

It was proved in Figure 4-6 that RGRC-GCCF could induce voltage under exhalation moisture, the electricity generation performance and mechanism of BMIEG need to be further studied. Figure 4-9 presents the electricity generation mechanism of the BMIEG and the V_{OC} change curves of difference parts of the BMIEG under exhalation.
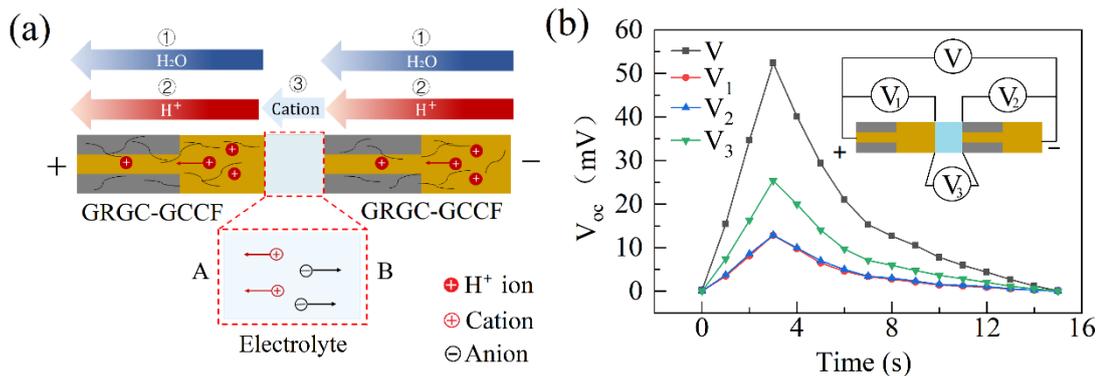
Figure 4-9 (a) The electricity generation mechanism of the BMIEG, (b) the V_{OC} change curves of difference parts of the BMIEG under exhalation of 3 s.

The BMIEG was fabricated by two pieces of RGRC-GCCFs and electrolyte gel. GO combined with water molecules can ionize free H^+ ions and anions fixed on functional groups[47, 48]. During an exhalation, a significant amount of water molecule was absorbed under exhalation. In this process, a humidity difference was formed because of the hydrophilicity difference in the RGRC-GCCFs. The directional movements of moisture and free H^+ ions happen simultaneously in the RGRC-GCCFs at the two ends of the electrolyte (①, ②). The A side nearby electrolyte is negatively, and the B side is positively because of the diffusion of H^+ ions. The potential difference between the A and B sides can drive ions in the electrolyte to move directionally (③). Consequently, a complete current path can be formed by ions' movement in the ② and ③ processes.

To prove the mechanism above, the V_{OC} changes of each part in BMIEG

under an exhalation were recorded in Figure 4-9b. The measure method is shown in Figure 4-10a. The V, V_1, V_2 and V_3 present the V_{OC} of the BMIEG, the RGRC-GCCFs in the two poles and the electrolyte, and they changed in similar trend. It is worth noting that V_1 and V_2 curves were almost overlap and their voltages values were about half of that of V_3, in which V_1, V_2 and V_3 showed peak values of 12.29 mV, 13.11 mV, and 25.11 mV respectively. This is consistent with the description of H^+ ions movements in RGRC-GCCFs (②) and electrolyte (③) in Figure 4-4a. After stopping exhalation, their discharge process lasted about 13 s, about 4 times of exhalation time (3 s). The slow discharge performance of BMIEG was mainly relied to the special sandwich structure [32] in RGRC-GCCF that water molecule in the RGRC part escape difficultly resulting from its poor surface hydrophily. So, its complete discharging behavior took much time.

4.3.3 The output performance of the BMIEG under controllable exhalation frequencies

As shown in Figure 4-10b, the V_{OC} of the BMIEG changed with breathing time. A sustainable exhalation time test was conducted on 15 adults and 5 children, and the shortest breath time was 3.27 s; therefore, the breath duration was selected as 3 s.
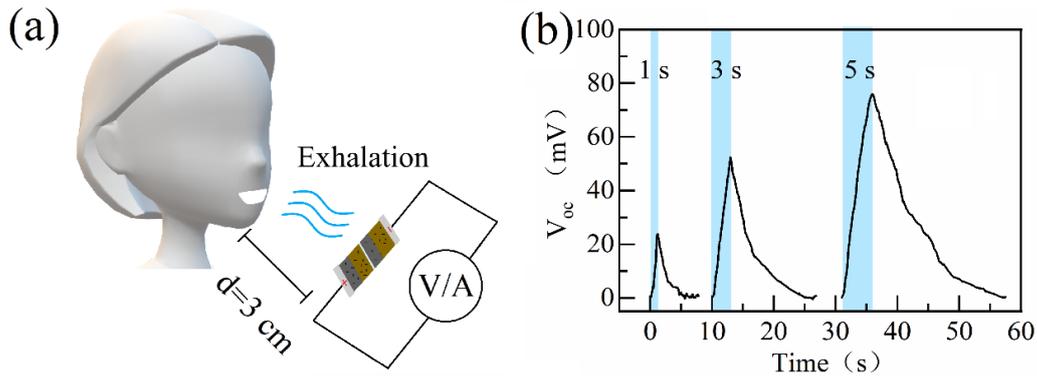
Figure 4-10 (a) The V_{OC} measure method of BMIEG under exhalations in RT of 20°C and RH of 50% , (b) the V_{OC} change curves under different exhalation times.

Figure 4-11a~d present the V_{OC} changes of the BMIEG under different exhalation frequencies. As shown in Figure 4-11a, the max V_{OC} of 50.56 mV was obtained in the first exhalation of breath and decreased to zero within 15 s; this was due to the sufficient dehumidification in the RGRC-GCCF, which led to a completive discharging behavior. The V_{OC} changed similarly in the subsequent exhalations. The V_{OC} curve that changed with a similar amplitude value was named the steady-state V_{OC}. As shown in Figure 4-5b, the V_{OC} of 52.37 mV obtained in the first exhalation dropped to 7.97 mV in 10 s. In the second exhalation, it generated a relatively high value of 64.71 mV because of the previous incomplete discharge. Additionally, the amplitude of the steady-state V_{OC} gradually increased to 19.83–81.59 mV in the initial five cycles (Figure 4-11b). After that, the V_{OC} varied similarly in the next seven cycles, while the max V_{OC} deceased to 70.31 mV at the 13th exhalation and then rapidly dropped to zero within 5

s. As shown in Figure 4-11c, under an exhalation interval of 3 s, the steady-state V_{OC} was maintained for approximately four cycles: from the third to the seventh. Under a considerably reduced exhalation interval, it only appeared in one or two cycles (Figure 4-11d). In summary, the steady-state V_{OC} under a fast exhalation frequency was retained for less time, and the electricity generated by the BMIEG decreased, as shown in Figure 4-11f. This was caused by the limitation of the moisture absorption capacity of the GO. The water molecules in the RGRC-GCCF accumulated during each circle until moisture saturation; afterward, it was disabled to ionize new H^+ ions, and it quickly discharged.
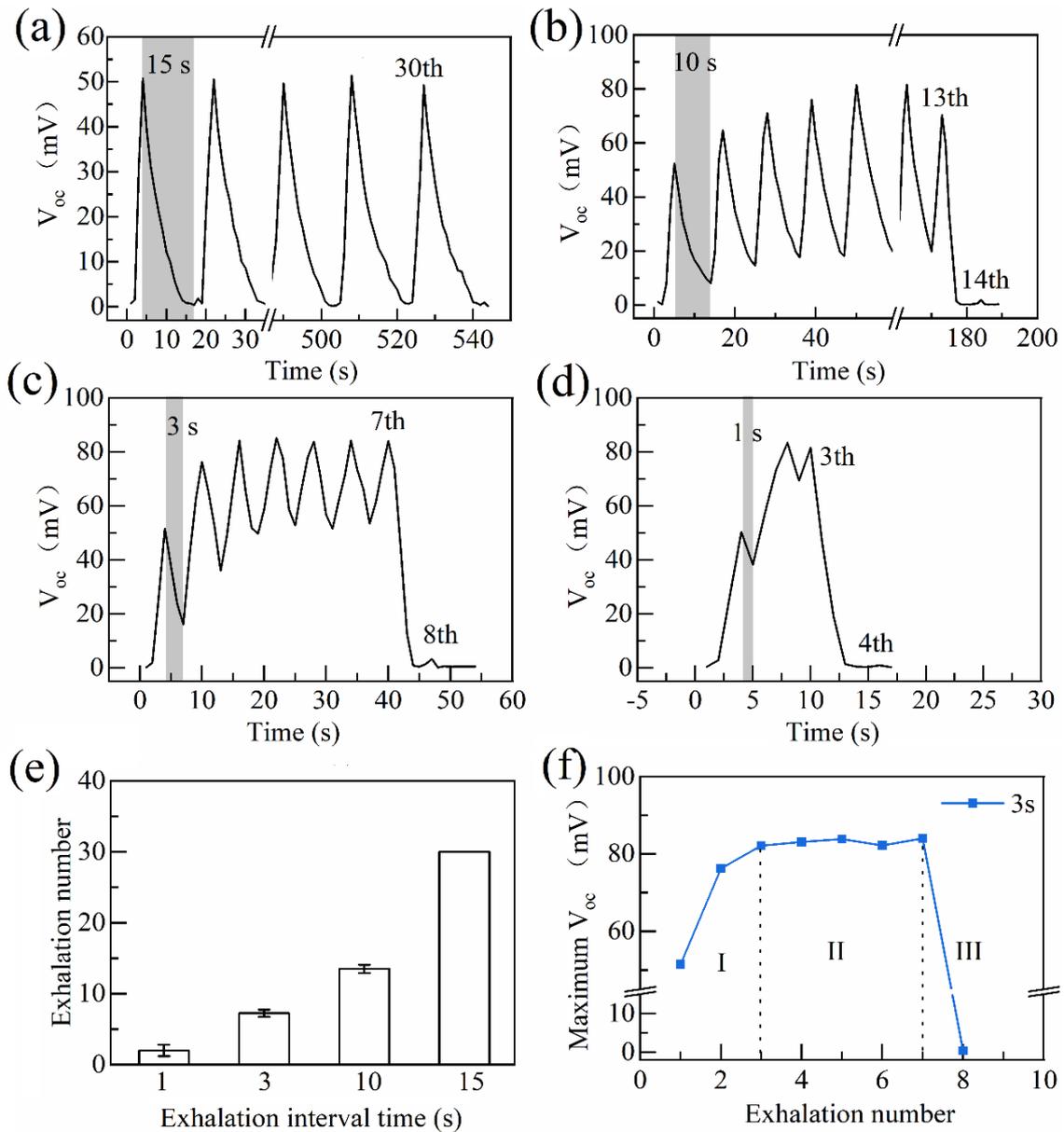
Figure 4- 11 (a–d) the V_{OC} versus time curves of the BMIEG under interval exhalations; the intervals were (a) 15 s, (b) 10 s, (c) 3 s, and (d) 1 s, and each exhalation was maintained for 3 s. The V_{OC} test method of the BMIEG under exhalation was the same as shown in Figure 4-3a. (e) The exhalation number of the steady-state V_{OC} under different interval time. (f) The maximum V_{OC} change curve under each exhalation number, the interval was 3 s.

As it shown in Figure 4-11f, the V_{OC} curves presented three stages

overall: in the beginning, the V_{OC} increased with the accumulation of exhalations (Stage I), and afterward, little change was observed in Stage II; finally, it decreased with the increase of exhalation cycle (Stage III). The initial state of BMIEG is shown in Figure 4-12a. The BMIEG initially had little water and free H^+ ion molecules inside. The directional motion of ions happened in the first exhalation (Figure 4-11b), there by the voltage (Figure 4-11f) increased. After stopping exhalation, water molecular escaped from RGRC-GCCFs (Figure 4-12b) and free H^+ ions recombined with the functional groups on GO. The decrease of free H^+ ions caused the potential difference to drop (Figure 4-12c). However, the short exhalation interval could not allow to completely discharge so that a few water molecules and potential difference remained in the BMIEG (Figure 4-12c). It should be reminded that spontaneous dehumidification always existed because of the humidity difference between the material and environment.

In the exhalations of Stage I, hygroscopicity predominated. So, the peak value of V_{OC} in each cycle increased due to the accumulation potential difference in previous cycle. Due to the accumulation of moisture in each cycle and the limitation of the hygroscopicability of RGRC-GCCF, the moisture concentration difference gradually decreased. Thus, the growth rate of the V_{OC} peak values became small with the increase of exhalation cycle in Stage I (Figure 4-11f). A dynamic balance of moisture absorption and dehumidification could be reached in the exhalations of Stage II that

the peak values changed little (Figure 4-11f), in which the increase and decrease of H^+ ions in hygroscopic process might be equal in a cycle (Figures 4-12d~f). However, the balance could not last long resulted from the uncontrollability of the moisture from each exhalation (content, flow rate, etc.) and other factors. When the balance was broken, it came to the Stage III, in which the peak value of V_{OC} in this stage decreased (Figure 4-11d). The accumulation of water molecular in previous cycles led to the reduce of humidity differences in RGRC-GCCF (Figures 4-12g~h), and dehumidification dominated. Then a fast discharge was conducted since the humidity difference was too small to drive H^+ ions (Figure 4-12i).
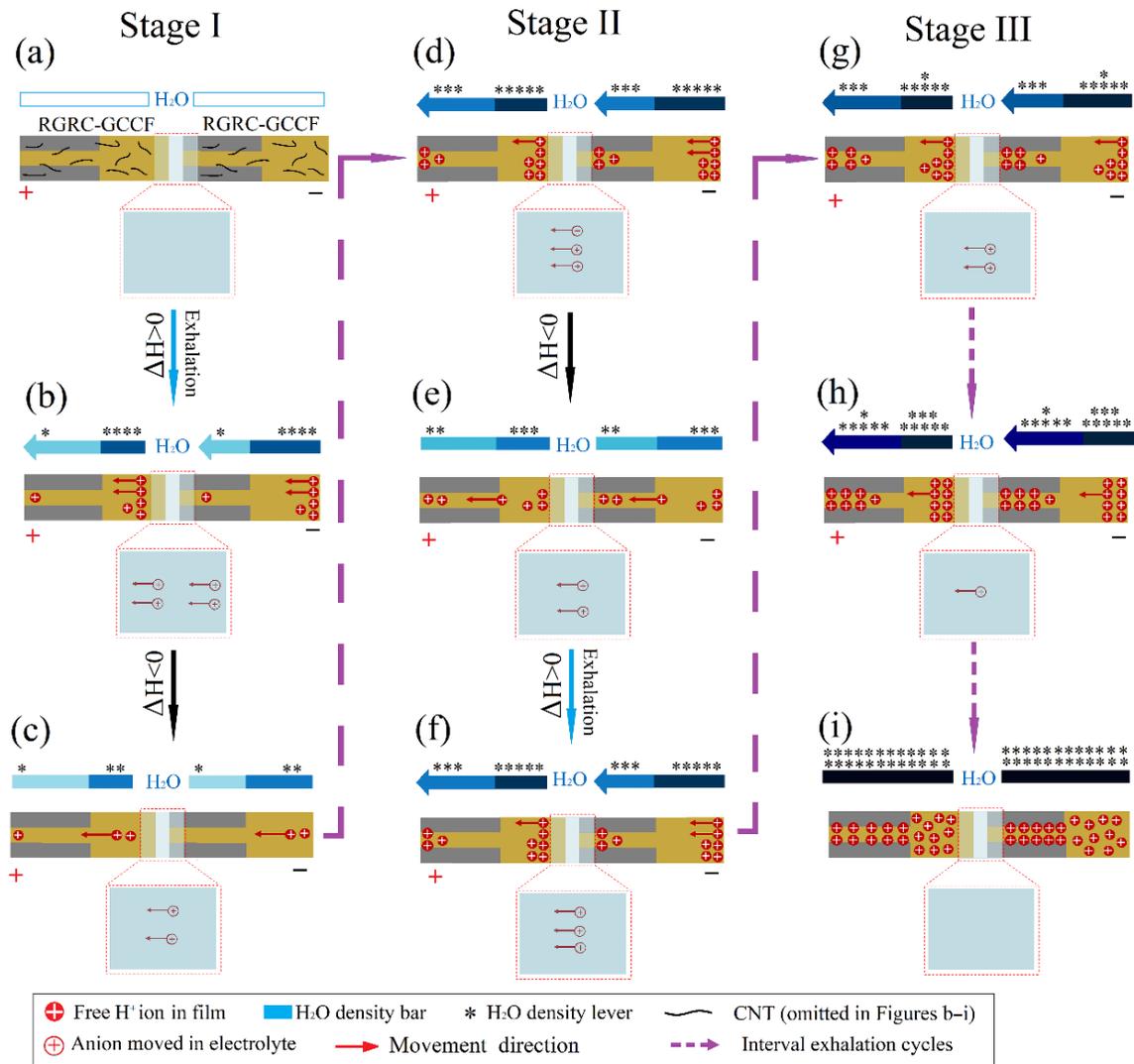
Figure 4-12 The Schematic diagram of the motion water molecules and free H$^+$ ions in BMIEG under exhalations at intervals. State I: (a) the initial state (b)under exhalation (c) stopping exhalation; State II after multiple interval breaths: (d) under exhalation (E) stopping exhalation (f) under exhalation; State III after multiple interval breaths: (g) exhalation (h) stopping exhalation (i) reaching to the saturation. ΔH>0 means humidification and ΔH<0 means dehumidification.

As shown in Figure 4-13a, BMIEG conducted slow discharging behavior under exhalations of 1~5 s, in which the peak value of I$_{SC}$ density

under an exhalation of 5 s did not so increase compared with it under 3 s. It might be difficult for the tester to exhale continuously and steadily for 5 seconds. Additionally, the limitation of the hygroscopicity could not allow the film to absorb so much moisture in short time. The slow discharging behavior relied on the sandwich structure in RGRC-GCCF, which has been verified in our previous work[32]. As shown in Figure 4-13b, after stopping exhalation, the release of water molecular in the RGRC was slower than that in GC parts. It might be due to that the layers on the surface of RGRC had poor hydrophilic. Free H^+ ions reduced in the dehumidification process, and so did the concentration difference. Thus, the current went down slowly with the dehumidification time.

From Figure 4-13c~f, the I_{SC} peak values under the first exhalation were the similar, about 12.43 uA/mm, and the shorter the interval time, the faster the peak value of I_{SC} decreased. The decrease in current might be related to the diffusion of water molecular and the movement of H^+ ions, which both mainly depended on their concentration differences. The moisture in Stage I could be accumulated from previous cycle that in RGRC-GCCF increased because of the incomplete dehumidification. However, the moisture content difference reduced between RGRC part and GC part since it is more difficult for water molecular escape from the RGRC layers with poor hydrophilicity on the surface. Therefore, the number of directional movements of water molecular or the speed of movement decreased or both.

While a fast movement of moisture can drive H^+ ions to move faster. So, the declined synergistical effect from the movement of water molecule，might lead to the decline of I_{SC} peak value. More importantly, the accumulation of H^+ ions in the RCRC part resulted in that the H^+ ions in GC part had to overcome a larger repulsion force to move toward RGRC part with high potential. Then, when the moisture absorption and desorption reach a dynamic equilibrium, the H^+ ions might do reciprocating directional motion in an exhalation cycle. Hence, the peak value varied little in Stage II. When the balance was broken, the current peak value dropped in Stage III.
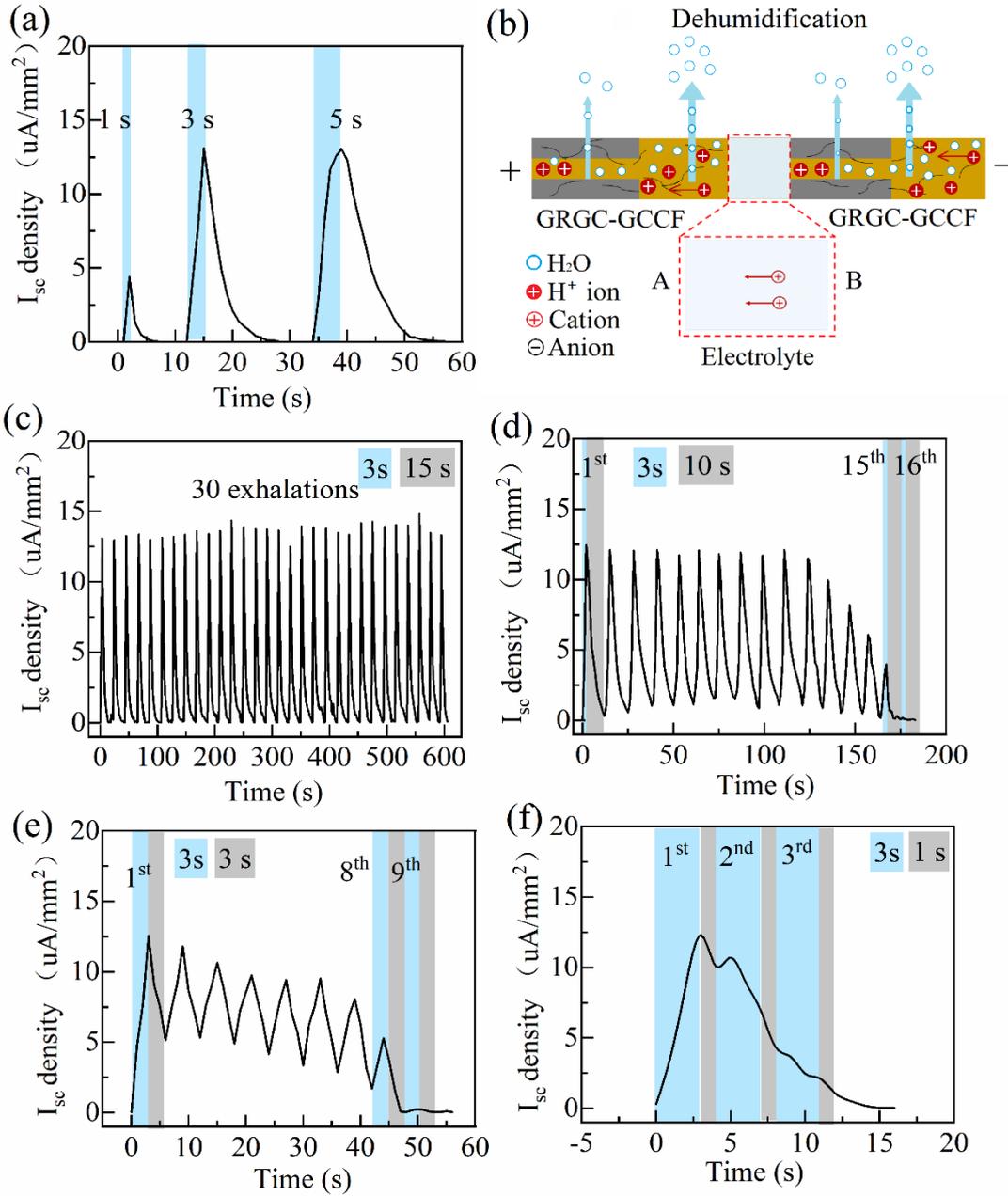
Figure 4-13 (a) The I_{SC} density change curves under different exhalation times; (b–e) the I_{SC} density versus time curves of the BMIEG under interval exhalations; the intervals were (b) 15 s, (c) 10 s, (d) 3 s, and (e) 1 s, and each exhalation was maintained for 3 s. The I_{SC} test method of the BMIEG under exhalation was the same as shown in Figure 4-3a.

4.3.4 The output performance of BMIEGs

To explore the stability of the BMIEG, the generator was placed in different humidity (H = 30%, 50%, and 80%, T = 25°C) and various temperatures (H = 50%, T = 5°C, 20°C, and 35°C) conditions for 30 min to measure the max V_{OC} under an exhalation. As shown in Figure 4-14a, the humidity in the environment had significant influence on its output performance. The decrease of the V_{OC} at a humidity of 80% was due to the weak humidity difference in the RGRC-GCCF in a highly humid environment. The temperature change afforded little difference in the V_{OC} (Figure 4-14a). Considering the suitable size for a wristband or mask, the generator connected using three pieces of the RGRC-GCCFs was employed as a unit (BMIEGs-9, 1 × 9 cm). And generators 3BMIEGs-9 (3 × 9 cm) and 5BMIEGs-9 (5 × 9 cm) were produced to study the influence of the size expandation. As shown in Figure 4-14b, the V_{OC} increased because of the expansion of the hygroscopic area which could endow the generator to release much more free ions. The exhalation cycles to reach the maximum voltage for each sample increased as Table 1 showed, as the generator with larger size can absorbed more moisture.

Table 1 The exhalation cycles to reach stable V_{OC}

Sample	BMIEGs-6	BMIEGs-9	2BMIEGs-9	3BMIEGs-9	5BMIEGs-9
Size (cm^2)	6	9	18	27	75
Exhalation cycles	3.5±0.58	5.7±0.96	9±0.82	11.75±0.95	22.5±1.29

The V_{OC} and I_{SC} change curves of the 5BMIEGs-9 under interval exhalations also presented three stages, as shown in Figures 4-14c and 4-14d. In Stage I, the V_{OC} value exhibited a changed peak-like increase, and the peak voltage value increased with the exhalation cycle in the initial 90 s (approximately 15 exhalations). Thereafter, the V_{OC} attained a stable change with an amplitude value of 0.83–1.44 V in approximately 32 exhalation cycle (about 194 s, Stage II). In stage III, both the V_{OC} and I_{SC} peak values decreased. The change of the I_{SC} density in Stage II were different that I_{SC} density sharply increased to 13.43 µA/mm2 and then conducted a changed peak-like decrease (Figure 4-14d). This is similar to the result of Figure 4-13c, the current peak value of the 5BMIEGS-9 decreased more slowly due to the size expansion. The change range of the I_{SC} density was 5.42–10.17 µA/mm^2 in Stage II. The Stage II could last about approximately 200 s, which endowed the possibility for the 5BMIEGs-9 to supply a sustainable electricity. To verify this conjecture, 5BMIEGs-9 and LED were connected in series (Figure 4-14e, OFF state). A commercial LED was lit up and out for approximately 24 exhalations

(144 s) at State II (the minimum V_{OC} and I_{SC} were 0.83 V and 32.52 μA, respectively). This changeable electricity can be applied in signal emission and instantaneous or intermittent power supply. Connecting a capacitor was beneficial to maintain V_{OC} stable. When a capacitor was connected in series (Figure 4-14e, ON state), the LED remained lit for more than 39 exhalations (approximately 234 s), showing the potential application for a short-time power supply. Furthermore, it obtained good flexibility and stability (Figure 4-15) and could be worn on the wrist (Figure 4-14g).
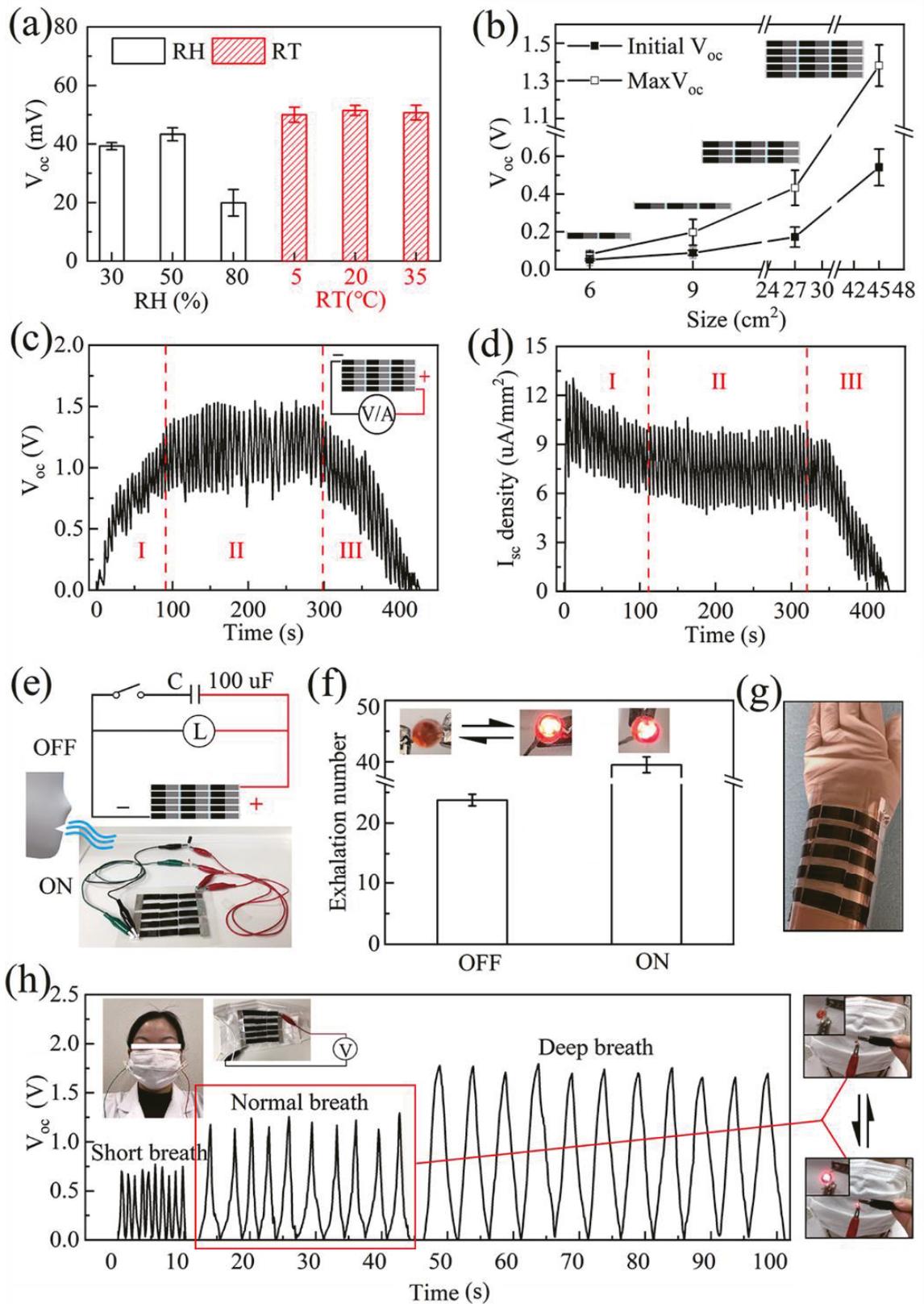
Figure 4-14 (a) The stable V_{OC} of the BMIEG under different humidity and temperature values;

(b) the effect of the expansion of the BMIEG on the initial V_{OC} and stable V_{OC}; (c, d) the V_{OC} and I_{SC} density change curves under the action of the exhalation of the expanded BMIEGs with a size of 45 cm^2 (5BMIEGs-9) and the voltage change curve under the action of exhalation; (e) the connection circuit diagram and photo of the 5BMIEGs-9, an LED (a red bulb can be lighted when the power supply >1.2 V, 30 uA), and a capacitor (100 μF). The ON and OFF switch shows if the capacitor is connected or not. (f) The exhalation number shows that the LED lit up in states ON and OFF in a dim room. The pictures of the different lit states of the LED under OFF and ON are included; (g) the digital photo of the 5BMIEGs-9 worn on the wrist. (h) The V_{OC} change curve of the 5BMIEG-9 under different breath frequencies of 30 min^{-1} (short breath), 10 min^{-1} (normal breath), and 6 min^{-1} (deep breath); the digital photos of the LED powered by the 5BMIEGs-9 under normal breath in a dim room.

Considering that the 5BMIEG-9 produced a significant voltage signal under exhalations from oral, the generator was placed in a mask to record the Voc change under different breath frequencies, aiming to explore its possibility in breath monitoring. As Figure 4-14h shown, three breathing frequencies of 30 min^{-1} (short breath), 10 min^{-1} (normal breath), and 6 min^{-1} (deep breath) were conducted, in which the exhalation and inhalation time is same. Under three breathing frequencies, the generator did show a slow discharging performance that the Voc increased with exhalation and droped to 0 in inhalation. This might be due to that inhalation behavior enhanced dehumidification effect. Besides, the direction of wet airflow

approach to the generator was changed in the mask, and much moisture was absorbed by mask. The peak V_{OC} under the three breath frequencies (short, normal, and deep) were approximately 0.72, 1.12, and 1.69 mV, respectively. The significant difference of the V_{OC} suggested an application potential in breath monitoring. The V_{OC} under a deep breath was the highest because of the increased moisture supply. Additionally, that the Voc change under normal breath could remain for more than 2 h (Figure 4-16), suggested a good stability. As the photo in Figure 4-14h shown, a LED could be lit up with exhalation and went out with inhalation by the generator. So, it can also be used as a signal generator for breath monitoring. To sum up, the BMIEG has an application potential of breath monitoring and a signal generator for it.
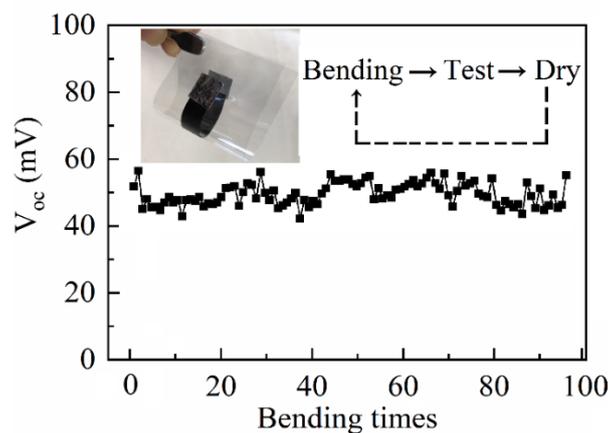

Figure 4-15 The max V_{OC} of BMIEG under an exhalation for bending 100 times
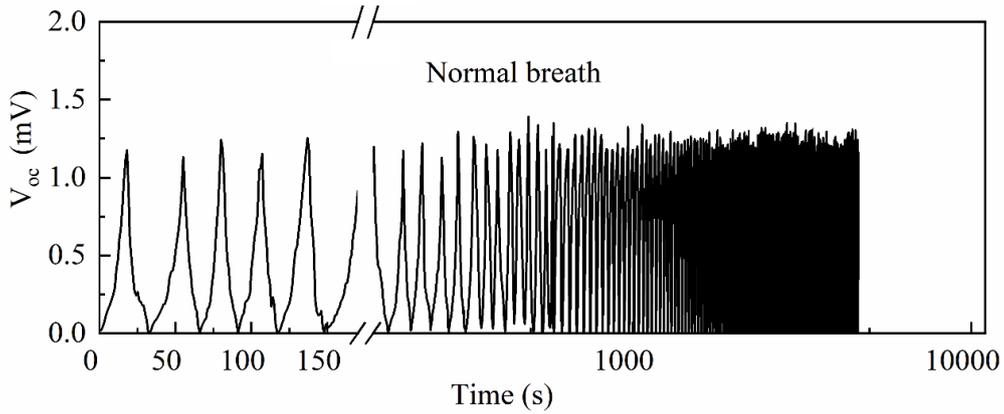
Figure 4-16 The V_{OC} curve of 5BMIEG-9 under normal breath for 2 h
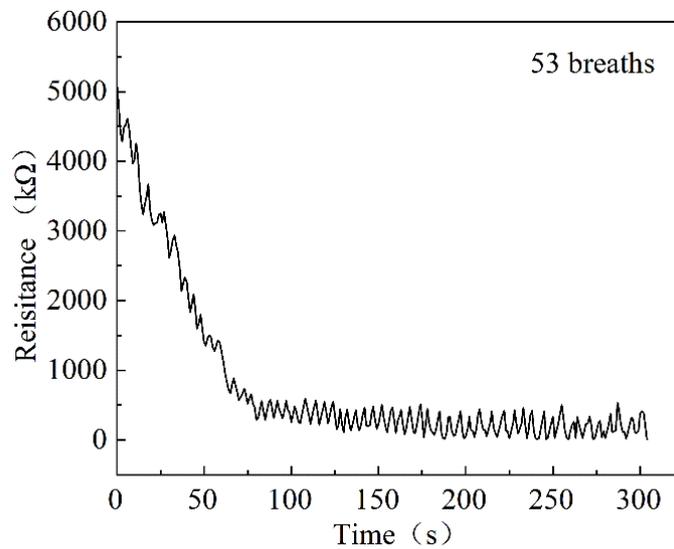
Figure 4-17 The resistance curve of 5BMIEG-9 under 53 normal breaths

The V_{OC} and I_{SC} of 5BMIEG-9 showed peak-like changes under intermittent exhalations. In order to facilitate the calculation, we simplified the three stages of the V_{OC} and I_{SC} density curves into linear change curves, as shown in Figure 4-18. Hence, the average V_{OC} of 0.57 V (Figure 4-18a) and I_{SC} density mean of 10.97 uA/mm^2 (Figure 4-18b) in Stage I were considered to calculate the power density. According to the formula $P =$

$\frac{V_{OC}I_{SC}}{4}$, 5BMIEG-9 could gain power density of 1.55 uW/mm^2. In Stage II, based on the average V_{OC} of 1.97 V (Figure 4-18a) and the mean value of I_{SC} density of 7.80 u/mm^2 (Figure 4-18b), the power density was 1.94 uA/mm^2. The power density of the stage III was 0.97 uW/mm^2.
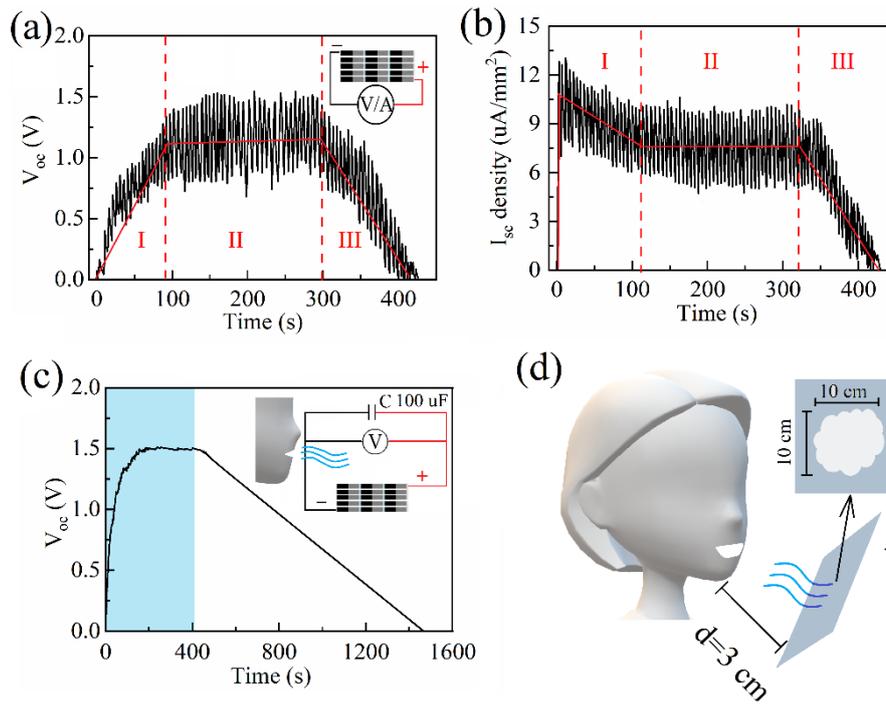
Figure 4-18 The V_{OC} (a) and I_{SC} density (b) curves of 5BMIEG-9 under interval exhalations. (c) The V_{OC} versus time curves of BMIEG connected with a capacitor under interval exhalations. (d) The moisture area formed by the exhaled water vapor on the glass plate 3 cm away.

In Figure 4-18b, I_{SC} of 5BMIEG-9 is larger than 33uA (with an area of 6mm^2) during Stage I and II, and the LED with a red bulb can be lighted up under power supply >30 uA, 1.2 V, so the I_{SC} is sufficient. As shown in

127

Figure 4-10a, without a capacitor connected, when t >90s, the maximum V_{OC} can reach 1.2V, and the maximum V_{OC} >1.2 V time is about 200 s (Figure 4-14f-OFF). While the minimum voltage in Stage II cannot meet the need. So, the LED cannot be continuously lighted up (Figure 4-14f-OFF). A capacitor (100 uF) connected in parallel is used. The V_{OC} change curve of 5BMIEG-9 connected with the capacitor is shown in Figure 18c. The V_{OC} grows up quickly and reaches to 1.2 V at 61 s, and the duration of V_{OC} >1.2 V is about 570 s, which is much greater than the duration time (about 300 s) of I_{SC} > 30 uA. Thus, it can satisfy to continuously light up the LED for 240 s (about 39 breaths, Figure 4-14f-ON). As shown in Figure 4-18d, each time the moisture exhaled from the oral cavity forms an area of about 10 cm × 10 cm on the glass plate, which is limited by the material area limitation of the material preparation method, the current 5BMIEG-9 area assembly area is about 9 cm × 9 cm, so it makes little sense to gain larger size to obtain higher energy. Therefore, improving the material preparation method and adding water-absorbing particles are considered in our future work to achieve much higher electricity that LED can be lighted up by the first exhalation and prolong the lighting time.

BMIEG also can not only generate electricity based on breathing moisture, but also harvest energy from moist air or from direct contacted water droplets. As shown in Figure 4-19a, the V_{OC} almost changes after reaching 121 mV within 10 minutes in an environment with a humidity of

75%. Afterwards the V_{OC} changed little for about 25 minutes and then dropped to 0 in the last 17 minutes. It might be due to the moisture absorption saturation in BMIEG that there was no water molecular concentration difference in RGRC-GCCF to drive directional motion or there was no new H^+ ions released by GO combined with water molecular. The corresponding I_{SC} rapidly increased to 14.3 uA within ten seconds, and then slowly decreased to 0 (Figure 4-19b). According to the formula, $P = \frac{V_{OC}I_{SC}}{4}$, the power was calculated that a BMIEG could gain power of 0.11 uW. Its slow discharge behavior endowed BMIEG the ability to substantially generate electricity in a humid environment, which was consistent with the power generation behavior of BMIEG under breathing moisture in the article. As shown in Figure 4-19c, when 3 uL of distilled water is directly added to the unreduced part of the two electrode films in the BMIEG, the V_{OC} quickly reaches about 345 mV within a few seconds, and then the V_{OC} decreases to 0 in 5 minutes due to the dehumidification. The corresponding I_{SC} presented a similar change, and the maximum value was about 35 uA. The V_{OC} and I_{SC} in Figure 4-19c and 4-19d were much larger, since the liquid water only entered the GCC part and formed a significant humidity difference to drive a surge and rapid movement of H^+ ions. While the V_{OC} could not be sustained as Figure 4-19a.The max power was 3 uW, because of the limited amount of water molecules in water drops and the continuous dehumidification behavior.
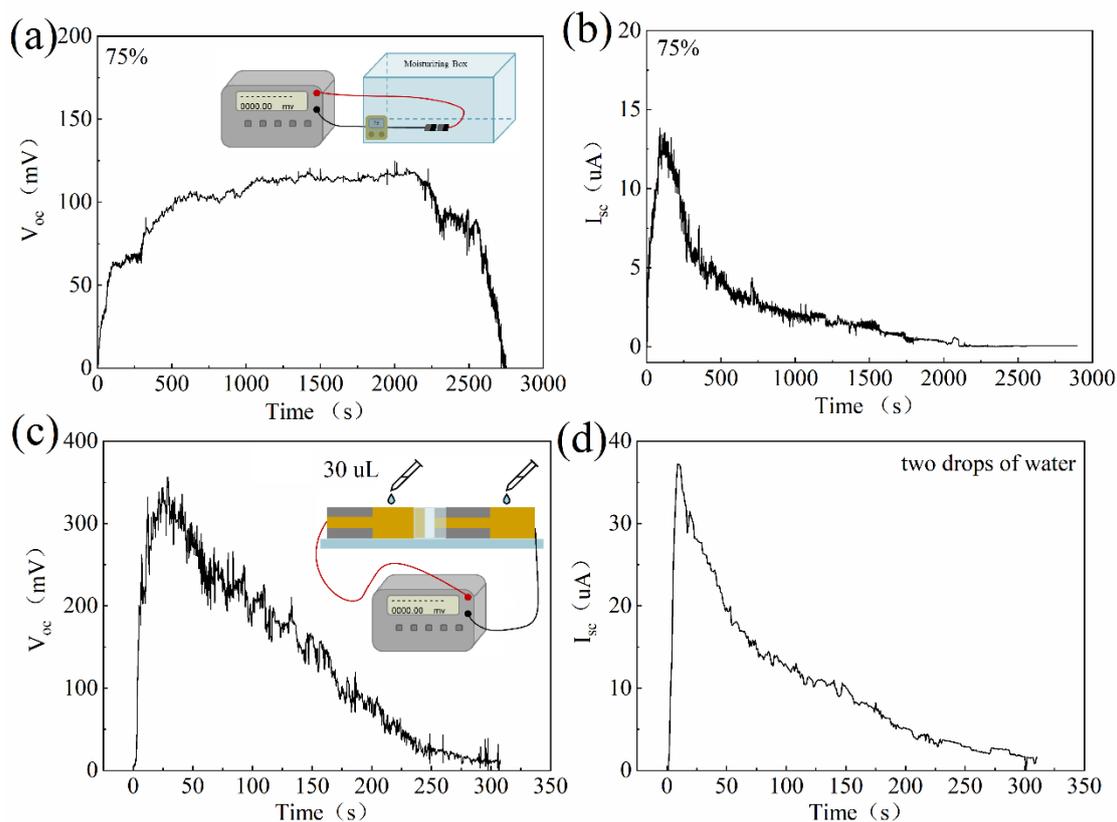
Figure 19 The V_{OC} (a) and I_{SC} (b) change curves of BMIEG under an environment with a humidity of 75%, the V_{OC} (c) and I_{SC} (d) change curves of BMIEG added two drops of distilled water on the GCC part and a drop was 30 uL.

4.4 Conclusions

In this chapter, a sustainable, continuously expandable, and wearable breath moisture-induced electricity generator was successfully innovated. The BMIEG mainly relied on the hydrophilicity difference caused by a regional UV treatment on the RGRC-GCCF, which achieved concentration differences and directional movement of water molecules and H^+ ions. The appropriate addition of CNT could enhance the induced electricity. The

130

BMIEG was arbitrarily assembled by the end-to-end connection of two RGRC-GCCFs and enlarged to meet various requirements of power supply. The 5BMIEGs-9 discontinuously lit an LED under intermittent breaths with a peak V_{OC} of 1.44 V. Further, a capacitor was employed to sustain the generator to light the LED up for approximately 4 min. The BMIEG presented excellent adaptability for the requirements of instantaneous, variable, and stable voltage power generation, and it controllably generated diverse electrical signals based on exhalation ways and electronic component assembly. Additionally, the generator obtained application prospects in respiration sensors because the V_{OC} signal changed stably in obvious differences under different respiratory frequencies. Because of the excellent flexibility and reusability of the BMIEG, it can be employed as a power supply for wearable electronics and mask built-in breathing monitors. Further research will be conducted to improve the production method of the RGRC-GCCF to enlarge the size and try different assembly methods to gain a relatively high output performance.

References

[1] M.V. Boskovic, M. Sarajlic, M. Frantlovic, M.M. Smiljanic, D.V. Randjelovic, K.C. Zobenica, D.V. Radovic, Aluminum-based self-powered hyper-fast miniaturized sensor for breath humidity detection, Sens. Actuator B-Chem. 321 (2020) 10.

[2] J. Liu, Design and simulation analysis of offshore tidal energy generating set system based on sensor network, Arabian Journal of Geosciences 14(11) (2021).

[3] M.N. Ayob, V. Castellucci, J. Abrahamsson, R. Waters, A Remotely Controlled Sea Level Compensation System for Wave Energy Converters, Energies 12(10) (2019).

[4] L.L. Wang, Y.X. Song, W.H. Xu, W.B. Li, Y.K. Jin, S.W. Gao, S.Y. Yang, C.Y. Wu, S. Wang, Z.K. Wang, Harvesting energy from high-frequency impinging water droplets by a droplet-based electricity generator, Ecomat 3(4) (2021).

[5] Y.L. Wang, J.L. Duan, Y.Y. Zhao, B.L. He, Q.W. Tang, Harvest rain energy by polyaniline-graphene composite films, Renewable Energy 125 (2018) 995-1002.

[6] C.C. Liu, J. Ju, Y.M. Zheng, L. Jiang, Asymmetric Ratchet Effect for Directional Transport of Fog Drops on Static and Dynamic Butterfly Wings, ACS Nano 8(2) (2014) 1321-1329.

[7] Jun Yin, Xuemei Li, Jin Yu, Zhuhua Zhang, Jianxin Zhou, W. Guo,

Generating electricity by moving a droplet of ionic liquid along graphene, Nature Nanotechnology 56 (2014, 04) 1-6.

[8] X. Wang, S.M. Fang, J. Tan, T. Hu, W.C. Chu, J. Yin, J.X. Zhou, W.L. Guo, Dynamics for droplet-based electricity generators, Nano Energy 80 (2021).

[9] Y. Li, W.P. Hong, H.R. Li, Z. Yan, S.M. Wang, X.Y. Liu, B.Y. Li, H.F. Jiang, X.J. Niu, Solar absorber with tunable porosity to control the water supply velocity to accelerate water evaporation, Desalination 511 (2021).

[10] V.D. Dao, N.H. Vu, H.L.T. Dang, S.N. Yun, Recent advances and challenges for water evaporation-induced electricity toward applications, Nano Energy 85 (2021).

[11] Z.Y. Wang, Y.L. Wu, K.Q. Xu, L.P. Jiang, J.K. Sun, G.Y. Cai, G.F. Li, B.Y. Xia, H.F. Liu, Hierarchical Oriented Metal-Organic Frameworks Assemblies for Water-Evaporation Induced Electricity Generation, Advanced Functional Materials (2021).

[12] Z.L. Luo, C.H. Liu, S.S. Fan, A moisture induced self-charging device for energy harvesting and storage, Nano Energy 60 (2019) 371-376.

[13] C. Yang, Y.X. Huang, H.H. Cheng, L. Jiang, L.T. Qu, Rollable, Stretchable, and Reconfigurable Graphene Hygroelectric Generators, Advanced Materials 31(2) (2019).

[14] Z.H. Zhang, X.M. Li, J. Yin, Y. Xu, W.W. Fei, M.M. Xue, Q. Wang, J.X. Zhou, W.L. Guo, Emerging hydrovoltaic technology, Nature

Nanotechnology 13(12) (2018) 1109-1119.

[15] T. Xu, Q. Han, Z.H. Cheng, J. Zhang, L.T. Qu, Interactions between Graphene-Based Materials and Water Molecules toward Actuator and Electricity-Generator Applications, Small Methods 2(10) (2018).

[16] T. Xu, X.T. Ding, Y.X. Huang, C.X. Shao, L. Song, X. Gao, Z.P. Zhang, L.T. Qu, An efficient polymer moist-electric generator, Energy & Environmental Science 12(3) (2019) 972-978.

[17] F. Zhao, H.H. Cheng, Z.P. Zhang, L. Jiang, L.T. Qu, Direct Power Generation from a Graphene Oxide Film under Moisture, Advanced Materials 27(29) (2015) 4351-4357.

[18] M.J. Li, L. Zong, W.Q. Yang, X.K. Li, J. You, X.C. Wu, Z.H. Li, C.X. Li, Biological Nanofibrous Generator for Electricity Harvest from Moist Air Flow, Advanced Functional Materials 29(32) (2019).

[19] W.Q. Yang, X.K. Li, X. Han, W.H. Zhang, Z.B. Wang, X.M. Ma, M.J. Li, C.X. Li, Asymmetric ionic aerogel of biologic nanofibrils for harvesting electricity from moisture, Nano Energy 71 (2020).

[20] Z.Y. Sun, L.L. Feng, C.D. Xiong, X.Y. He, L.M. Wang, X.H. Qin, J.Y. Yu, Electrospun nanofiber fabric: an efficient, breathable and wearable moist-electric generator, Journal of Materials Chemistry A 9(11) (2021) 7085-7093.

[21] D. Shen, W.W. Duley, P. Peng, M. Xiao, J.Y. Feng, L. Liu, G.S. Zou, Y.N. Zhou, Moisture-Enabled Electricity Generation: From Physics and

Materials to Self-Powered Applications, Advanced Materials 32(52) (2020).

[22] L.H. Li, Z.G. Chen, M.M. Hao, S.Q. Wang, F.Q. Sun, Z.G. Zhao, T. Zhang, Moisture-Driven Power Generation for Multifunctional Flexible Sensing Systems, Nano Letters 19(8) (2019) 5544-5552.

[23] X. Gao, T. Xu, C.X. Shao, Y.Y. Han, B. Lu, Z.P. Zhang, L.T. Qu, Electric power generation using paper materials, Journal of Materials Chemistry A 7(36) (2019) 20574-20578.

[24] Y.X. Huang, H.H. Cheng, C. Yang, H.Z. Yao, C. Li, L.T. Qu, All-region-applicable, continuous power supply of graphene oxide composite, Energy & Environmental Science 12(6) (2019) 1848-1856.

[25] Y.X. Huang, C.Z. Wang, C.X. Shao, B.Y. Wang, N. Chen, H.B. Jin, H.H. Cheng, L.T. Qu, Graphene Oxide Assemblies for Sustainable Clean-Water Harvesting and Green-Electricity Generation, Accounts of Materials Research 2(2) (2021) 97-107.

[26] C.X. Shao, J. Gao, T. Xu, B.X. Ji, Y.K. Xiao, C. Gao, Y. Zhao, L.T. Qu, Wearable fiberform hygroelectric generator, Nano Energy 53 (2018) 698-705.

[27] H.Z. Yao, P.P. Zhang, Y.X. Huang, H.H. Cheng, C. Li, L.T. Qu, Highly Efficient Clean Water Production from Contaminated Air with a Wide Humidity Range, Advanced Materials 32(6) (2020).

[28] M.H. Ye, Z.P. Zhang, Y. Zhao, L.T. Qu, Graphene Platforms for Smart

Energy Generation and Storage, Joule 2(2) (2018) 245-268.

[29] T. Xu, X.T. Ding, C.X. Shao, L. Song, T.Y. Lin, X. Gao, J.L. Xue, Z.P. Zhang, L.T. Qu, Electric Power Generation through the Direct Interaction of Pristine Graphene-Oxide with Water Molecules, Small 14(14) (2018).

[30] F. Zhao, Y. Liang, H.H. Cheng, L. Jiang, L.T. Qu, Highly efficient moisture-enabled electricity generation from graphene oxide frameworks, Energy & Environmental Science 9(3) (2016) 912-916.

[31] Y. Liang, F. Zhao, Z.H. Cheng, Q.H. Zhou, H.B. Shao, L. Jiang, L.T. Qu, Self-powered wearable graphene fiber for information expression, Nano Energy 32 (2017) 329-335.

[32] S. Chen, H. Xia, Q.Q. Ni, A Wearable Sustainable Moisture-Induced Electricity Generator Based on rGO/GO/rGO Sandwich-Like Structural Film, Advanced Electronic Materials 7(7) (2021).

[33] M. Ma, F. Grey, L.M. Shen, M. Urbakh, S. Wu, J.Z. Liu, Y.L. Liu, Q.S. Zheng, Water transport inside carbon nanotubes mediated by phonon-induced oscillating friction, Nature Nanotechnology 10(8) (2015) 692-695.

[34] B.N.J. Persson, U. Tartaglino, E. Tosatti, H. Ueba, Electronic friction and liquid-flow-induced voltage in nanotubes, Physical Review B 69(23) (2004).

[35] D.C. Marcano, D.V. Kosynkin, J.M. Berlin, A. Sinitskii, Z.Z. Sun, A. Slesarev, L.B. Alemany, W. Lu, J.M. Tour, Improved Synthesis of Graphene Oxide, Acs Nano 4(8) (2010) 4806-4814.

[36] S. Ghosh, A.K. Sood, N. Kumar, Carbon nanotube flow sensors, Science 299(5609) (2003) 1042-1044.

[37] J.X. Pei, J. Huang, Z. Huang, K. Liu, Liquid flow-induced electricity in carbon nanomaterials, Sustainable Energy & Fuels 3(3) (2019) 599-610.

[38] D.D. Han, Y.L. Zhang, Y. Liu, Y.Q. Liu, H.B. Jiang, B. Han, X.Y. Fu, H. Ding, H.L. Xu, H.B. Sun, Bioinspired Graphene Actuators Prepared by Unilateral UV Irradiation of Graphene Oxide Papers, Advanced Functional Materials 25(28) (2015) 4548-4557.

[39] Y.G. Bi, J. Feng, Y.F. Li, Y.L. Zhang, Y.S. Liu, L. Chen, Y.F. Liu, L. Guo, S. Wei, H.B. Sun, Arbitrary Shape Designable Microscale Organic Light-Emitting Devices by Using Femtosecond Laser Reduced Graphene Oxide as a Patterned Electrode, Acs Photonics 1(8) (2014) 690-695.

[40] A.A. Amer, S.M. Reda, M.A. Mousa, M.M. Mohamed, Mn3O4/graphene nanocomposites: outstanding performances as highly efficient photocatalysts and microwave absorbers, Rsc Advances 7(2) (2017) 826-839.

[41] N. Diez, A. Sliwak, S. Gryglewicz, B. Grzyb, G. Gryglewicz, Enhanced reduction of graphene oxide by high-pressure hydrothermal treatment, Rsc Advances 5(100) (2015) 81831-81837.

[42] X.H. Tai, S.W. Chook, C.W. Lai, K.M. Lee, T.C.K. Yang, S. Chong, J.C. Juan, Effective photoreduction of graphene oxide for photodegradation of volatile organic compounds, Rsc Advances 9(31)

(2019) 18076-18086.

[43] Z.J. Liu, Z.H. Qian, J.N. Song, Y. Zhang, Conducting and stretchable composites using sandwiched graphene-carbon nanotube hybrids and styrene-butadiene rubber, Carbon 149 (2019) 181-189.

[44] S.Q. Chen, W.K. Yeoh, Q. Liu, G.X. Wang, Chemical-free synthesis of graphene-carbon nanotube hybrid materials for reversible lithium storage in lithium-ion batteries, Carbon 50(12) (2012) 4557-4565.

[45] A. Lasalle, C. Guizard, E. Maire, J. Adrien, S. Deville, Particle redistribution and structural defect development during ice templating, Acta Materialia 60(11) (2012) 4594-4603.

[46] X. Sui, H.R. Ding, Z.W. Yuan, C.F. Leong, K.L. Goh, W. Li, N. Yang, D.M. D'Alessandro, Y. Chen, The roles of metal-organic frameworks in modulating water permeability of graphene oxide-based carbon membranes, Carbon 148 (2019) 277-289.

[47] S. Kim, S. Zhou, Y.K. Hu, M. Acik, Y.J. Chabal, C. Berger, W. de Heer, A. Bongiorno, E. Riedo, Room-temperature metastability of multilayer graphene oxide films, Nature Materials 11(6) (2012) 544-549.

[48] W. Gao, N. Singh, L. Song, Z. Liu, A.L.M. Reddy, L.J. Ci, R. Vajtai, Q. Zhang, B.Q. Wei, P.M. Ajayan, Direct laser writing of micro-supercapacitors on hydrated graphite oxide films, Nature Nanotechnology 6(8) (2011) 496-500.

Chapter 5：General conclusions

In this study, a variety of regional asymmetric oxygen-containing GO base films were obtained based on UV reduction of GOF, and the asymmetric hydrophilicity was used to form a concentration difference of water molecules, thereby forming H+ ions to perform directional movement due to the concentration difference to obtain induced voltage and current. And the applications of their induced electrical signals in moisture power generation, humidity monitoring, respiration monitoring and so on are discussed.

In Chapter 1, the basic properties of GO and some common reduction methods are summarized, and the applications of GO and RGO in humidity power generation and sensors are summarized.

In Chapter 2, RGFs with different oxygen-containing were developed by UV treating on the surface of GOF for 3 h. And the treatment time can control reduce the oxygen-contain, surface hydrophilicity and improve conductivity. Based on the difference in hydrophilicity of two surfaces, RGF can generate an electricity of 86 mV and 2.3 uA under 85%. The RGF-based HEG can generate peak values of 424 mV, 9.1 uA under 85%. And HESs with expandation powered a timer successfully. It suggested that the UV reduced GO-based film with the is very promising in moisture induced electricity, so in the further research we try to replace the use of sunlight

instead of UV irradiation for the reduction of GO.

In Chapter 3, the double-sided reduction treatment of GOF with UV is used to obtain the RGO/GO/RGO sandwich structure, RGRSF and RGRSF–GO composite films were developed by a simple bilateral UV treatment on GO films. Without any additives, power generation from the moisture mechanism of MIEG mainly depends on the hydrophilicity difference between the two films. The special sandwich structure endows MIEG with the capability to generate sustained electricity under moisture for more than 5.5 h and slow discharge in a dry condition. The high stability and reproducibility of MIEG were demonstrated by 100 cycles repetition of charge and discharge experiments. Besides, the generator could be easily scaled up for higher output. 9MIEGs successfully powered a LED under moisture and kept it lit for 1 h in a normal room condition, thereby showing excellent adaptability to humidity changes in the application for wearable electronic products. Besides, the MIEG has many benefits of flexibility, high stability, reusability, lightweight, low price of medicines, and ease of production.

In Chapter 4, based on the RGO/GO/RGO sandwich structure, I add CNTs into the GO base film and optimize the domain design of asymmetric hydrophilicity to develop a BMIEG that can provide sustainable electricity under intermittent exhalations. a sustainable, continuously expandable, and wearable breath moisture-induced electricity generator was successfully

innovated. The BMIEG was arbitrarily assembled by the end-to-end connection of two RGRC-GCCFs and enlarged to meet various requirements of power supply. The 5BMIEGs-9 discontinuously lit an LED under intermittent breaths with a peak V_{OC} of 1.44 V. Further, a capacitor was employed to sustain the generator to light the LED up for approximately 4 min. The BMIEG presented excellent adaptability for the requirements of instantaneous, variable, and stable voltage power generation, and it controllably generated diverse electrical signals based on exhalation ways and electronic component assembly. Additionally, the generator obtained application prospects in respiration sensors because the V_{OC} signal changed stably in obvious differences under different respiratory frequencies.

In conclusion, I utilize UV reduction to obtain various the GO-based films with reginal difference in hydrophilicity. And based on their performance of moisture-induced power generation to develop generators and sensors with different application potentials, and the research progresses layer by layer. Otherwise, it is verified that UV treatment on GOF shows many advantages such as high controllability and flexibility. I look forward that in the further research UV irradiation can be replaced by sunlight as a source to reduce GOF and obtain similar good effect.

In conclusion, UV treatment can be used to obtain various the GO-based films with reginal difference in hydrophilicity which is promising in the

field of moisture-induce electricity generation. Based on the regionally hydrophilic difference of GO-based films, sustainable environmental and breath moisture-induced power generators were developed. Besides, UV treated GO-based films show many advantages such as well controllable, flexible and wearable. In the further research, sunlight can be considered to replace UV irradiation as a source to obtain similar good effect and other different regional treatments can be discussion for more applications.

List of publications

1. <u>Chen Si</u>, Xia Hong, Ni Qing-Qing, A Sustainable, Continuously Expandable, Wearable Breath Moisture-Induced Electricity Generator, Carbon[J], 2022(194):104-113.

2. <u>Chen Si</u>, Xia Hong, Ni Qing-Qing, A Wearable Sustainable Moisture-Induced Electricity Generator Based on rGO/GO/rGO Sandwich-Like Structural Film, Advanced Electronic Materials[J], 2021.06.

Acknowledgement

Firstly, I am very grateful to the China Scholarship Council for providing me with a program to study abroad, and to the Ministry of Education, Culture, Sports, Science and Technology for supporting me funds in my study, so that I can devote myself to the study of my doctoral program and smoothly complete my coursework. Secondly, I would like to thank my two supervisors Prof. NI Qing-Qing and Prof. Natuski for their guidance and help. Pro. NI helped me to carry out graphene-related research, offered a good experimental environment and provided many valuable opinions for my research. In the last half year of the doctoral program, I entered to Prof. Natuski's group. Thanking for their help, I can complete doctor study. In addition, I would like to appreciate Xia Hong the researcher of NI group, for helping me a lot in my study and life, which gave me a lot of help to adapt to life and study in Japan. Meanwhile, I was moved that my master supervisors Prof. Qiu and Prof. Jiang have been caring about my study and life abroad and thanked them for their concern.

In addition, I want to say thanks to my members in our group for their help and accompany. My tutor Guan Xiaoyu, he helped me a lot in dealing with various academic and life trivial matters in the first year. And my senior sister Cui Lina, the happy times with her and her family became my fond memories. I am especially grateful for her 10-year-old daughter，the lively and lovely girl brought so much enjoyment to my boring life.